Evaluating Approximate Methods for Computing Extracellular Potentials from Neuronal Networks

Steinn Hauser Magnússon

Thesis submitted for the degree of
Master in Computational Physics
60 credits

Department of Physics
Faculty of mathematics and natural sciences

UNIVERSITY OF OSLO

Spring 2021

Evaluating Approximate Methods for Computing Extracellular Potentials from Neuronal Networks

Steinn Hauser Magnússon

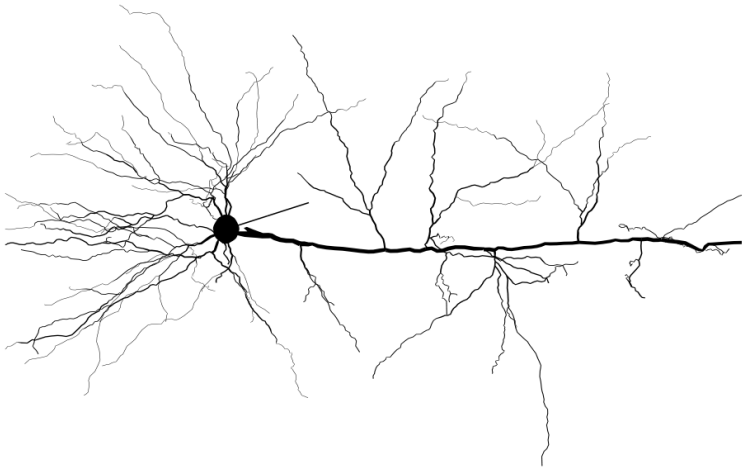

Evaluating Approximate Methods for Computing Extracellular Potentials from Neuronal Networks

http://www.duo.uio.no/

Printed: Repro sentralen

Contents

Acknowledgements

I would like to thank my advisor Gaute Einevoll and my two co-advisors Espen Hagen and Torbjørn Ness for the help throughout the year. In particular thank-you to Espen Hagen for the insightful discussions and answering my emails every time for the past months.

Thanks to my mom and dad for all the support in the past years while I finished my studies. Couldn't ask for better parents. Thanks to my brother for being on the other end of the phone each time I call and providing me with well needed decompression.

Thanks to my girlfriend who put up with two years of long-distance with me to get our masters degrees completed. Can't wait to start the next chapter in Leipzig 2021. Thanks additionally to the Irish in-laws for putting up with me during my extensive visits in the past two years. It made things so much more bearable. Final thanks to the supportive network of friends who are and always have been there for me back home.

Abstract

With the resurgence in popularity of the local field potential (LFP) as a measurement of neuronal activity in the brain, it remains a difficult signal to interpret. The LFP signal comprises activity originating in the electrophysiological features of neurons and network synapses, and sophisticated simulations of these signals involve a large number of nonlinear coupled differential equations. Simplified LFP approximation models have been developed in an effort to improve the computational efficiency of network LFP predictions, as well as gain a better understanding of the LFP signal using linear models. Two such linear LFP models are presented and evaluated, namely the hybrid- and kernel models. The hybrid model adapts simplified point-neuron spike times to synaptic activation times in biophysically detailed networks, removing the need to simulate the detailed neuron dynamics. Alternatively, the kernel method first spikes a population of neurons simultaneously to register the net LFP response per spike per neuron. This is subsequently combined with the spiking activity of a simulated network to obtain an approximation of the network LFP signal. This thesis presents a critical evaluation of the two linear LFP prediction methods by applying them to various network conditions and neuron models. A network of excitatory and inhibitory multicompartmental ball-and-stick neurons is first simulated and the ground-truth LFP signal is compared to the hybrid- and kernel method LFP approximations. These methods are then evaluated under two network conditions. The first in which the external drive/stimulus of the network is increased to up to four times stronger than the baseline, and another in which synchronous network spiking activity is induced. Neither network condition was found to jeopardize the linear method prediction performances, though the amplitude of the kernel method LFP prediction in the most synchronous network was found to be approximately two times larger than the ground-truth LFP signal. Finally, a layer 5b pyramidal cell was implemented to better represent a biophysically detailed system. The linear method LFP approximations of the L5b cell network were evaluated, and an external drive up to four times stronger than the baseline was used to investigate if the linear LFP approximation performances were consistent. The kernel method failed to capture high-frequency components of the ground-truth LFP signal in regions far from the synaptic input, and the hybrid method predictions were found to outperform the kernel method predictions in these regions. Despite this the kernel method was found to provide significant computational advantages, and both methods were overall successful in recreating the ground-truth signal. This demonstrates that a substantial amount of network LFP variability can be captured using linear spike-LFP models.

Chapter 1

Introduction

1.1 Thesis Context

The ongoing efforts to improve lifelike models of the brain are paramount to research fields within neuroscience today. Computational neuroscientists work to create replicas of the brain which can be simulated efficiently on large-scale computational clusters. One such model regards the primary visual cortex of mice comprising of 250,000 neurons at the Allen Institute for Brain Science in Seattle[1]. In these models, experimental data of biophysical properties of neurons are implemented into coupled differential equations which can simulate the evolution of such complex systems. The wide range of electrical brain signals which can be measured experimentally allow for a large corpus of data which can be compared with such simulations for benchmarking. The importance of computational brain replicas arises when considering the rigorousness of the mathematical descriptions we have of the brain. Several mathematical models can be constructed and hypotheses can be stated, but an intricate evaluation of the models is also necessary to verify the model performances.

1.2 Thesis Motivation

In the field of computational neuroscience in the 1960s, researchers observed the innate requirement for large-scale computation facilities to carry out simulations of the brain. The research at the time was predominantly focused on formalizing the mathematical equations which govern brain activity, and finding analytical solutions wherever possible[2]. With the computational means found today, large scale simulations are within reach, though computational bottlenecks are encountered when aiming for the sheer scale of the human brain. Methods which aim to simplify and approximate in vivo cortex activity are therefore imperative to improve computational efficiency.

The study at hand aims to evaluate two linear approximation models of neuronal network signals, applied to the simulation of a ~ 1 mm^2 patch of the primary visual cortex by Hagen et al. [3]. In particular, the thesis objective is to perform a rigorous evaluation of the two linear methods, referred to as the hybrid- and kernel methods. The hybrid method was a focal point of Hagen et al. [3], where it was utilized as an approximation technique of in vivo local

field potential (LFP) signals. The LFP signal is the low-frequency component of the extracellular potential, where the cutoff frequency is typically set to $\leq$ 500 Hz (though the definition varies[3, 4]). The LFP as a measurement of in vivo neuronal network activity has seen a resurgence in popularity in the past decade, though it is a difficult signal to interpret[5]. These linear methods are primarily meant to provide increased computational efficiency of neuronal network simulations, though a better understanding of the LFP signal can also be obtained by use of the linear models. Note that the kernel method was not mentioned as much as the hybrid method in Hagen et al. [3], and neither method has seen a thorough performance validation. The kernel method in particular is a promising technique to optimizing LFP simulations, and although the evaluation of both techniques is central to the thesis, the implementation and assessment of the kernel method is the focal point. Optimizing the fashion in which LFP is simulated for large networks of neurons yields insight into the dynamics at play, and if the optimized methods are to see continued application, they need to be systematically tested and evaluated.

1.3 Thesis Structure

The thesis aims to introduce the reader to the necessary theoretical background required for the analysis prior to the presentation of the methodology and results. Chapter 2 Theory describes a thoretical background of neuroscience, introduces the reader to neuron simulations, and finally describes the simulation techniques of neuronal networks and the LFP signal. This is followed by chapter 3 Methods, where the initial network configuration is described and the signal evaluation techniques are outlined. Following this is a thorough introduction to the hybrid- and kernel methods, and how these methods are implemented. Afterwards, a section explaining the limitations of the linear methods is presented, where the techniques used to test the linear methods are described. A biophysically detailed network of neurons is then implemented and the linear methods are tested on a more challenging network. Following the method descriptions are chapters 4 Results and 5 Discussion and Conclusion, where the method results are presented, followed by a discussion of the material. Potential future improvements are noted, and a conclusion of the study is finally stated.

Chapter 2

Theory

2.1 Neuroscience Background

The central cell of neuroscience is the neuron, a cell which, being quite simple on its own, can give rise to complex behaviour in larger networks. Neurons consist of various sections, all of which serve different functions within the cell. The neuron consists of a central compartment named the *soma*, and outwards-extending branches of *axons* and *dendrites*. Dendrites are further categorized into *basal* and *apical* dendrites. Figure 2.1 illustrates the basic biological characteristics describing a neuron. Note that signals from the neuron travel outwards along the axon and neural input comes from the various dendrites. The cell membrane separates the Extracellular Space (ECS) from the Intracellular Space (ICS). This membrane upholds a *membrane potential*, the relative voltage difference between these two spaces. This potential is generated by an ion imbalance between the ECS and ICS, regulated by channels and pumps which allow ions to pass through the membrane. The typical resting potential for neurons is around $\approx$-62 mV[6], and any deviances this potential has from the mean has a large impact on the neuronal membrane dynamics.

2.1.1 Membrane Characteristics

The membrane is *bilipid*, meaning that it is hydrophobic on the inside but hydrophilic on the outside, making for a barrier which separates the ECS and ICS plasma, an important characteristic to have to uphold the membrane potential.

Figure 2.2 illustrates a conceptualization of how the potential difference is measured on the two sides of the bilipid membrane. Something not included in the membrane illustration are the $\sim$100-200[9] types of ion channels which regulate the ion flow through the membrane. This ion flow of the membrane is controlled by *active* and *passive* channels. The difference between the two is that the *active* channels open and close based on various factors such as the membrane potential or the prevelance of certain types of bound molecules[9]. These active channels can produce an 'artificial' concentration gradient, and therefore require energy to pump. This energy comes from ATP, Adenosine triphosphate, an essential molecule for energy transport in biology. Meanwhile the *passive* ion channels simply allow ions to diffuse freely through the membrane depending either on the concentration gradient or electric forces. These

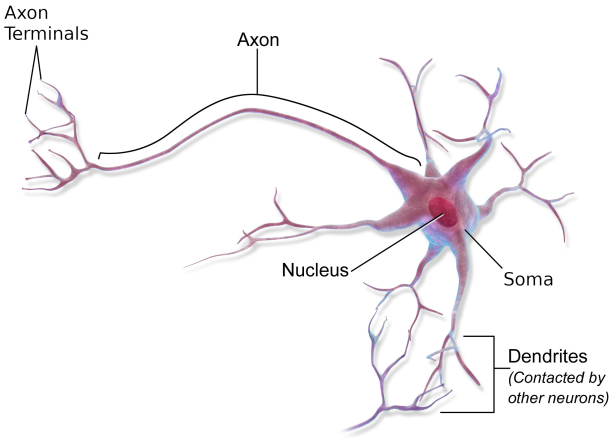

Figure 2.1: Figure illustrating the basic anatomy of a neuron cell. Adapted from [7]

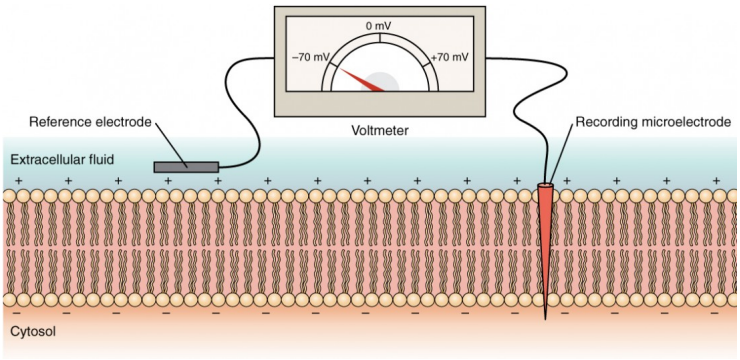

Figure 2.2: Figure illustrating the voltage caused by ion differences in the ECS and ICS fluids, referred to as Extracellular fluid and Cytosol, respectively. Copied from [8].

ion channels are thoroughly catalogued on several online sources[10, 11, 12] for more detail on the subject. The ions which are discussed most in the thesis are:

- Potassium, K^+
- Sodium, Na^+
- Chloride, Cl^-
- Calcium, Ca^{2+}

All these are ions which are prominent inside and outside the neuron, though the two central ones considered for the moment are the K^+ and Na^+ ions. In the ECS, there is a far larger Na^+ concentration, and in the ICS, the K^+ ion is far more prominant. The neuron dynamics are very dependent on the transfer of these ions through their respective active, voltage-gated Na^+ and K^+ channels[9]. These channels regulate the flow of the main charge carriers

which contribute to the *action potential* firing of the neuron, something which is explained in detail shortly.

Another central membrane characteristic is the *capacitive* property of the bilipid membrane. This capacitive impact arises from charges gathering at each side of the cell membrane as a result of the resting potential. This then has the properties of a capacitance plate, allowing for new for charge changes/currents through the membrane[1]. The capacitive current is one of multiple ways in which currents can flow through the membrane. There are many more transmembrane currents which can dynamically flow through the bilipid membrane which are described later on. Firstly though, the term neuron dynamics should be addressed, as it refers to action potential firing of neurons, the characteristic signal used for neuron-to-neuron communication.

2.1.2 Action Potential

The membrane can be stimulated in several ways by outer sources, from input from other neurons to artificial current injections. These stimuli change the membrane potential to be greater or lesser than the resting potential, and can cause the voltage-gated ion channels to change their states between *open* and *closed*, depending on the stimulus strength. If the membrane potential in the

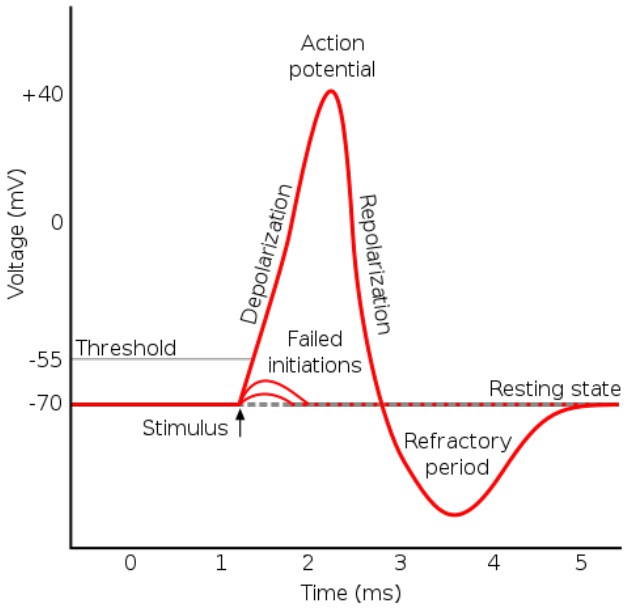

Figure 2.3: Conceptualization of the action potential. Copied from [14].

soma reaches a certain threshold potential (around ≈ -50 mV[6]), an irreversible process known as an action potential (AP) is set in motion. The voltage-gated Na^+ channels begin to open if the membrane potential surpasses the threshold potential, causing a surge of positively-charged Na^+ ions to flow into the

[1] It is worth noting that this membrane current is not a result of ions traveling through the membrane but is rather a purely capacitive characteristic. See to [13] for more on capacitors.

membrane. The flow of positive ions into the membrane causes the neuron to *depolarize*, meaning that the polarity caused by the charge surplus has been negated.

A concurrent opening of the voltage-gated K^+ channel takes place shortly after the depolarizing surge of Na^+ ions. This channel pumps positive K^+ ions out of the neuron, against the charge gradient. The opening of the K^+ channel comes about far slower than the Na^+ channel, allowing for depolarization to occur before the *repolarization* of the neuron. The slow nature of the K^+ channel also results in *hyperpolarization*, where the membrane potential becomes far more polarized than it otherwise is when resting. The full process of an action potential is described by figure 2.3, and the hyperpolarization state is illustrated by *refractory period* region, a period in which the neuron is unable to fire off another AP. Figure 2.3 only displays the membrane potential of a single measurement point in the neuron. The reality of the situation is that

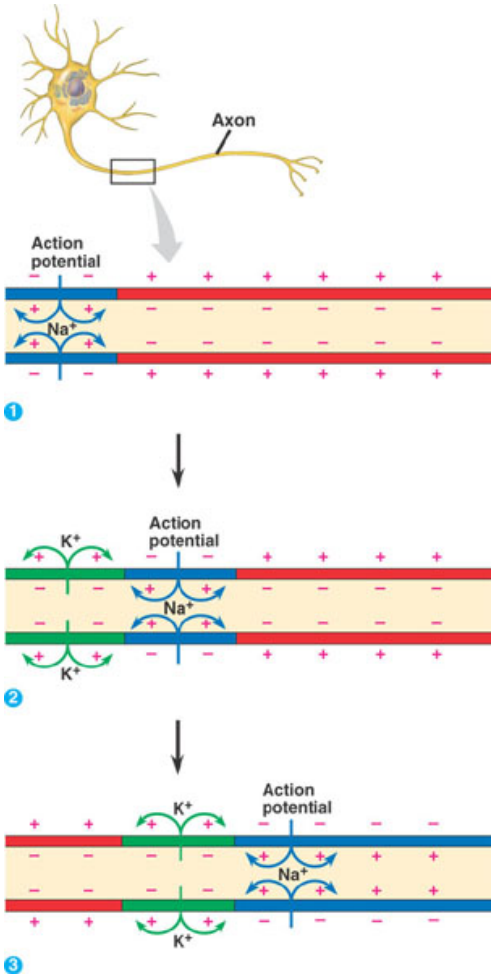

Figure 2.4: Action potential from the soma propagating down the central axon. Copied from [15].

this action potential begins in the soma and propagates down the axon. This is illustrated by figure 2.4, where the opening of the Na^+- and subsequently the K^+ ion channels propagates through the axon. The AP process involves a quick depolarization of the membrane potential which propogates from the soma outward. Although some so-called backpropogation of the AP goes to the dendrites, the signal mainly propagates through the axon to several terminals. These axon terminals connect to other neurons via *synapses*, the main communication tool between cells.

2.1.3 Synapses

Synapses are the basis for communication between neurons in a network. They ensure that an AP signal from a pre-synaptic neuron is properly conveyed to the post-synaptic neuron. As mentioned previously, synapses are found at the end of pre-synaptic axon terminals, connecting to the dendrites of the post-synaptic neuron. When an AP propagates down the axon terminals and into a synapse, a set of neurotransmitters are released from synaptic vesicles into the synaptic *cleft*, the space between the neurons. These neurotransmitters are subsequently received by various types of ion channels in the post-synaptic neuron membrane, creating a setting in which the post-synaptic dendritic membrane can either polarize or depolarize, depending on the synapse type. Figure 2.5 illustrates a

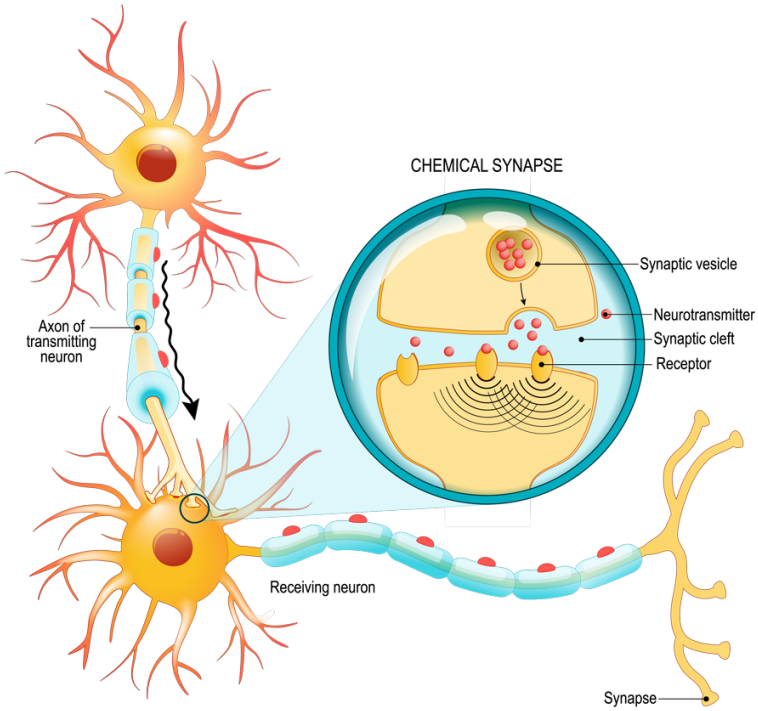

Figure 2.5: Illustration of a synaptic connection between an axon of one neuron and the dendrites of another. Closer inspection of the activity within the synaptic cleft is included. Figure copied from [16].

synaptic connection between two neurons in detail. The two central types of

synapses are *excitatory* and *inhibitory* synapses. The difference between the two is that they release different neurotransmitters into the synaptic cleft. Excitatory synapses typically release glutamate and acetylcoline, whereas inhibitory synapses release gamma-aminobutyric acid (GABA)[9]. Excitatory synapses increase the the post-synaptic membrane potential, bringing the post-synaptic neuron closer to the AP firing threshold potential, while opposite is true for inhibitory synapses. Typically, the excitatory synapses are placed at the apical dendrites and the inhibitory synapses are placed at the basal dendrites, closer to the soma. The synaptic stimulus to the dendritic branches is still noticed in the soma, though the distance between the dendrite and the soma causes the stimulus strength to diminish. Despite the synaptic signal being weakened by distance, the soma receives a multitude of signals from all other synapse locations in the dendrites, and sum of all such contributions guides the soma either away- or towards the action potential firing threshold.

2.2 Modeling of Neurons

A number of neuron simulation models which are relevant to the thesis are presented in the following chapter. Models with various levels of simulation complexity are described, and the tradeoff between model complexity and simulation efficiency is quite relevant in the context of neuronal modeling.

2.2.1 Traditional Neuron Models

In computational neuroscience, the neuron models typically utilize *quasi-ohmic* approximations of transmembrane currents densities I:

$$I_x = g_x(V - E_x) \tag{2.1}$$

where g_x is the membrane conductance per unit area, given in mS cm^{-2}, V is the membrane potential in mV, and E_x is the resting membrane potential in mV. The current density I_x then has units µA cm^{-2}. Note that positive ion currents are currents which travel from ICS to ECS, by convention. The factor $(V - E_x)$ is the *driving force* of the ion, as the equilibrium is always reached when the membrane potential equals the resting potential $V = E_x$, and driving force equals zero. Here, x is some ion traveling between the ECS and ICS $x \in (\mathrm{K}^+, \mathrm{Na}^+, \mathrm{Cl}^-, \mathrm{Ca}^{2+})$.

RC-Circuit Neuron

The RC-circuit neuron model allows for neuron dynamics to be modeled as an RC-circuit. This involves combining the individual ion channel properties into general membrane characteristics $x \rightarrow$m using Thévenin's theorem[9]:

$$I_\mathrm{m} = g_\mathrm{m}(V - E_\mathrm{m}), \tag{2.2}$$

where the parameters and units follow equation 2.1, and the ion-channel specifics have been combined into a single membrane current expression. The current I_cap which describes the capacitive characteristics of the membrane can additionally be modeled as[9]:

$$\frac{\partial V}{\partial t} = \frac{1}{C_\mathrm{m}}\frac{\partial q}{\partial t} = \frac{1}{C_\mathrm{m}} I_\mathrm{cap}, \tag{2.3}$$

$$\Rightarrow I_\mathrm{cap} = C_\mathrm{m}\frac{\partial V}{\partial t}, \tag{2.4}$$

where C_m is the specific membrane capacitance, given in µF cm^{-2}, and V is the membrane potential mV. Time is typically measured in ms, such that the capacitive current has units µA cm^{-2}. The relation between the capacitive current I_cap and other transmembrane currents I_m is found using current-conservation in the ICS and ECS, where Kirchoff's law yields:

$$I_\mathrm{cap} + I_\mathrm{m} = 0 \tag{2.5}$$

$$C_\mathrm{m}\frac{\partial V}{\partial t} = g_\mathrm{m}(E_\mathrm{m} - V), \tag{2.6}$$

here, I_m represents all currents into the membrane due to ion transmission.Figure 2.6 illustrates a conceptual circuit which can be used to describe neuron membrane dynamics. Note that the specific membrane resistance R_m in units of Ω cm^2 is inversely related to the membrane conductance per unit area $g_\mathrm{m} = 1/R_\mathrm{m}$.

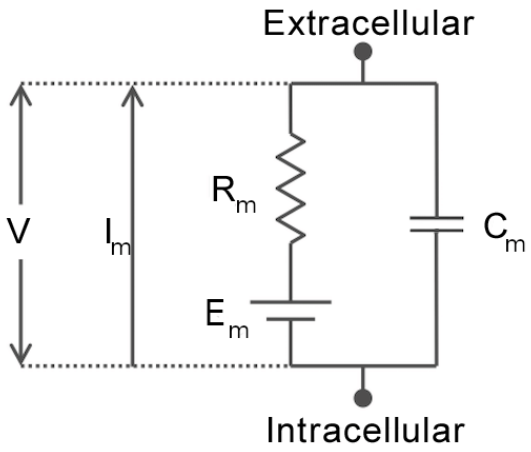

Figure 2.6: Figure illustrating the basic RC circuit graph for the neuron membrane. Figure adapted from [17].

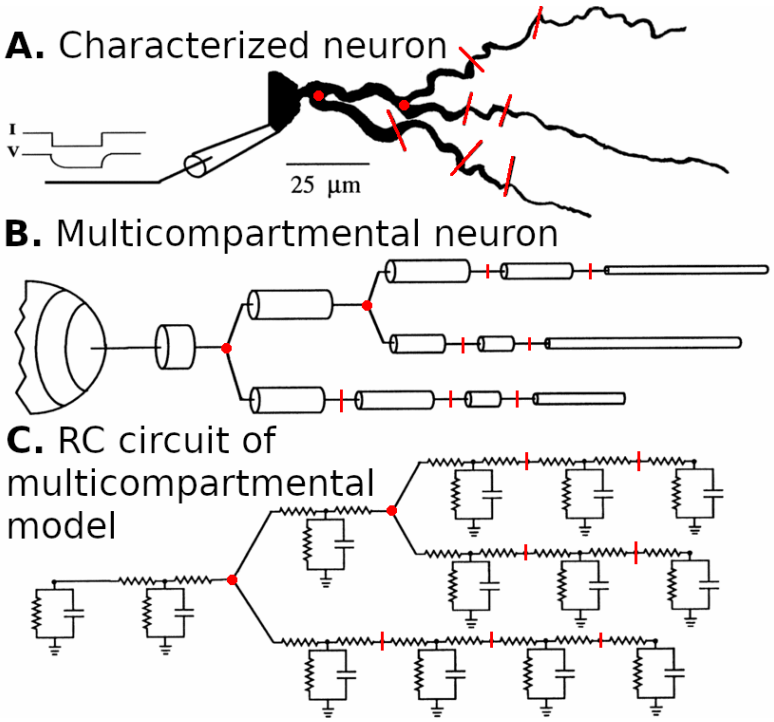

Figure 2.7: Conceptualization of how a measured, characterized neuron (**A**) can be configured as a multicompartmental neuron (**B**), and subsequently simulated as a multicompartmental RC circuit (**C**). Figure adapted from [18].

2.2.2 Multicompartmental Neuron Models

The RC-circuit model of the neuron relates to what is known as multicompartmental neuron models. This method of neuron modeling involves setting up a multitude of connected RC circuits to represent various 'compartments' of the cell. Each such compartment is then connected to its neighboring compartments by an axial resistance R_a such that compartments can transfer current axially, as well as through the membrane into the ECS. Figure 2.7 illustrates a conceptual chronological approach to how to simulate a neuron this way. Firstly, the quantities and qualities of the neuron are measured and recorded in the lab, as illustrated by section (**A**) of the figure. This measurement step includes the measurement of the morphology of the neuron - such as placements and widths of dendritic branches - to measuring specific neuron parameters such as the membrane capacitance C_m and resistivity R_m at a number of sites across the morphology.

Once this is done, one can split the neurons into multiple cylindrical sections depending on the level of granularity which is desired. In the example figure presented, there are 7 such splits of the neuron, illustrated by the red lines. These should optimally be done to section off regions which have very similar parameters and morphologies, and there is a tradeoff between accuracy and computational efficiency here. Branching points are also included as two red dots in figure 2.7, where the circuit splits as showed in section (**C**) of the figure. An important step from sections (**A**) to (**B**) in figure 2.7 is the assignment of the cylindrical dimensions of each compartment. These dimensions are important to evaluate closely as the length and diameter determines how much membrane surface area the ICS of that compartment shares with the ECS. The curved surface area of the cylinder is typically regarded as the only area in contact with the ECS, such that the membrane area of each compartment is given by $A = \pi dl$, where l is the cylinder length and d is the cylinder diameter.

In measuring the characteristic neuron in step (**A**), quantities such as the specific membrane resistance R_m and specific membrane capacitance C_m should be determined. Other measured quantities include the membrane resting potentials E_m and axial resistance between compartments R_a. In the RC circuit model, the axial resistance determines the voltage drop between compartments, and is closely linked to the so-called decay factor λ. This factor depends on both the specific membrane resistance R_m and the axial resistance R_a, and is given by the following expression[9]:

$$\lambda = \sqrt{\frac{dR_m}{4R_a}} = \sqrt{\frac{r_m}{r_a}}, \tag{2.7}$$

where $r_m = R_m/(\pi d)$ is the membrane resistance per circumference, and $r_a = 4R_a/(\pi d^2)$ is the axial resistance per cross sectional area. As an example following Sterratt et al. [9], inserting parameters such as d=1 µm, $R_a = 35.4\ \Omega$ cm and $R_m = 6000\ \Omega\ \text{cm}^2$ yields a characteristic decay factor $\lambda \approx 1029$ µm. Thus, injecting a current into one end of a dendrite, then the membrane potential has dropped by $1/e \approx 36.8\%$ after 1029 µm. As a final note on the matter, a general rule when determining the length of a compartment is asserting a so-called electrotonically compact compartment, where $l << \lambda$. If the length of the compartment is far smaller than the characteristic voltage decay constant, then the compartment size is considered appropriate.

2.2.3 Hodgkin-Huxley Models

The Hodgkin-Huxley (HH) formalism from Hodgkin et al. [19] introduces so-called activation/gating variables into the quasi-ohmic models. The motivation behind this development was that previous models could not produce accurate AP firings as was observed in neurons. These activation variables simulate the conductances for the Na^+ and K^+ ions as voltage- and time-dependent functions, such that the transmembrane Na^+ and K^+ currents in the soma are given by:

$$I_{\mathrm{Na}} = g_{\mathrm{Na}}(V,t)\,(V - E_{\mathrm{Na}})\,, \tag{2.8}$$

$$I_{\mathrm{K}} = g_{\mathrm{K}}(V,t)\,(V - E_{\mathrm{K}})\,. \tag{2.9}$$

The driving force still functions as described previously, though the conductances g_{Na} and g_{K} are modeled more dynamically. The HH formalism models the conductances as[9, 19]:

$$g_{\mathrm{Na}}(V,t) = \bar{g}_{\mathrm{Na}} \cdot n^4(V,t) \tag{2.10}$$

$$g_{\mathrm{K}}(V,t) = \bar{g}_{\mathrm{K}} \cdot m^3(V,t) \cdot h(V,t), \tag{2.11}$$

where $\bar{g}_{\mathrm{Na}}$ and $\bar{g}_{\mathrm{K}}$ are constants and the parameters n, m and h are voltage- and time-dependent gating variables. Such variables are probabilistic, $(n,m,h) \in [0,1]$, such that $\bar{g}_{\mathrm{Na}}$ and $\bar{g}_{\mathrm{K}}$ are the maximal conductance values. The full HH model is then found using Kirchoff's law, where the membrane current I_{m} is split into three separate currents

$$I_{\mathrm{m}} = I_{\mathrm{L}} + I_{\mathrm{K}} + I_{\mathrm{Na}}, \tag{2.12}$$

and Kirchoff's law yields the HH formalism:

$$I_{\mathrm{cap}} + I_{\mathrm{L}} + I_{\mathrm{K}} + I_{\mathrm{Na}} = 0 \tag{2.13}$$

$$\rightarrow C_{\mathrm{m}}\frac{\partial V}{\partial t} = -\bar{g}_{\mathrm{L}}\,(V - E_{\mathrm{L}}) - \bar{g}_{\mathrm{K}} n^4\,(V - E_{\mathrm{K}}) - \bar{g}_{\mathrm{Na}} m^3 h\,(V - E_{\mathrm{Na}})\,. \tag{2.14}$$

This is the general expression for the membrane dynamics under the HH formalism. Where (n,m,h) are voltage- and time-dependent functions which are not specified in the thesis. More information about how these are modeled can be found at Hodgkin et al. [19]. I_{L} is the generalized leak current which accounts for other passive membrane ion transmission which are not related to the K^+ and Na^+ ion dynamics. A central assumption of the HH model is that there are enough ion channels in the membrane to approximate that the probabilities (n,m,h) equal the fraction of open gates. Once these activation variables are properly tuned and modeled, the HH model provides a simulation of AP firing in neurons, earning the developers the nobel prize in Physiology or Medicine in 1963[20].

2.2.4 Simplified Neuron Models

The complexity of individual neuron simulations often gets in the way of large scale network simulations. If the individual neuron detail level is too great, then larger network simulations are impractical. Neuron models which attempt to minimize the computational requirements of each neuron are developed for this reason, and a description of simplified neuron models is presented. Typical simplifications which can be applied to the network are:

1. Reduction of the number of compartments which each neuron is comprised of.
2. Skip modeling AP shapes, opting instead for *firing rate* models such as:
   (a) Integrate-and-Fire (IF) family of models.
   (b) Simplified AP generation dynamics with the Morris-Lecar-[21], or the Fitzhugh-Nagumo[22] models.

Ball-and-Stick Neuron Model

One neuron morphology simplification is the ball-and-stick neuron model. The study at hand utilizes this model throughout, as it is highly computationally efficient. This morphology is split into two central sections - the ball and the stick. The ball section is meant to represent the soma, while the stick represents the apical dendrites. These are then connected together such that current can flow axially between them. Each section is initialized with unique characteristics. The ball section is given characteristics resembling the soma, where the membrane is capable of firing APs. The dendritic section is set to have compartments with passive membrane conductances, such that the compartments are not capable of AP firings. The AP firing of the soma can be modeled using either the active Na^+ and K^+ conductances of the HH formalism, or using other simplified neuron firing models.

Neural Firing Models

An additional simplification approach aims to reduce the amount of coupled differential equations by simply modeling *when* the neuron fires, removing the complexities of the membrane dynamics. The HH model for instance has four coupled ODEs[19, 23], whereas the Morris-Lecar and Fitzhugh-Nagumo models both reduce it to two coupled ODEs[21, 22].

Integrate-and-Fire Neurons

Integrate-and-Fire (IF) neuron models are highly computationally efficient. The IF neuron model involves monitoring the membrane potential in the soma in relation to some voltage threshold θ, firing an AP if the membrane potential in the soma surpasses the threshold, and resetting the membrane potential to the resting value. Typically, this threshold is set to be around $\theta \approx -50$ mV[24], and the value is often accompanied with some noise to increase stochasticity of the network. Several IF neuron model modifications have been made to incorporate various additional observed phenomena into the IF neuron. This yields a large IF-neuron family of models, a few such model modifications being[25]:

- Leaky Integrate-and-Fire neuron model (LIF)

$$C_{\mathrm{m}} \frac{\partial V}{\partial t} = I - g_{\mathrm{m}}(V - E_{\mathrm{m}}) \tag{2.15}$$

- Quadratic Integrate-and-Fire neuron model (QIF)

$$C_{\mathrm{m}} \frac{\partial V}{\partial t} = I - g_{\mathrm{m}} \frac{(V - E_{\mathrm{m}})(\theta - V)}{(\theta - E_{\mathrm{m}})} \tag{2.16}$$

- Exponential Integrate-and-Fire neuron model (EIF)

$$C_{\mathrm{m}}\frac{\partial V}{\partial t} = I - g_{\mathrm{m}}\left(V - E_{\mathrm{m}} - \Delta t \cdot \exp\left(\frac{V-\theta}{\Delta t}\right)\right), \tag{2.17}$$

where I is a general input current. Note that these models often share a similar approach to refractory periods. A typical approach is to start integration of the membrane potential at a time Δ^{abs} after AP firing. Δ^{abs} is an absolute refractory time, and is typically chosen to be in the range $0 < \Delta^{\mathrm{abs}} < 5$ ms[26]. Despite these models performing well in their own ways, it is important to note that one of the most central characteristics seen in vivo is noisy signaling between cells. The introduction of stochasticity and variability is something which was briefly discussed in relation to the threshold potential θ in the IF Neuron context, and is a factor which is very important in the resulting variability of the system.

Neural Firing Variability, the Stein Model and Poisson Distributions

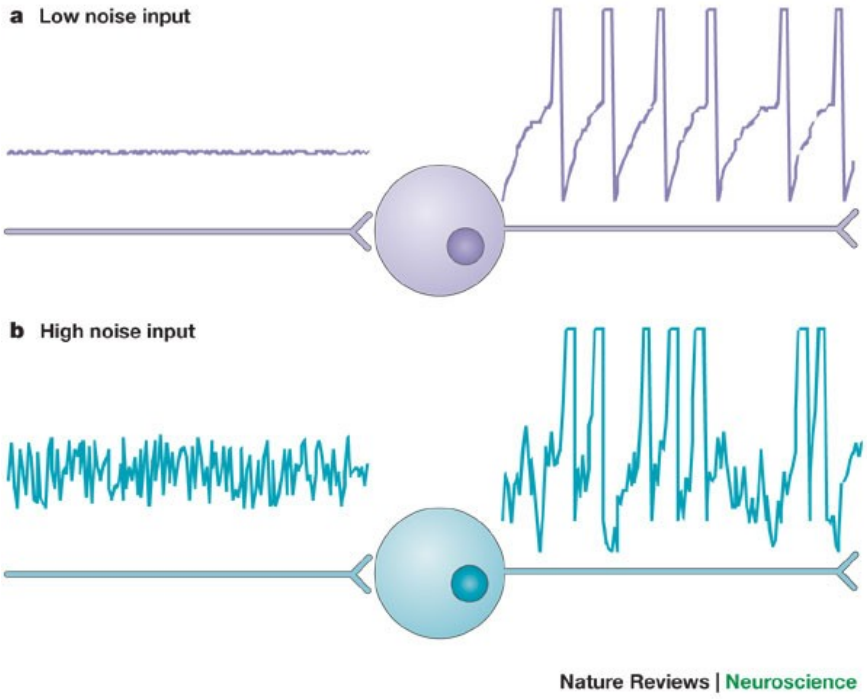

Figure 2.8: Intra-spike-interval (ISI) variability produced by high-noise input. In this case noise refers to a large combination of both excitatory and inhibitory input from external sources into the soma. Figure copied from [27].

The intra-spike-intervals (ISIs), defined as the time interval between a pair of AP firings of a single neuron, are quite regular if the input to each neuron has little to no noise. This is problematic as we know from observations that in vivo neuron spiking is irregular[27]. The impact of variability to neuron input is illustrated in figure 2.8, where the AP firing of the neuron with the noisiest

input has the most variability. A source of neural firing variability is included in the models to reproduce the stochasticity observed in vivo.

A way of modeling the variability in neuron ISIs is assuming that spike trains are Poissonian[28, 29, 30]:

$$f_{\mathrm{Ps}}(k;\lambda) = \frac{\lambda^k e^{-\lambda}}{k!}, \tag{2.18}$$

where λ is the expected rate of occurrences and k is the number of occurrences. Such Poissonian distributions have characteristics which resemble the behavior of network spiking activity:

- The probability of occurrence of the event (the firing of an AP in this case) is the same with each small increment of time[27].
- The exponentially decaying interspike interval distribution observed in vivo is characteristic of a poissonian distribution.

This insight which was provided by Stein [28], and the modeling of spike rate statistics is an important one to the study at hand due to the external drive needs of a network. In an effort to create network activity, each neuron is connected a number of excitatory 'external' neurons. Without an external drive, the network would reach a resting state if unstimulated. These external stimulating synapses have firing rates which are picked from the poissonian distribution from equation 2.18, and are only excitatory.

2.2.5 Synaptic Models

The typical way in which synaptic connections between neurons are modeled is to set up a quasi-ohmic approximation which determines the current injected into the post-synaptic neuron following synaptic activation. Such a quasi-ohmic expression can be stated as:

$$I_{\mathrm{syn}} = g_{\mathrm{syn}} \left(V - E_{\mathrm{syn}}\right), \tag{2.19}$$

where g_{syn} is the conductance of the synapse, V is the post-synaptic membrane potential and E_{syn} is the synaptic reversal potential. E_{syn} takes on two values in the current study:

$$E_{\mathrm{syn}} \approx \begin{cases} 0 \text{ mV for AMPA and NMDA receptors} \\ -80 \text{ mV for GABA receptors.} \end{cases} \tag{2.20}$$

These driving forces reflect the fact that AMPA and NMDA receptors are excitatory whereas GABA is inhibitory, as was described in section 2.1.3. Two central models of synaptic current injections I_{syn} are introduced and implemented: the conductance- and the current-based synapse models. The conductance-based synapse model is as follows:

$$g_{\mathrm{syn}} = \bar{g}_{\mathrm{syn}} s_{\mathrm{syn}} \tag{2.21}$$

$$I^{\mathrm{g}}_{\mathrm{syn}}(V,t) = \bar{g}_{\mathrm{syn}} s_{\mathrm{syn}}(t) \left(V - E_{\mathrm{syn}}\right) \tag{2.22}$$

where $I^{\mathrm{g}}_{\mathrm{syn}}(V,t)$ is the post-synaptic current injection using the conductance-based synapse model, V is the post-synaptic membrane potential, $\bar{g}_{\mathrm{syn}}$ is the

maximum conductive value of the synapse, and $s_{\text{syn}}(t)$ is a function which models synaptic kinetics[31]:

$$s_{\text{syn}}(t) = \eta(\tau_1, \tau_2)\left[\exp\left(\frac{-(t-t_s)}{\tau_2}\right) - \exp\left(\frac{-(t-t_s)}{\tau_1}\right)\right]\Theta(t-t_s), \quad (2.23)$$

where τ_1 and τ_2 are characteristic rise- and decay time constants of the synapse, respectively. The rise time determines how quickly the synaptic conductance reaches the peak value $\bar{g}_{\text{syn}}$, while the decay time determines how long it takes for this value to taper off, or reduce back down to zero. These constants are restricted by $\tau_1 < \tau_2$. $\Theta(t-t_s)$ is known as the heaviside step function, given by:

$$\Theta(t-t_s) = \begin{cases} 1 \text{ if } t \geq t_s \\ 0 \text{ else} \end{cases} \quad (2.24)$$

where t_s represents the time in which the post-synaptic current injection occurs. This captures the time taken for the AP to arrive at the synapse, time of vesicle release, time for the neurotransmitters to traverse the synaptic cleft, and time taken for the transmitters to bind to the post-synaptic receptors. The heaviside step function ensures that the current injection into the post-synaptic neuron equals zero for all times prior to the completion of these processes. The value $\eta(\tau_1, \tau_2)$ from equation 2.23 is a normalization factor for some combination τ_1, τ_2, given by:

$$\eta(\tau_1, \tau_2) = \left(\exp\left(-t_{\text{peak}}/\tau_2\right) - \exp\left(-t_{\text{peak}}/\tau_1\right)\right)^{-1}, \quad (2.25)$$

$$t_{\text{peak}} = \frac{\tau_2\tau_1}{\tau_2 - \tau_1}\log\left(\frac{\tau_2}{\tau_1}\right). \quad (2.26)$$

This normalization factor ensures that $0 \leq s_{\text{syn}} \leq 1$, such that $0 \leq g_{\text{syn}} \leq \bar{g}_{\text{syn}}$. The second synapse model which is vital to the study at hand is the current-based synapse model. This model opts for the following expression for synaptic current injections:

$$I^{\text{i}}_{\text{syn}}(t) = \bar{I}_{\text{syn}} s_{\text{syn}}(t) \quad (2.27)$$

where $\bar{I}_{\text{syn}}$ is the maximum current value, and $s_{\text{syn}}(t)$ models the synaptic kinetics as described in equation 2.23. The differences between the conductance- and current-based synapse models from equations 2.22 and 2.27 are worth noting, as conversion between them is a central subject of this study. The conductance-based synapse model expression $I^{\text{g}}_{\text{syn}}(V,t)$ is a function of both post-synaptic membrane potential and time, while the current-based synapse model only varies with time $I^{\text{i}}_{\text{syn}}(t)$. This means that the current-based synapse model is linear, and is not dependent on the dynamics of the membrane potential V inside the post-synaptic cell like the conductance-based model is.

This is important later on, as the linearized LFP techniques implement the linear current-based synapse model. The conversion between the conductance- and current-based synapse maximum values $\bar{g}_{\text{syn}}$ and $\bar{I}_{\text{syn}}$ (later referred to as weights) is a crucial step in linearizing the system, and is performed by the multiplication of a driving force:

$$\bar{I}_{\text{syn}} = \bar{g}_{\text{syn}}\left(\bar{V} - E_{\text{syn}}\right). \quad (2.28)$$

Note that the synaptic maximum values $\bar{g}_{\mathrm{syn}}$ and $\bar{I}_{\mathrm{syn}}$ are constants, such that the conversion driving force $\left(\bar{V} - E_{\mathrm{syn}}\right)$ must also be a constant. E_{syn} is given by the values in equation 2.20, such that a constant post-synaptic membrane potential $V \rightarrow \bar{V}$ must be determined for the conductance- to current-based synapse model procedure. The fashion in which the study chooses to determine the constant post-synaptic membrane potential $\bar{V}$ is by calculating the mean value of the mean somatic membrane potential for each neuron in the network:

$$\bar{V} = \frac{1}{N} \sum_{j=1}^{N} \frac{1}{N_{\mathrm{t}}} \sum_{i=1}^{N_{\mathrm{t}}} V_{\mathrm{soma},j}(t_i), \tag{2.29}$$

where N is the total number of neurons in the network and N_{t} is the total number of time points in the simulation. $V_{\mathrm{soma},j}(t_i)$ is the somatic potential value of neuron j at time point t_i. This is the value which is assigned for the conductance- to current-based synapse model weight conversion $\bar{g} \rightarrow \bar{I}$, and the procedure is described in greater detail in section 3.4.2.

2.3 Network Dynamics

The upcoming section regards the simulation of networks of neurons, from localized multi-neuron interactions to large scale cortex simulations. A central challenge which arises in such networks is how measurements are conducted in the lab, and how those measurements can be replicated in simulations. Several brain activity measurement methods have recently been popularized such as Magnetic Resonance Imaging (MRI)[32], Magnetoencephalography (MEG)[33], Electroencephalography (EEG)[34], and Electrocorticography (ECoG)[35]. Many of these measurements are logged in the *Handbook of Neural Activity Measurement*[36]. The thesis has one such neuronal activity measurement at its focal point, the *Local Field Potential*.

2.3.1 Local Field Potential

The Local Field Potential (LFP) is a general term used for low-frequency potential signals which arise in the ECS from neuronal network activity in the brain. Low-frequency recordings in this context refer to frequencies less than 500 Hz[4], though the definition varies. There are several reasons in which the LFP signal has gained more traction as a neural network activity indicator in recent times. One of the reasons is that the main neuronal activity measurements, namely AP firing and synaptic activity, release a large amount of ions into the ECS. The AP firing of neurons was previously mentioned to take in a large amount of Na^+ before releasing K^+, and the post-synaptic membrane stimulus results in either a large release or a large intake of ions, depending on the type of synapse. These transmembrane currents from ICS to the ECS result in voltage changes in the ECS which are recorded by the LFP.

As opposed to ECOG and EEG measurements, experimental recordings of the LFP involve *invasive* measurement techniques, meaning that the insertion of a recording electrode into the brain is necessary for data collection. The recording electrode is sensitive to voltage changes, and can record extracellular potential in various sites in the brain. This results in a time series of extracellular potential signals which record the neuron activity at various sites, revealing characteristics about the network activity. The LFP is then obtained by low-pass filtering this signal at a predefined cutoff frequency. For more on the resurgence of LFP as a neural network measurement tool, see to the article by Einevoll et al. [5]. Understanding the LFP as a neural network activity signal is a central component for the study at hand. Among other objectives, the current study aims to improve the computational efficiency of network LFP simulations and understand the signal better.

The fashion in which the extracellular potential and LFP is simulated using multicompartmental neurons is presented in the following chapter. Each compartment in the multicompartmental model from section 2.2.2 is capable of current transfer to neighboring compartments, as well as transmembrane currents. This means that all compartments of the neurons in the simulated network can contribute to the total extracellular potential signal by transmembrane currents. The recording electrode is sensitive to potential changes from transmembrane currents both close to- and far away from the electrode positioning. The simulation procedure follows the phenomena observed in the lab, where the distance between the electrode and the transmembrane current sites

determines the strength of the registered potential signal. The strength is also determined by the conductivity of the extracellular space, and the link between a source of current and the resulting electric potential field in a surrounding volume conductor is described by volume conduction theory.

2.3.2 Volume Conductor Theory

Volume Conductor Theory (VCT) is the theory describing an electric potential recording of a current source, where the two are separated by some distance [37]. More importantly, VCT can link a current source to the resulting electric potential field within a medium, where the medium can have various conductive properties. VCT is not specific to the extracellular potential of the brain, but is very applicable in this context.

The many transmembrane currents from the compartments of a neuron network produce an intricate electric potential field in the ECS fluid. The conductive properties of the ECS fluid are impactful on the resulting fields from the current sources, and the ECS fluid conductance is a quanitity which can be measured in the lab. A recording device sensitive to potential changes can record the potential signal in a region of the field, and the electrodes which are placed in the brain serve this purpose. A key assumption of VCT is describing the ECS fluid as a continuous extracellular domain, and the ICS as a discrete intracellular domain [9]. The key to understanding how these extra- and intracellular domains interact is by the uptake and release of currents in the ICS compartments. There are multiple cell processes capable of producing transmembrane currents I_{m}, and assuming a current I_{m} is released into the ECS, then VCT states that the current density function $\rho(r)$ in a sphere of radius r around the injection point is given by[9]:

$$\rho(r) = -\sigma_{\mathrm{e}} \frac{\partial \phi}{\partial r}, \tag{2.30}$$

where σ_{e} is the conductivity of the ECS fluid, and ϕ is the extracellular potential. Using current conservation in a sphere around the source yields:

$$I_{\mathrm{m}} = \rho(r) \cdot 4\pi r, \tag{2.31}$$

$$\Rightarrow I_{\mathrm{m}} = -\sigma_{\mathrm{e}} \frac{\partial \phi}{\partial r} \cdot 4\pi r \tag{2.32}$$

by insertion of equation 2.30. Rearranging the expression yields the following differential equation describing the relationship between a current injection I_{m} and the resulting potential field ϕ in the ECS:

$$\frac{\partial \phi}{\partial r} = \frac{-I_{\mathrm{m}}}{4\pi\sigma_{\mathrm{e}} r^2}. \tag{2.33}$$

Integration then yields the ECS potential expression for the current source I_{m} to be:

$$\frac{\partial \phi}{\partial r} = \frac{-I_{\mathrm{m}}}{4\pi\sigma_{\mathrm{e}} r^2} \tag{2.34}$$

$$\phi(r) = \frac{I_{\mathrm{m}}}{4\pi\sigma_{\mathrm{e}} r}, \tag{2.35}$$

where I_{m} is some current injection into the ECS, σ_{e} is the conductivity of the ECS fluid, and r is the distance between the measurement point of ϕ and the current injection point. Notice also that $\phi \to 0$ for $r \to \infty$, and $\phi \to \infty$ for $r \to 0$. The latter is referred to as a mathematical singularity, and should be handled carefully when implementing VCT numerically.

This expression can be superpositioned, such that additional terms can be added linearly without interactive effects[38]. If there are multiple current injections $I_{\mathrm{m},n}$ at various positions $r_{\mathrm{m},n}$, then the ECS potential in position $\vec{r}$ is given by:

$$\phi(\vec{r}) = \frac{1}{4\pi\sigma_{\mathrm{e}}} \sum_{n} \frac{I_{\mathrm{m},n}}{|\vec{r} - \vec{r}_{\mathrm{m},n}|}, \tag{2.36}$$

where $\phi(\vec{r})$ is the extracellular potential field value at the point $\vec{r}$, and $\vec{r}_{\mathrm{m},n}$ is the vector pointing at current source $I_{\mathrm{m},n}$. This ties closely into the multicompartmental theory of neurons, where each compartment can provide a current injection into the ECS through transmembrane currents.

Note the distance metric r is transformed into a vector $\vec{r}$, such that the current injection points $\vec{r}_{\mathrm{m},n}$ are described by coordinates (r_x, r_y, r_z), such that $\vec{r} = r_x\hat{e}_x + r_y\hat{e}_y + r_z\hat{e}_z$, where $\hat{e}_d$ is the unit vector of dimension d. This yields the distance from the measurement point $\vec{r}$ to the current injection points $\vec{r}_{\mathrm{m},n}$ to be the absolute value of the combined differences between each coordinate:

$$|\vec{r}_1 - \vec{r}_2| = \sqrt{(r_{x,1} - r_{x,2})^2 + (r_{y,1} - r_{y,2})^2 + (r_{z,1} - r_{z,2})^2} \tag{2.37}$$

2.3.3 Multicompartmental Neuron LFP

Applying VCT to calculations of the extracellular potential fields of neuronal networks is largely summarized by equation 2.36. A number of restrictions are however placed on the amount of current $I_{\mathrm{m},n}$ which passes through the membrane of compartment n. A central constraint to transmembrane currents is current conservation and Kirchoff's law.

Kirchoff's law states that the net current flow across the neuron membrane is equal to zero, and dictates that the total positive transmembrane current $I_{\mathrm{m},n}$ into the ICS must be followed by an equal amount into the ECS. This means that the sum of the currents which pass through the neuron membrane cancel out:

$$\sum_{n=1}^{n^{\mathrm{seg}}} I_{\mathrm{m},n} = 0, \tag{2.38}$$

for all transmembrane currents of a neuron at any given time. $I_{\mathrm{m},n}$ is the transmembrane current of compartment n, and n^{seg} is the total number of compartments in the neuron. Recalling that positive currents are defined as currents moving from the ICS to the ECS by convention[9], the positive currents $I_{\mathrm{m},n} > 0$ are referred to as sources, and the negative currents $I_{\mathrm{m},n} < 0$ are referred to as sinks. A stimulated neuron acts as a dipole with this source-sink pair, and this can be visualized by a two-compartment neuron model.

The two-compartment neuron model has one compartment representing the soma, and another to represent the apical dendrites. A positive stimulus of the dendritic compartment results in a current-sink in the surrounding ECS field.

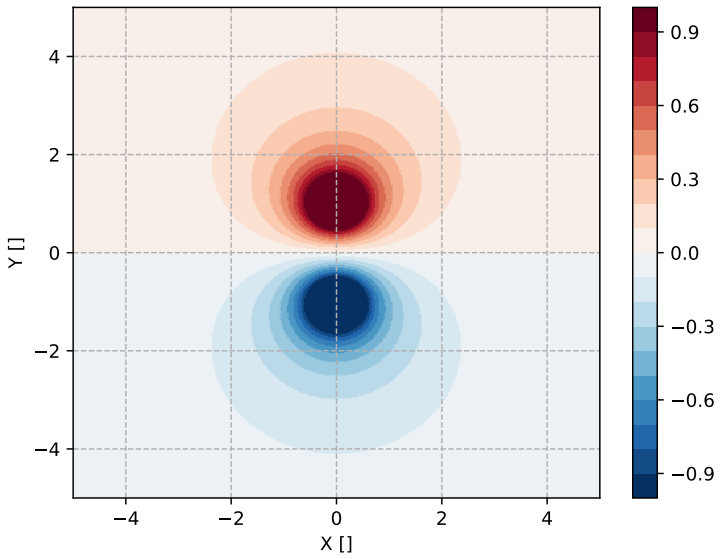

Figure 2.9: Dimensionless conceptualization of the potential pattern produced by a source-sink dipole. The current source- and sink are placed in $(0, 1)$ and $(0, -1)$, respectively. The potential value colorbar is capped at ± 1 in order to see the resulting dipole field patterns. In truth, the value of the potential diverges to $\pm\infty$ as the field measurement approaches the source/sink points. Image generated using the `misc/dipole_conceptualization.py` script[39].

The somatic compartment then releases an equal and opposite current into the ECS, acting as a current-source. This is visualized by figure 2.9, where equation 2.36 is superpositioned, with a positive current in $(0, 1)$, and a negative current in $(0, -1)$.

In a larger network of multicompartmental neuron models, the current contributions from each compartment are far more intricate, and all neurons are taken into consideration for the extracellular potential field. For a recording electrode placed at $\vec{r}$, the extracellular potential then equals the contribution of all compartments for each neuron in the network:

$$\phi(\vec{r}) = \frac{1}{4\pi\sigma_e} \sum_{j=1}^{N} \sum_{n=1}^{n_j^{\text{seg}}} \frac{I_{\text{m},jn}}{|\vec{r} - \vec{r}_{\text{m},jn}|}, \tag{2.39}$$

where $\vec{r}_{\text{m},jn}$ is the vector pointing at that the transmembrane current $I_{\text{m},jn}$ from compartment n of neuron j. N is the total number of neurons in the network, and n_j^{seg} is the total number of compartments for neuron j. These currents are still constricted under Kirchoff's law, such that

$$\sum_{n=1}^{n_j^{\text{seg}}} I_{\text{m},jn} = 0 \tag{2.40}$$

for all neurons $j \in N$. It is worth mentioning that the implemented VCT assumes an infinite, isotropic (same in all directions), homogeneous (same in all

positions), and ohmic (frequency-independent) extracellular medium, such that the conductivity σ_e from equation 2.35 is represented by a scalar[3]. There are models which include varying spatial conductivities such that σ_e includes grey/white matter modeling[9], though the current model is based on well established VCT from Rall et al. [40] and Holt et al. [41]

Line-Source Potential Expression

The extracellular potential field value ϕ described in equation 2.39 is what is known as a point-source model of the transmembrane current. In this model, all the transmembrane current $I_{\mathrm{m},jn}$ from compartment n in neuron j originates in a single point $\vec{r}_{\mathrm{m},jn}$ in the ECS.

As was described in section 2.2.2, compartments are often set as cylinders in the multicompartmental model. The membrane is then represented by the curved surface area of the cylinder, and the extracellular potential model is modified to account for currents distributed across this membrane [42]:

$$\phi(\vec{r}) = \frac{1}{4\pi\sigma_e}\sum_{j=1}^{N}\sum_{n=1}^{n_j^{\mathrm{seg}}} I_{\mathrm{m},jn}\int \frac{1}{|\vec{r}-\vec{r}_{\mathrm{m},jn}|}d\vec{r}_{\mathrm{m},jn}. \tag{2.41}$$

This is known as the line-source approximation, and is obtained by integrating equation 2.39 such that the transmembrane current $I_{\mathrm{m},jn}$ is distributed evenly along the center axis of each cylindrical compartment. In order to avoid singularities such as $\phi \to \infty$ for $\vec{r} \to \vec{r}_{\mathrm{m},jn}$, the minimum possible distance $|\vec{r}-\vec{r}_{\mathrm{m},jn}|$ is set to be the cylindrical compartment radius:

$$|\vec{r}-\vec{r}_{\mathrm{m},jn}| = \begin{cases} a_{jn} & \text{if } |\vec{r}-\vec{r}_{\mathrm{m},jn}| \leq a_{jn} \\ |\vec{r}-\vec{r}_{\mathrm{m},jn}| & \text{else} \end{cases} \tag{2.42}$$

where a_{jn} is the radius of compartment n in neuron j. The application of the line-source approximation for extracellular potential modeling of multicompartmental neurons is further detailed in Hagen et al. [42], where the numerical implementation of equation 2.41 is included.

A combination of the extracellular field approximations presented is used for the current study. The point-source approximation from equation 2.39 is used for the somatic compartment, while the line-source approximation from equation 2.41 is applied to the cylindrical dendritic branches of the neuron. This is referred to as the `soma_as_point` method in Hagen et al. [42].

Chapter 3

Methods

3.1 Network Configuration

There are many ways of combining the theory presented into a neuron network model which can produce results which are reasonably realistic, and the upcoming chapter will introduce the configuration of a recipe network which serves as a baseline. Keep in mind that the following network configuration described is directly relevant to the initial results presented after the methods chapter. It is worth noting that the recipe network chosen is set to be more phenomenological rather than biophysically accurate. An implementation of more biophysically accurate neurons is performed later on.

3.1.1 Network Description

The initial network characteristics are based on an example network of ball-and-stick (BaS) neurons from the LFP simulation package used, the LFPy library by Hagen et al. [42]. The inital `example_network.py` configuration which the study is based on can be found at the initial state of the repository fork[1][43].

The LFPy library builds upon the NEURON python library by Hines et al. [44], and the LFPy library can be used to calculate the extracellular potential signal from transmembrane currents in NEURON, among other things. Several papers have been published on the use of LFPy for LFP simulation purposes [45, 46, 47], and a number of example networks are included in the library for reference. For more information on the functionality of the library, see to the docs written on the module at LFPy.readthedocs.io[42].

The initial recipe network sets the scene for how the rest of the simulations are configured. Table 3.1 lists a number of general network and simulation variables as well as their assigned values. Note the discrete fashion in which the time is simulated, where the simulations increments by $dt = 0.0625$ ms until the total time of T_{sim} =2200 ms is reached. This results in $N_t \approx 35200$ time points in the recipe network which describes the length of the recorded signals. The network of 1280 ball-and-stick neurons exists within a cylindrical space, where

[1] `https://github.com/LFPy/LFPy/blob/49f819/examples/example_network/example_network.py`

Variable	Description	Value
N_{E}	Total number of excitatory neurons	1024
N_{I}	Total number of inhibitory neurons	256
$\mathrm{T}_{\mathrm{sim}}$	Total Simulation time	2200 ms
dt	Simulation time step	0.0625 ms
$\mathrm{T}_{\circ C}$	Temperature	6.5 $^{\circ}C$

Table 3.1: A number of variables describing the recipe network.

a depth parameter z and network radius r_{Nw} are given by:

$$r_{\mathrm{Nw}} = 100 \text{ µm} \tag{3.1}$$

$$z \in [-200 \text{ µm}, 1200 \text{ µm}]. \tag{3.2}$$

The z axis is used as the network depth representative, where $z = 1200$ µm is at the top of the network, and $z = -200$ µm is at the bottom.

Electrode Channel Configuration

Channel number	(x, y, z) Coordinate
1	(0, 0, 1000 µm)
2	(0, 0, 900 µm)
3	(0, 0, 800 µm)
4	(0, 0, 700 µm)
5	(0, 0, 600 µm)
6	(0, 0, 500 µm)
7	(0, 0, 400 µm)
8	(0, 0, 300 µm)
9	(0, 0, 200 µm)
10	(0, 0, 100 µm)
11	(0, 0, 0)
12	(0, 0, -100 µm)
13	(0, 0, -200 µm)

Table 3.2: Positioning of the recording electrode channels in the network space. These 13 channels record 13 unique extracellular potential signals, capturing the network activity at various depths.

The electrode channel distribution follows the z-axis and the spatial coordinates of the 13 channels are listed in table 3.2. Other parameters which are necessary for the electrode configuration are the conductivity of the extracellular space, set here to be $\sigma_{\mathrm{e}} = 0.3$ S m^{-1}, and the radius of each electrode contact surface, set here to be $r = 5$ µm.

Somatic Positioning

The somatic center point of each neuron is distributed evenly around the cylindrical space and the electrode channels presented in table 3.2. The positioning

of the somatic center is determined according to a uniform distribution in a disk at z=0, defined by:

$$x^2 + y^2 \leq r_{\mathrm{Nw}}^2, \tag{3.3}$$

where the radius of the network is set to $r_{\mathrm{Nw}} = 100$ µm around the origin point. In addition to the stochastic distribution of the (x, y) coordinates of each somatic center, an additional variation of each somatic depth is introduced. This is done by sampling each somatic depth z_{soma} according to the Gaussian distribution $z_{\mathrm{soma}} \sim \mathcal{N}\big(0, (20\ \mu\mathrm{m})^2\big)$.

Note that the study denotes the Gaussian distribution using the convention $\mathcal{N}(\mu, \sigma^2)$, where μ is the distribution mean value and σ is the sample standard deviation[48]. To denote the probability density function (PDF) $\Pr(x)$ of the Gaussian distribution, the following convention is used:

$$\Pr_{\mathcal{N}(\mu,\sigma^2)}(x) = \frac{1}{\sigma\sqrt{2\pi}} \exp\left(-\frac{1}{2}\left(\frac{x-\mu}{\sigma}\right)^2\right). \tag{3.4}$$

For clarity and as an example, if a variable l is sampled from an input $\mu = 1$ mm and standard deviation of σ =4 mm, then it is denoted as:

$$l \sim \mathcal{N}\big(1\ \mathrm{mm}, (4\ \mathrm{mm})^2\big), \tag{3.5}$$

where '$\sim$' denotes 'has the probability distribution of'.

3.1.2 Neuron and Synapse Properties

Table 3.3 lists the neuron characteristics and synaptic parameters used in the recipe network. The table describes the universal (applies to the entire network) axial resistivity R_{a} and specific membrane capacitance C_{m}, following what was presented in section 2.2.2 and equation 2.4, respectively. Table 3.3 also describes the membrane characteristics and 3D morphologies of the somatic and dendritic sections in detail. All morphologies of the ball-and-stick sections are relative to the somatic center point, meaning that $(0, 0, z)$ indicates a height of z above the somatic placement. The somatic center points of the neurons are placed according to equation 3.3.

Note the difference in somatic parameters which are set depending on the 'active' or 'passive' characteristics of the soma in table 3.3. When the soma has active conductances, the neuron can fire off APs according to the g_{Na} and g_{K} conductance models described in equations 2.8 and 2.9. An introduction to the HH model was described in section 2.2.3, and further information can be found about the HH model and parameter values at Hodgkin et al. [19] and Gillies et al. [49], respectively. Setting the soma to be passive involves assigning the membrane parameters (g_{m}, E_{m}) listed in table 3.3 to the somatic compartment and implementing equation 2.6 to simulate the membrane potential dynamics. Making the distinction between active and passive somatic compartments is important as removing the AP firing ability of the soma is a requirement of the hybrid- and kernel methods described later on.

The fashion in which compartments are initialized in relation to the sections presented in table 3.3 follows work by Hines et al. [44]. The number of compartments for each neuron section is set according to the so-called `d_lambda` rule,

	Recipe Network		
	Variable	Description	Value
Universal	R_a	Cytoplasmic Resistivity	100 Ω cm
	C_m	Specific Membrane Capacitance	1 µF/cm^2
Soma	Active Characteristics		
	Hodkin-Huxley Model parameters [20, 23]		
	Passive Characteristics		
	g_m	Conductance per unit area	0.3 mS/cm^2
	E_m	Resting potential	-54.3 mV
	3D Spatial Information		
	(x_0, y_0, z_0)	Soma Startpoint	(0, 0, -15 µm)
	(x_1, y_1, z_1)	Soma Endpoint	(0, 0, 15 µm)
	(d_0, d_1)	Boundary Diameters	(30 µm, 30 µm)
Dendrite	Membrane characteristics		
	g_m	Conductance per unit area	0.2 mS/cm^2
	E_m	Resting potential	-65 mV
	3D Spatial Information		
	(x_0, y_0, z_0)	Dendrite Startpoint	(0, 0, 15 µm)
	(x_1, y_1, z_1)	Dendrite Endpoint	(0, 0, 1015 µm)
	(d_0, d_1)	Boundary Diameters	(3 µm, 3 µm)
Synapses	Excitatory		
	τ_1	Synaptic-Rise Time	0.2 ms
	τ_2	Synaptic-Decay Time	1.8 ms
	E_{syn}	Reversal Potential	0 mV
	Inhibitory		
	τ_1	Synaptic-Rise Time	0.1 ms
	τ_2	Synaptic-Decay Time	9.0 ms
	E_{syn}	Reversal Potential	-80 mV

Table 3.3: Description of the ball-and-stick neurons used in the recipe network. Active- and passive soma characteristics are listed, where an active soma is capable of firing APs and a passive soma is not. The active- and passive characteristics follow equations 2.14 and 2.6, respectively. The morphologies of the ball-and-stick sections are included, and the 3D coordinates are all relative to the soma center. The population-specific synapse characteristics used in the synaptic models presented in section 2.2.5 are also listed.

using parameters of $f = 100$ Hz and `d_lambda` $= 0.3$. This fashion of compartment initialization follows a procedure which is similar to the one described in equation 2.7, where the decay factor λ determines the compartment lengths to ensure electronically compact compartments.

3.1.3 Sampled Network Variables

A number of network parameters which are sampled stochastically are presented. One such parameter is the delay value $\bar{\delta}$ assigned to each synaptic connection. This synaptic delay value represents the time it takes for an AP to traverse the length of the pre-synaptic axon and reach the terminals. This value is typically not very long due to the speed of AP propogation. Another sampled parameter is the synaptic weights $\bar{g}$, where the conductance-based synapse model presented in equation 2.22 is implemented in the recipe network.

Additional network parameters include the network connectivity probabilities between populations and the so-called multapse number for each connection. The network connectivity probabilities are defined for all pre- and post- synaptic neuron population combinations C_{XY}, denoting the probability connection from population X to population Y. Once a connection is made, the number of synapses in that connection is determined by the multapse number. The multapse number is sampled stochastically while the connectivity probabilities are kept constant.

As an example of how these parameters are used to configure networks, consider a population of 80 neurons in population E and 20 neurons in population I. A C_{IE} =10% probability of connection from population I to population E then indicates that each neuron in the I population is connected to 8 neurons from the E population on average. If the multapse argument $\bar{n}$ for the I:E synapse type (the notation $i{:}j$ indicates the synaptic type connecting pre-synaptic population i to post-synaptic population j) is set to $\bar{n} = 5$, then there are 5 synapses connecting the I cells to the E cells for each connection. For clarity, this would on average result in $8 \cdot 20 = 160$ I:E connections, and a total of $160 \cdot 5 = 800$ I:E synapses.

Table 3.4 lists the parameters mentioned, along with the connection probabilities C_{XY}. The parameters which are sampled according to a Gaussian distribution have their mean- and standard deviation values (μ, σ) listed in the table. The 12.8 scaling factors which are applied to the max synaptic conductances are described shortly. A number of boundaries of the sampled parameters are also included in the bottom of table 3.4 which describe the type of value assigned ($\mathbb{Z}$ denoting integer numbers and $\mathbb{R}$ denoting real numbers) and domains in which the sampled values are considered valid. If a sampled value is outside the defined domain, the value is discarded and is replaced by a new sample. Table 3.4 lists that the conductances are strictly positive, delay times are above a certain value, and that there is always at least one synapse per connection. Note that table 3.4 sets the standard deviation used for sampling the max synaptic conductance value to 1/10th of the mean value. The max conductance values $\bar{g}_{\text{syn}}$ are changed a number of times in the study, and it is important to note that the standard deviation also changes in a relative fashion.

				Post-Synaptic Type	
		Variable	Description	E	I
Pre-synaptic type	E	$\bar{g}_{E,\mu}$	Max synaptic conductance mean	2 nS/12.8	2 nS/12.8
		$\bar{g}_{E,\sigma}$	Max synaptic conductance std	$0.1 \cdot \bar{g}_{E,\mu}$	$0.1 \cdot \bar{g}_{E,\mu}$
		$\bar{\delta}_{E,\mu}$	Synaptic delay mean	1.5 ms	1.5 ms
		$\bar{\delta}_{E,\sigma}$	Synaptic delay std	0.3 ms	0.3 ms
		$\bar{n}_{E,\mu}$	Multapse mean	2	2
		$\bar{n}_{E,\sigma}$	Multapse std	0.5	0.5
		C_{EX}	Connectivity Probability	10%	10%
	I	$\bar{g}_{I,\mu}$	Max synaptic conductance mean	20 nS/12.8	20 nS/12.8
		$\bar{g}_{I,\sigma}$	Max synaptic conductance std	$0.1 \cdot \bar{g}_{I,\mu}$	$0.1 \cdot \bar{g}_{I,\mu}$
		$\bar{\delta}_{I,\mu}$	Synaptic delay mean	1.5 ms	1.5 ms
		$\bar{\delta}_{I,\sigma}$	Synaptic delay std	0.3 ms	0.3 ms
		$\bar{n}_{I,\mu}$	Multapse mean	5	5
		$\bar{n}_{I,\sigma}$	Multapse std	1	1
		C_{IX}	Connection probability	10%	10%
Boundaries		$\bar{g}$	$\{\bar{g} \in \mathbb{R} \mid \bar{g} \geq 0\}$		
		$\bar{\delta}$	$\{\bar{\delta} \in \mathbb{R} \mid \bar{\delta} \geq 0.3 \text{ ms}\}$		
		$\bar{n}$	$\{\bar{n} \in \mathbb{Z} \mid \bar{n} \geq 1\}$		

Table 3.4: A listing of variables which are sampled from Gaussian distributions $\mathcal{N}(\mu, \sigma^2)$, and the predetermined connection probabilities C. μ is the mean of the distribution and σ is the standard deviation, often denoted 'std'. The max-synaptic conductance values used correspond to a conductance-based synapse model, as described in equation 2.22. The parameter boundaries are also declared, defining which sample values are within, and outside the defined range. If a sample value is outside, a new value is sampled. The multapse value $\bar{n}$ is rounded down to the closest integer after sampling, and must be at least one. The connection probability between the pre- and post-synaptic populations are also included.

3.1.4 Network Scaling and Setup

The scaling factor 12.8 from the synaptic weights in table 3.4 is a result of scaling up the network. The original network was configured from a network of 100 neurons, scaled up to 1280 neurons to obtain a more densely populated network. In order to increase the size of the network, however, one cannot increase the number of neurons in the network without normalizing other network parameters such as the connection probability or synaptic strength. Scaling the network up without normalizing the connectivity between neurons can produce

network behaviour which is far too active, and even epileptic[2]. To state this formally, Potjans et al. [50] perform a first order Taylor series expansion of an expression for the connection probability between two neurons, yielding:

$$C_{N^{\text{pre}},N^{\text{post}}} = \frac{K}{N^{\text{pre}}N^{\text{post}}}, \tag{3.6}$$

where $C_{N^{\text{pre}},N^{\text{post}}}$ is the connection probability of two neurons from populations of sizes N^{pre} and N^{post}. These neurons are randomly connected with uniform probability by K synapses. Following Potjans et al. [50], this expression is obtained using the approximation:

$$K^2 \cdot \left(\frac{-1}{N^{\text{pre}}N^{\text{post}}}\right)^2 \approx 0. \tag{3.7}$$

When scaling up a network, one could consider the number of synaptic connections between two neurons K as a constant, such that the stimulus to each neuron does not change. This equation then states that an increase in the two network sizes $N^{\text{pre}}, N^{\text{post}}$ implies that the connection probability $C_{N^{\text{pre}},N^{\text{post}}}$ should decrease accordingly, if the number of stimulus to each neuron K is held constant.

Instead of reducing the connectivity between neurons, an approach which decreases the strength of synaptic connections is chosen in order to regulate the activity of the scaled up network. This approach comes from a paper by van Albada et al. [51], in which the total network size N and the number of synapses per neuron K are proportional to one another $N \propto K$, and the synaptic weights G are set to scale in the following fashion[51]:

$$G \propto \frac{1}{K} \propto \frac{1}{N}. \tag{3.8}$$

In this context, an increase in network size $N \to 10N$ implies that the synaptic weights G should be adjusted in accordingly $G \to G/10$ in order to keep the so-called asynchronous irregular (AI) network behaviour. AI network behavior means that the network activity is noisy, and there is little structure in the neuron AP firing times. This network firing behavior is desirable as AI firing patterns are observed in cortex[52]. The recipe network which is utilized for the study has an initial size of 100 neurons and is scaled to 1280. The scaling factor of 12.8 applied to the total number of neurons N must then also be applied to the synaptic strengths utilized $G \to G/12.8$ to maintain the AI activity of the recipe network.

3.1.5 Synaptic Positioning

The synaptic positioning of the recipe network configuration is done such that excitatory synapses are primarily connected to the dendritic section of the post-synaptic neuron, while the inhibitory synapses are primarily connected to the somatic section. This commonly observed in cortex [53]. Since the morphologies of both ball-and-stick neuron populations are equivalent in the recipe network,

[2]Epileptic activity of neuron networks is characterized by a large systematic firing of all neurons in full synchronicity, a system in which there is little difference between a single neuron and the rest of the network.

then the only variability is the pre-synaptic connection type. This means that the E:E and E:I synapses are placed in the same fashion, and the same goes for the I:E and I:I synapses. When connecting a synapse, the synaptic placement on the post-synaptic cell is determined by a probability which is assigned to each compartment. This synaptic positioning probability is calculated in part according to sampling the synaptic depth z_{syn} for each synapse. This establishes a depth dependency of the synaptic connection probability, and the two pre-synaptic population types have the following depth preferences:

$$z_{\text{syn, E}} \sim \mathcal{N}\big(500\ \mu\text{m}, (100\ \mu\text{m})^2\big), \tag{3.9}$$

$$z_{\text{syn, I}} \sim \mathcal{N}\big(0, (100\ \mu\text{m})^2\big). \tag{3.10}$$

This indicates that the excitatory synapses prefer a depth of around 500 µm, and the inhibitory synapses prefer a depth of around 0 µm. All synaptic depth preference distributions are set to have a 100 µm standard deviation in the thesis. For example, equation 3.9 reflects that if a post-synaptic compartment is at a depth of $z = 500$ µm and a new excitatory synapse is connected to the neuron, then the compartments at $z = 500$ µm have the largest probability of connection. The depth-related probability of connection assigned to the compartment is given by the PDF value $\Pr^{z}_{\mathcal{N}(500\ \mu\text{m},(100\ \mu\text{m})^2)}(z = 500\ \mu\text{m})$, presented in equation 3.4.

The post-synaptic compartment surface area is also taken into consideration in the synaptic connection probability per compartment. The compartments which take up the largest fraction of total neuron surface area are made to have a higher number of synaptic connections than the smaller ones. This is included by introducing the following surface area dependency to the synaptic connection probability of each compartment:

$$\Pr^{A}_{jn} = \frac{S_{jn}}{\sum_n S_{jn}}, \tag{3.11}$$

where $\Pr^{A}_{jn}$ denotes the area-probability of synaptic connection for compartment n in cell j. This is simply equal to the surface area S_{jn} of compartment n of cell j, divided by the total surface area of all compartments of cell j, given by $\sum_n S_{jn}$. Combining the depth-preference and area-probability yields a probabilistic model in which each compartment is assigned a value between 0 and 1 which dictates how likely a synaptic connection is. The probability of each compartment is given by[42]:

$$\Pr^{\text{syn, }p}_{jn} = \Pr^{A}_{jn} \cdot \Pr^{z}_{\mathcal{N}(\mu_p,\sigma_p^2)}(z_{jn}) \tag{3.12}$$

$$\sum_n \Pr^{\text{syn, }p}_{jn} = 1 \tag{3.13}$$

where $\Pr^{\text{syn},p}_{jn} \in [0, 1]$ is the probability of a synaptic connection from pre-synaptic population p to compartment n of cell j. $\Pr^{z}_{\mathcal{N}(\mu_p,\sigma_p^2)}(z_{jn})$ denotes the PDF value of the distribution $\mathcal{N}(\mu_p, \sigma_p^2)$ which follows equation 3.9 or 3.10, and z_{jn} is the depth of compartment n in cell j. The final probability $\Pr^{\text{syn, }p}_{jn}$ is then normalized for the compartments of the cell, as stated by equation 3.13. Each time a connection is made from a pre-synaptic population p to post-synaptic

neuron j, this probability density distribution $\mathrm{Pr}_{jn}^{\mathrm{syn},\,p}$ for each compartment n is calculated, normalized, and sampled from. The sampled probability is then used to determine which compartment the synapse connects to [42]. This expression ensures that the surface area distribution is fair across compartments in the neuron, as well as maintaining the depth preferences of the synaptic types observed in cortex[53].

3.1.6 External Stimulus

The 'external stimulus' element (sometimes referred to as external drive) is one which has previously been introduced as a depolarization requirement of the network in section 2.2.4. The fashion in which the study at hand addresses this is by connecting $\mathrm{n_{idx}}$ excitatory synapses to each neuron. By default, the number of excitatory external synapses per neuron is set to $\mathrm{n_{idx}} = 64$. The firing rates of these synapses are picked out using a Poissonian distribution, emulating the firing irregularities which were discussed in section 2.2. The expected rate of spike occurrence is set to be $\lambda = 100$, with $k = 0$ expected values following equation 2.18.

Variable	Description	Value
	Synaptic properties	
τ_1	Synaptic Rise time	0.2 ms
τ_2	Synaptic Decay time	1.8 ms
E_{syn}	Synaptic reversal potential	0
$\bar{g}_{\mathrm{syn}}$	Max synaptic conductance	2 nS
	Firing distribution $f_{\mathrm{Ps}}(k;\lambda)$ variables	
λ	Expected rate of occurrance	100
k	Expected values	0

Table 3.5: Configuration for the external stimulating synapses. $\mathrm{n_{idx}} = 64$ such synapses are stochastically connected to each neuron in the recipe network to produce network activity.

All $\mathrm{n_{idx}}$ synapses have the synaptic parameter configuration which is listed in table 3.5, though the firing times sampled from $f_{\mathrm{Ps}}(k;\lambda)$ differ. $\mathrm{n_{idx}} = 64$ of these synapses are connected to each neuron by sampling 64 compartments by area-probability and connecting them. Note that only the area-probability of each compartment Pr_{jn}^{A} from equation 3.11 is used to determine the probability of synaptic connection for the $\mathrm{n_{idx}}$ externally stimulating synapses. No depth-preference is introduced for these synapses.

3.2 Hybrid Model and Kernel Method

The hybrid- and kernel models are the two focal points of the study, and a thorough description of these two methodologies is presented. These both approximate a ground truth signal, often referred to as the 'Reference' signal in the thesis.

3.2.1 Hybrid Model Introduction

The hybrid model is a relatively new development, being first introduced by Hagen et al. [3]. This paper used efficient, simplified neuron models to estimate the LFP signal of more biophysically accurate network models. First, a primary point-neuron network was established and simulated to extract the network AP spiking activity. Then a secondary biophysically accurate network used the spike times of the simplified primary network to determine synaptic activation times, allowing for measurement of the LFP signal[3]. The central assumption of the hyrbid methodology is that the spiking activity of the simplified primary network can be utilized to predict the LFP activity of the biophysically detailed secondary network. This assumption of a linear spike-to-LFP relationship is a central point of testing in the initial study, and a description of how this can be tested is described.

The testing of the hybrid method in the thesis differs from the original hybrid motivation. The original motivation was to conduct an efficient simplified primary network simulation and apply it to a biophysically detailed secondary network. The current study differs in that the primary- and secondary networks are mostly equivalent. They still serve the same purpose, where the spiking times of the primary network are applied to the synaptic activation times of the secondary network. Both these networks produce LFP signals, and the secondary network hybrid approximation is benchmarked by the ground-truth primary network signal. Note that the primary network is often referred to have 'active conductances' and be 'fully connected' in the study. These refer to having somatic compartments which are capable of AP firing, and have direct connections between pre-synaptic and post-synaptic neurons, respectively. The secondary network is not technically conneceted, as synapses provide current injections to the post-synaptic neuron depending on predetermined activation times, replicating the synaptic activity of the primary network. Note also that the secondary network neurons have inactive conductances, meaning that no additional AP firing can occur. This allows for a replay of the synaptic activity of the primary network without additional AP firing activity in the soma.

3.2.2 Kernel Method Description

The kernel method takes the linear spike-LFP concept a step further, and is a highly computationally efficient LFP approximation method. The kernel method requires two preliminary pieces of information to provide a LFP approximation. The primary network spiking activity per population is required, and the net LFP response of a single spike per neuron per population from the primary network is required. The way this is obtained is to set up synaptic connections identical to the primary network, synchronously activating the synapses and recording the LFP response in each of the electrode channels. Assuming a

linear spike-LFP relationship, the kernel method then uses the spike times and the LFP response per spike signals to approximate the full LFP signal.

Kernel Method Procedure

The rest of the section lays out the various details which go into configuring the kernel method. Firstly, a primary network is simulated, where the ground-truth LFP, spiking times, neuron configurations, and synaptic placements are all saved. A network which has a neuron configuration and synaptic placements equivalent to the ground-truth network is then set up. The somatic compartments are be set to have passive conductances, such that no additional AP firings occur, and all synapses are activated at a synchronous time τ_s, where the delay time of AP propogation to current injection $\bar{\delta}$ described in section 3.1.3 is included. The LFP response of the synaptic activations is then registered for all recording electrode channels, and these signals are referred to as the kernels H^c. Note that this is done separately for every population in the network, such that kernels are obtained for the excitatory- and inhibitory synapses separately. Once the spiking of the primary network and kernels H^c are obtained, the kernel method can be applied.

3.2.3 Convolution

The way in which the kernel method approximates the LFP signal is by convolution of the firing rates and the kernels H^c. Convolution is a mathematical operation in which two temporal signals $x(t)$ and $h(t)$ are combined into a new temporal signal $y(t) = (x * h)(t)$ in the following manner[54]:

$$x(t) * h(t) = \underbrace{\int_{-\infty}^{\infty} x(\tau)\ h(t-\tau)\ d\tau}_{\mathrm{y(t)}}\,. \tag{3.14}$$

x is considered as the input signal and y is the output. The filter h (often referred to as the kernel) transforms the input signal by integrating over a separate time value τ for each time signal t, and multiplying the two signals together[54]. Applying this function to temporally discrete signals $t \to t_i$, as is done in the thesis, involves implementing the following equation numerically[54, 55]:

$$(x * h)(t_i) = \sum_{j=-\infty}^{\infty} x(t_i - t_j)\ h(t_j) \tag{3.15}$$

where the index $i \in [0, N_t]$ is the temporal index, and N_t is the total points of time of the simulation. Figure 3.1 illustrates a convolution example, where each point in signal $y(t_i)$ is the result of a summation of scanning the filter $h(t_j),\ j \in [\ldots, i-1, i, i+1, \ldots]$, over the input signal $x(t_i)$. Note that the kernel contribution to the output signal is only non-zero in the points $h(-5$ ms$\leq t_i \leq 5$ ms). This means that the secondary time constant τ must only be summed from $\tau \in [-5\text{ ms}, 5\text{ ms}]$ for a triangular filter such as the one in figure 3.1. Factors like these are important to decrease computational requirements of these methods. As we can see in the figure, there is a notable noise reduction from the input signal x to the output y. This is characteristic of the convolution

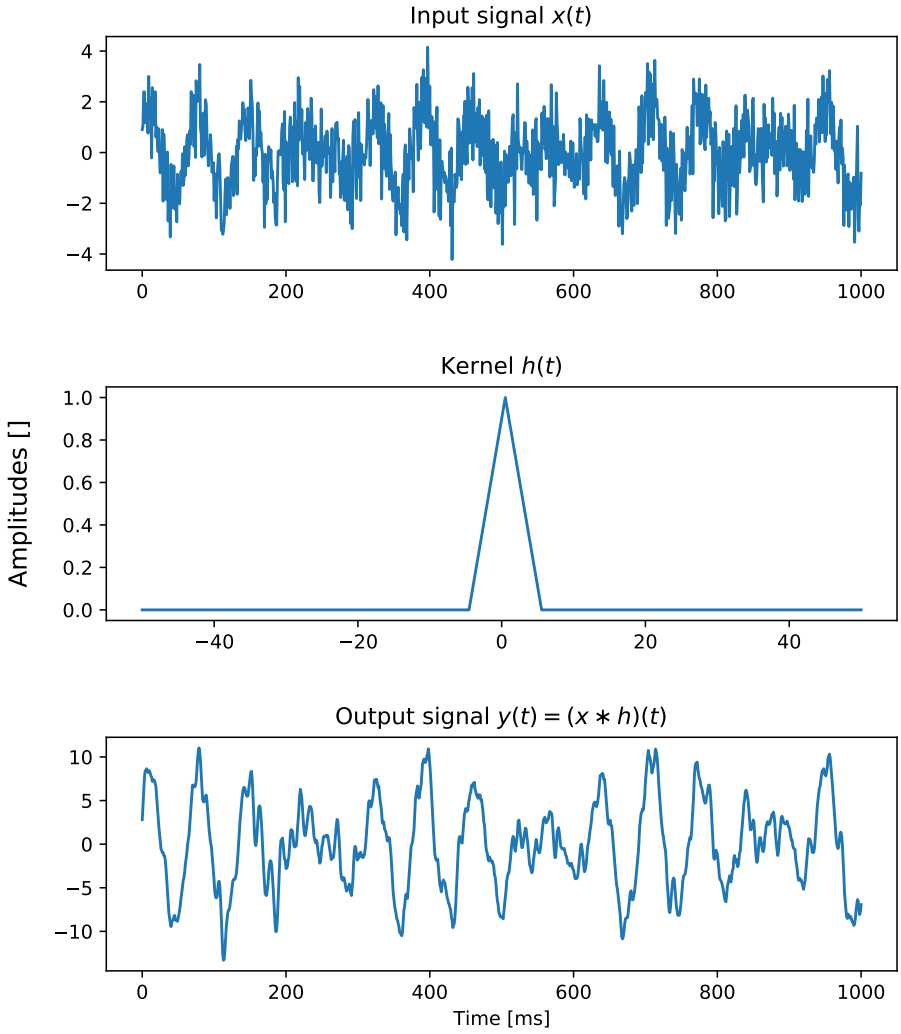

Figure 3.1: Convolution between an input signal and a triangular kernel. The amplitude difference of signals x and y illustrate how multiple contributions from the kernel h are be summed into the same output $y(t_i)$. The number of such contributions depends on the width of the kernel, and this results in a low-pass filtering effect. Image generated using the `misc/convolution_intro.py` script [39].

operation, where a temporarily extended filter such as the triangular filter allows for multiple neighboring points of the input signal to add up to a weighted sum for each output $y(t_i)$, as described in equation 3.15. The more broad the filter is, the more contributions from neighboring points each output point $y(t_i)$ has, generally yielding an output signal which has lower frequency content than the input signal (depending on the filter h).

3.2.4 Kernel Method LFP Approximation

To reiterate, the kernel method obtains the LFP approximation by convolving the spiking activity of the primary network with the LFP response of a synchronous synaptic activation H_p^e per neuron per population in a similar secondary network. The spiking activity of the primary network is stored in spike δ-train signals for each population ν_p. This signal is similar to a histogram with N_t bins, where the value in each time window $[t_{i-1}, t_i]$ equals the number of AP firings which occurred within the bin width dt. These spike δ-train signals can only equal a non-negative integer for any time signature $\nu(t_i) \in \mathbb{Z}^{\geq 0}$. Figure 3.2 illustrates the convolution of a spike δ-train input signal x and a kernel h, and depicts how the primary network spike δ-train ν is combined with the

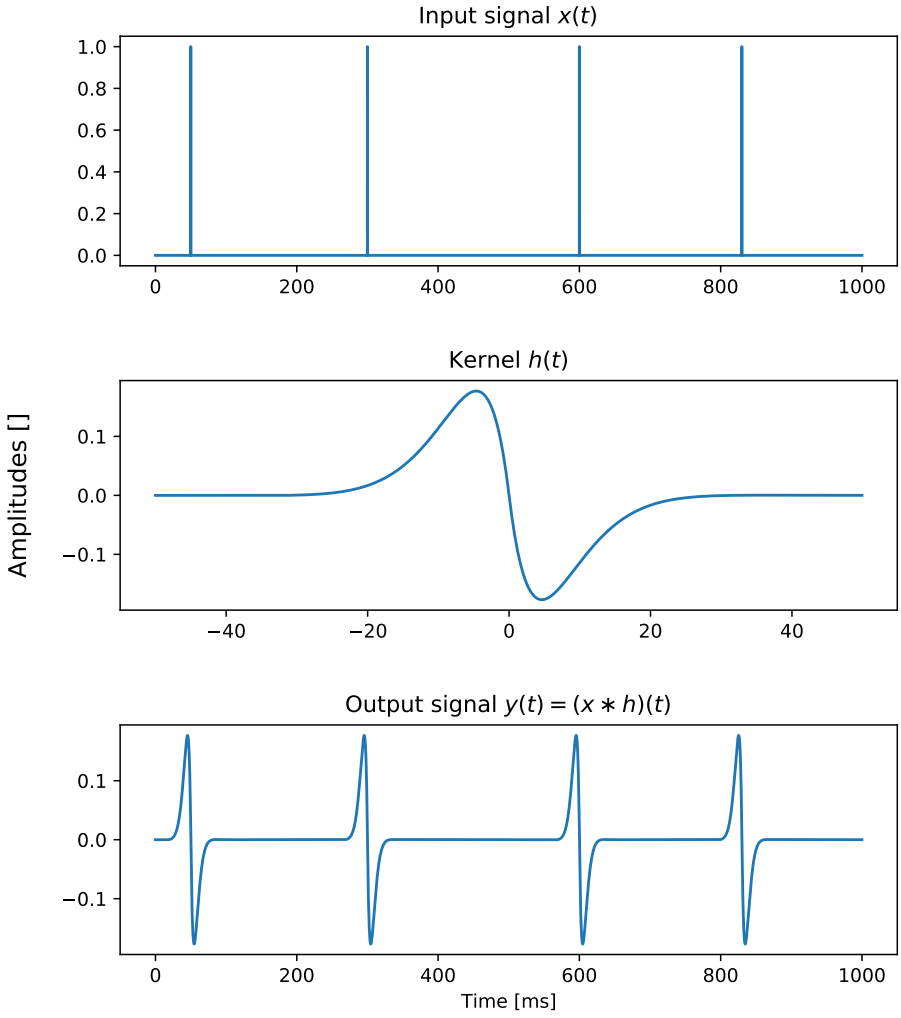

Figure 3.2: Illustration of a convolution between a δ-train signal and a kernel h. Each non-zero x value inserts the kernel h into the output signal y. Image generated using the `misc/convolution_example.py` script [39].

LFP response per spike H_p^c to produce the LFP approximation. The population spiking activity ν_p is obtained from the neuron-specific spiking times by:

$$\nu_p(t_i) = \sum_{j=1}^{N_p} \nu_j(t_i) \tag{3.16}$$

for all times t_i, where ν_j is the spike δ-train for neuron j in population p with size N_p. The extracellular potential kernel approximation ϕ^c in channel c is then obtained by combining population-specific kernels H_p^c with population-specific firing rates ν_p by:

$$\phi_p^c = (\nu_p * H_p^c), \tag{3.17}$$

$$\Rightarrow \phi^c = \sum_p (\nu_p * H_p^c), \tag{3.18}$$

where ϕ^c is the kernel approximation to the extracellular potential in channel c. Note that the extracellular potential and LFP responses have been used somewhat interchangably for the kernels H_p^c in the section. Framing the kernels H_p^c to be the LFP response builds intuition on the kernel method, though the $\leq$ 300 Hz low-pass filter could be applied to the extracellular responses either before- or after convolution. Both produce the same output, as convolution is a linear operation The thesis applies the low-pass filter $\leq$ 300 Hz after convolution, such that the kernels H_p^c illustrated later on are the full extracellular potential responses of the synchronous AP firing.

3.3 Evaluation Methods and Signal Processing

A central component of the thesis is the evaluation and signal processing of the recorded results. A number of metrics are presented which are used to evaluate the performances of the approximation methods in relation to the primary ground-truth signal. Other signal processing tools applied to the signals are also presented shortly after, such as the low-pass filter ≤ 300 Hz used to obtain the LFP signal from the raw extracellular potential.

3.3.1 Evaluation Methods

The current study aims to compare two time series of data to each other. One signal which is a ground-truth, and another which is an approximation. This study utilizes the relative maximum error (RME), pearson correlation coefficient (PCC) and the mean squared error (MSE) for signal comparison between the two.

Relative Maximum Error

In order to evaluate the performance of an extracellular potential recreation for any given time t_i, the relative maximum error (RME) metric is used. The RME outputs a signal of length N_t for two input signals of length N_t, where the signals are depicted as vectors with length equal to the number of time steps in the simulation:

$$\vec{x}_1 = [x_1(t_1), x_1(t_2), \ldots, x_1(t_{N_t-1}), x_1(t_{N_\mathrm{t}})] \tag{3.19}$$

$$\vec{x}_2 = [x_2(t_1), x_2(t_2), \ldots, x_2(t_{N_t-1}), x_2(t_{N_\mathrm{t}})] \tag{3.20}$$

$$\vec{x}_1, \vec{x}_2 \in \mathbb{R}^{N_\mathrm{t}}. \tag{3.21}$$

The RME calculates the element-wise subtraction of the two, normalizing to the maximum of the second signal:

$$\mathrm{RME}(\vec{x}_1, \vec{x}_2) = \left[\frac{x_1(t_1) - x_2(t_1)}{\max(\vec{x}_2)}, \ \ldots, \ \frac{x_1(t_{N_\mathrm{t}}) - x_2(t_{N_\mathrm{t}})}{\max(\vec{x}_2)} \right], \tag{3.22}$$

where $\mathrm{RME}(\vec{x}_1, \vec{x}_2) \in \mathbb{R}^{N_\mathrm{t}}$ and $\max(\vec{x}_2)$ equals the maximum scalar value of the $\vec{x}_2$ vector. This is a useful metric for finding relative error between two signals while simultaneously avoiding division by close-to-zero values.

Mean Squared Error

The mean squared error (MSE) metric is used as a measure of absolute signal difference. The MSE yields a scalar value $\mathrm{MSE}(\vec{x}_1, \vec{x}_2) \in \mathbb{R}^{\geq 0}$, obtained by subtracting the two signals from each other at time t_i, squaring the result, and calculating the mean for all times t_i:

$$\mathrm{MSE}(\vec{x}_1, \vec{x}_2) = \frac{1}{N_\mathrm{t}} \sum_{i=1}^{N_\mathrm{t}} \big(x_1(t_i) - x_2(t_i)\big)^2 \tag{3.23}$$

Note that this metric has units which correspond to $[x]^2$, where $[x]$ is the input unit. This metric is one of two ways of evaluating two signals $\vec{x}_1, \vec{x}_2$ by a scalar value.

Pearson Correlation Coefficient

The other technique used to compare two signals is the pearson correlation coefficient (PCC). This coefficient is calculated using two signals $\vec{x}_1, \vec{x}_2 \in \mathbb{R}^{N_t}$, and the PCC produces a scalar value which evaluates the linearity between the two:

$$\text{PCC}(\vec{x}_1, \vec{x}_2) \in [-1, 1] \subset \mathbb{R}. \tag{3.24}$$

This value approaches 1 as the two signals $\vec{x}_1$, $\vec{x}_2$ approach colinearity - a property in which one can be expressed in terms of the other multiplied by some constant $\vec{x}_1 \propto \vec{x}_2 \Rightarrow \text{PCC}(\vec{x}_1, \vec{x}_2) = 1$. This means that two signal which have the same variance, or shape, but different amplitudes, would still have a high correlation coefficient. Two signals which are completely uncorrelated will produce PCC=0, and two signals which are precisely anti-correlated yield PCC=-1[56]. The PCC value is calculated using the following expression [57]:

$$\text{PCC}(\vec{x}_1, \vec{x}_2) = \frac{\text{cov}(\vec{x}_1, \vec{x}_2)}{\text{std}(\vec{x}_1)\text{std}(\vec{x}_2)}, \tag{3.25}$$

where $\text{cov}(\vec{x}_1, \vec{x}_2)$ is the covariance of the two signals, given by [58]:

$$\text{cov}(\vec{x}_1, \vec{x}_2) = \frac{1}{N_t} \sum_{i=1}^{N_t} \left[\vec{x}_1(t_i) - \bar{x}_1\right] \left[\vec{x}_2(t_i) - \bar{x}_2\right], \tag{3.26}$$

where $\bar{x}$ is denotes the mean, and $\text{std}(\vec{x})$ is the sample standard deviation.

3.3.2 Frequency Spectrum Analysis

Fourier Transformations

A more in-depth approach to signal processing and signal analysis is found in the frequency domain. The Fourier Transformation (FT) is a commonly used analysis and processing technique of temporal signals. Applying a FT to a signal yields information about which frequencies the input is comprised of, and the FT method involves implementing the following transformation [59, 60]:

$$\hat{s}(f) = \mathcal{F}\big(s(t)\big) \tag{3.27}$$

$$= \int_{-\infty}^{\infty} s(t) e^{-2\pi i t f} dt \tag{3.28}$$

Here, $s(t)$ denotes the temporal input signal to be transformed, $\hat{s}(f)$ represents the FT of $s(t)$, and f represents the frequency in units of Hz. Applying this transformation to a sum of sinusoid signals returns an image of what the frequency spectrum illustrates. The sum of two sinusoid signals of frequencies 100 Hz and 250 Hz and a small amount of noise have their FT signal $\hat{s}$ illustrated in figure 3.3. The FT can then be used to calculate the power spectral density for signal analysis.

Power Spectral Density

The following expression is used to calculate the power spectral density (PSD) for a given input signal $s(t)$[61]:

$$S_{xx} = \lim_{T \to \infty} \frac{1}{T} \left|\hat{s}_T(f)\right|^2, \tag{3.29}$$

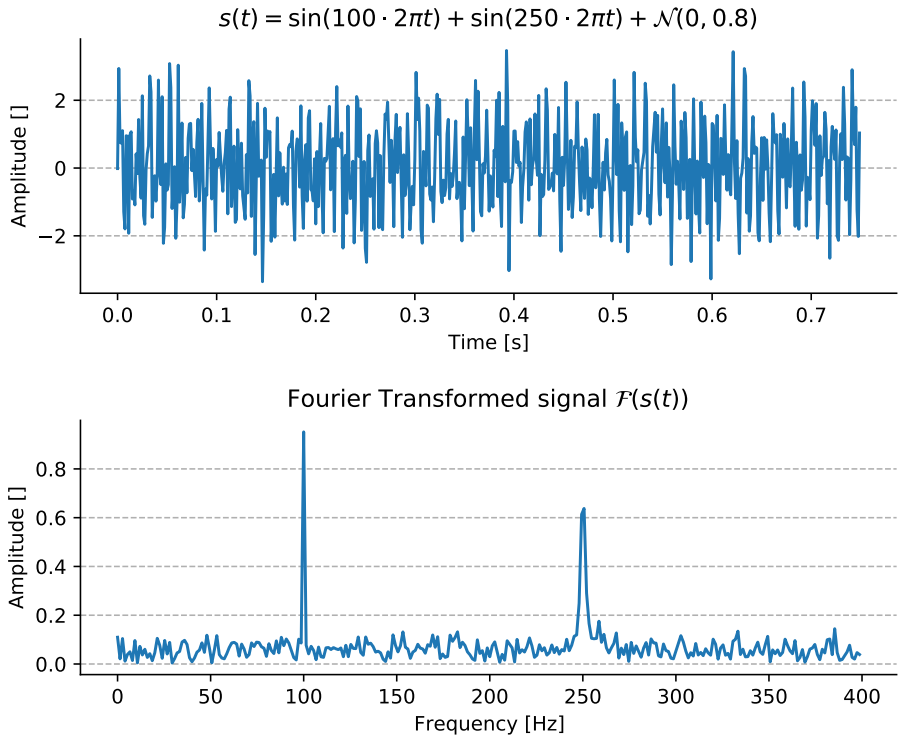

Figure 3.3: Illustration of the frequency domain $\mathcal{F}\big(s(t)\big)$ of an input signal $s(t)$ which is comprised of two periodic sinusoids with frequencies 100 Hz and 250 Hz. Additional noise is added to the signal which has a Gaussian distribution $\mathcal{N}\big(0, (0.8)^2\big)$. Image generated using the `misc/fourier_example.py` script [39].

where $\hat{s}_T(f)$ is the FT of the signal $s(t)$ within some given time period centralized around an arbitrary time $[t - T/2, t + T/2]$. This method splits the signal up into equal windows of length T and subsequently applies the FT method to each window. This procedure is usually referred to as the Welch method[62, 63]. After this is done, the FT of each window is squared and the average is calculated. Finally, divide the squared average by the analysis bandwidth to obtain the PSD output. This is done to normalize the data to a single Hertz[62]. The enterpretation of this output PSD signal is that it shows the average energy at a single frequency over a period of time T[62]. A central advantage of the PSD method in relation to the FT is that the units which the PSD signal yields are more intelligible than those of the FT, making for a better signal for analysis. For more on the PSD methodology for analysis, see to the explanation by [62].

3.3.3 Signal Post-Processing

Low-pass Filtering

In order to extract the LFP signal from the extracellular potential, a low-pass filter needs to be applied. As has been mentioned, the cutoff frequency for the LFP signal is set to ≤ 300 Hz in the thesis. The main filtering technique used

comes from the Butterworth filter, developed by Butterworth et al. [64] in an attempt to have as flat a frequency response in the pass-band as possible[64]. The critical frequency (approximately the -3 dB frequency) used to obtain the LFP signal is $f_c = 300$ Hz, and the thesis uses 4th order Butterworth filtering throughout. The Butter filter is a well-established filtering technique within physiological signals, in particular due to the fact that there is minimal attenuation of the signals you want to keep. A formal mathematical definition of the Butter filter is considered out of scope in the current thesis.

DC Subtraction

An important signal post-processing step which performed in the study is one which subtracts the DC component from the extracellular signals. The DC component represents the permanent offset of the extracellular signals, and is removed by subtracting the signal mean from all signal time points. As was mentioned previously, the first 200 ms of the simulations can include unwanted initialization artifacts, such that the DC value subtracted from the extracellular potential signal is the mean value calculated by excluding the initial 200 ms:

$$\phi^c(t_i) = \phi^c(t_i) - \mathrm{mn}^c_{t \geq 200 \text{ ms}}, \tag{3.30}$$

$$\mathrm{mn}^c_{t \geq 200 \text{ ms}} = \frac{1}{N_{t \geq 200 \text{ ms}}} \sum_{t=200 \text{ ms}}^{2200 \text{ ms}} \phi^c(t). \tag{3.31}$$

This step is performed for all extracellular signal time points $\phi^c(t_i)$ of each electrode channel c. $N_{t \geq 200 \text{ ms}}$ is the number of time points which are after 200 ms, and $\mathrm{mn}^c_{t \geq 200 \text{ ms}}$ is the mean extracellular potential value of channel c, calculated by excluding the first 200 ms of data. This pre-processing step is important to apply before the signals are presented, and before the evaluation metrics are applied. It is finally worth noting that when presenting the signals later on, only the final ≈ 200 ms of the simulations are illustrated. This is done in order to get a fine-grained image of the signals and their differences, as the difference details are harder to see if the entire time series is shown.

3.4 Methodology Implementation

The implementations of the methodologies are presented, and the following section details the steps involved to implement the recipe network, conductance- and current-based hybrid models and the kernel method.

3.4.1 Recipe Network

All recipe network parameters and configuration states have been presented, though the fashion in which some of the results are presented should be established beforehand. The central illustration of network activity used in the thesis

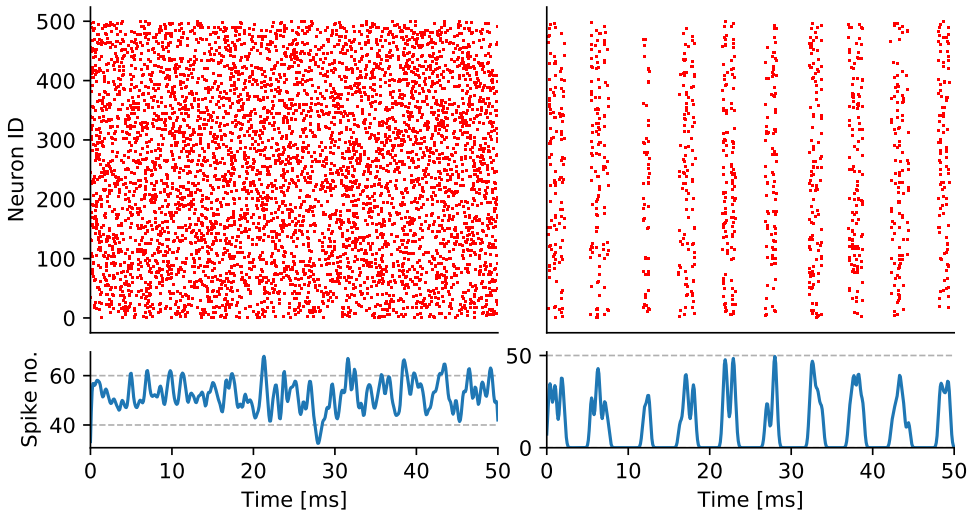

Figure 3.4: Two example spike raster plots of 500 neurons simulated for 50 ms. Left: Asynchronous irregular (AI) spiking of the network. Right: Synchronous firing structure. Below each is the smoothed total number of network spikes per time. Image generated using the `misc/spike_raster_example.py` script[39].

is the spike raster plot. Two example spike raster plots are illustrated in figure 3.4, where each red dot represents an AP firing. The neuron ID and time can be seen on the axes, and the spike raster plot is used to identify large scale network AP firing patterns such as synchronous firing structures. The thesis includes the population-specific firing rates in the spike raster plots, given by:

$$\bar{\nu}_p = \frac{|\nu_p|_{\geq 200\text{ ms}}}{N_p \cdot (\mathrm{T}_{\mathrm{sim}} - 200\text{ ms})}, \tag{3.32}$$

where $|\nu_p|_{\geq 200\text{ ms}}$ is the total number of spikes from population p which occur after the first 200 ms of simulation, N_p is the size of population p, and $\mathrm{T}_{\mathrm{sim}}$ is the total simulation time of 2200 ms. The reason the first 200 ms are left out of this evaluation is due to the so-called transient time. The first 200 ms of the simulation are affected by startup artifacts which are attributed to the fact that all neurons are initialized at the same membrane voltage. This means that it takes time for the system to stabilize, and the first 200 ms of the simulation

results are excluded from the evaluation metrics for this reason. The firing rate per population $\bar{\nu}_p$ indicates how active each population is, and is used throughout the spike raster evaluations later on. Keep in mind that the fully connected, active conductance recipe network is the only one which is presented in terms of spike raster graphs, as the rest of the LFP approximation methods have inactive conductances, meaning that no APs are fired.

3.4.2 Hybrid Model

Two hybrid models are presented - one in which the synaptic connections of the network use the conductance-based synapse model from equation 2.22, and another which utilizes the current-based synapse model from equation 2.27. Keep in mind once again that these synapses are connected to post-synaptic cell compartments with predetermined spiking times which come from the fully connected, active conductance 'primary' network simulation.

Conductance-based Hybrid Model

The initial results follow the procedure described in section 3.2.1, where a secondary network is set up which recreates the synaptic firing of a primary network. The secondary network has inactive conductances in the soma, and there are no connections made between neurons. The synapses are connected to the post-synaptic compartments identically to the primary network, and the synapses have activation times determined by the spiking times of the primary network:

$$t_{\mathrm{a},i} = t_{\mathrm{AP},i} + \bar{\delta}, \tag{3.33}$$

for all synapses and pre-synaptic neuron APs i of the primary network. $t_{\mathrm{a},i}$ is the synaptic activation time, $t_{\mathrm{AP},i}$ is the AP firing time of the pre-synaptic neuron in the primary network, and $\bar{\delta}$ is the synaptic delay of the synapse. When recreating the synapses, one must also deduce whether the synapse has excitatory or inhibitory rise- and decay times τ_1, τ_2 and what the reversal potential E_{syn} is. This is done by checking the pre-synaptic neuron population, and setting the variables according to what was presented in table 3.3. When recreating the synaptic activity in the hybrid scheme, the external stimulating $\mathrm{n_{idx}}$ synapses are also recreated, where the compartment placement, firing times, and synaptic parameters are all predetermined by the primary network configuration. Note that in the results, the low-pass filter ≤ 300 Hz is not applied for the initial hybrid method comparison. The raw extracellular potential signals are instead illustrated to view the high-frequency somatic AP firing activity which is produced by the active-conductance, ground-truth signal of the primary network.

Current-Based Hybrid Model

The current-based hybrid model is presented after the conductance-based hybrid model results. Much of the same methodology is used, and a linearization of the synaptic weights $\bar{g} \rightarrow \bar{I}$ is conducted. Section 2.2.5 described the two synapse models in detail, with a brief description of the differences and the process of converting between the two. In the linear current-based hybrid model, the primary network synapse model is unchanged, sampling synaptic weights

$\bar{g}_{\text{syn}} \sim \mathcal{N}(\bar{g}_{p,\mu}, \bar{g}^2_{p,\sigma})$ as was listed in table 3.4. The current-based hybrid model then converts these conductance-based weights to a maximum current $\bar{g} \to \bar{I}$ in the fashion described in equation 2.28. As aforementioned, this includes modeling the post-synaptic membrane potential V as a constant $V \to \bar{V}$. The estimation $\bar{V}$ is set to be equal to the mean of the mean somatic membrane potential of the active/primary network, as was described in equation 2.29, omitting the first 200 ms of initialization:

$$\bar{V} = \frac{1}{N} \sum_{j=1}^{N} \frac{1}{N_{t \geq 200 \text{ ms}}} \sum_{t=200 \text{ ms}}^{2200 \text{ ms}} V_{\text{soma},j}(t), \tag{3.34}$$

where $V_{\text{soma},j}(t)$ is the somatic potential at time t for neuron j, $N_{t \geq 200 \text{ ms}}$ is the number of time points after 200 ms, and N is the number of neurons in the network. In the thesis, $\bar{V}$ is determined by plotting the mean somatic potential values for each neuron as a histogram in the results. The estimation $\bar{V}$ can then be extracted as the mean value of the histogram distribution. Once $\bar{V}$ is determined, the conversions from the conductance-based synapse model weights to the current-based synapse model weights are given by:

$$\bar{I}_{\text{syn, E}} = \bar{g}_{\text{syn, E}} \cdot \big(\bar{V} - (0 \text{ mV})\big) \tag{3.35}$$

$$\bar{I}_{\text{syn, I}} = \bar{g}_{\text{syn, I}} \cdot \big(\bar{V} - (-80 \text{ mV})\big), \tag{3.36}$$

using the synaptic reversal potential values stated in equation 2.20.

3.4.3 Kernel Method

Following is a blueprint of the methodology used to produce a reference network simulation and a corresponding kernel method approximation:

1. Simulate the primary, fully connected, active conductance network, sampling and saving all required network characteristics.
   (a) Save the neuron and synaptic placements, as well as all necessary synaptic parameters such as the conductance-based weights $\bar{g}_{\text{syn}}$ and delay factors $\bar{\delta}$.
   (b) Save the spiking δ-trains ν_p for each population p independently. These are a requirement for the convolution operation of the kernel method.
   (c) Calculate the mean somatic potential of each neuron and save the data as a histogram displaying the distribution of mean somatic potentials across the network.
2. Establish a secondary configuration in a similar fashion to the previous hybrid scheme initializations (not connected, inactive soma conductances).
3. Simulate the copied configuration once for the synchronous firing of each synapse type, recording the extracellular potential response with identical recording electrodes to the primary network.
   (a) A loop is conducted over all the synapse types [E:E, E:I, I:E, I:I] (the notation $i{:}j$ indicates the synapse type where i is the pre-synaptic

population and j is the post-synaptic population), simulating for 400 ms and firing the appropriate synapses synchronously at $\tau_s = 200$ ms.

(b) Ensure that the conductance-based weights from the recipe network are converted to current-based synapse weights, setting the post-synaptic membrane potential estimation $\bar{V}$ according to the recipe network and equation 3.34.

(c) Ensure that the characteristic synaptic delay $\bar{\delta}$ for each synapse is added on to the synchronous AP firing time according to equation 3.33.

(d) Record the extracellular potential signal for each channel ϕ^c, and extract the kernels using $H_p^c = \phi^c(100 \text{ ms} \leq t_i \leq 300 \text{ ms})$, where p is the pre-synaptic neuron population of the current synapse firing (i when firing the i:j synapse).

(e) Finally, divide this signal by the total number of neurons N_p in the pre-synaptic population p, obtaining the net extracellular potential response H_p^c of an AP in channel c per neuron in population p.

This is important to describe, as there are a number of details which go into the kernel method such as the inclusion of the delay factor of each synapse $\bar{\delta}$ in the kernel H_p^c generation.

An important factor to consider in the methodology is the total simulation time for the generation of kernels for each synaptic type, set here to be 400 ms. In determining this time, one must ensure enough time for both initialization as well as kernel resting/decay time. The exctacellular signals at $\phi^c(t_i = 0)$ need time to initialize, decaying to zero and stabilizing well before the synchronous AP firing of the network. The signal also needs time to decay to zero after the synchronous AP firing $\phi^c(t_i \geq 200 \text{ ms})$ to get the full kernel image. The signals are therefore given $\tau_s = 200 \text{ ms} \pm 100 \text{ ms}$ before and after for pre-τ_s initialization and post-τ_s decay. This important for an accurate kernel shape, and the extracellular potential values at $t_i = 100$ ms and $t_i = 300$ ms should be asserted to be equal to a baseline value. This relaxed extracellular potential value is then subtracted from the entire signal, such that the kernels are normalized to zero at the points in which there is no AP response. The value chosen to subtract from the entire signal for normalization purposes could be anywhere in the range of $t_i \in [100 \text{ ms}, 200 \text{ ms})$, or at the final point of $t_i = 300$ ms. The thesis normalizes the kernel signals by subtracting the signals by $H_p^c(t_i = 100 \text{ ms})$ for all populations p and channels c.

Methodology Remarks

In addition to the resting time normalization, there are a number of other notable remarks which are important to consider moving forward with the kernel method. For one, the extracellular potential contributions from the E:E and E:I synapse types both represent the extracellular potential response from the synchronous AP firing of the E population. This means that these can be added accordingly to represent the full H_E^c kernels $H_E^c = H_{E:E}^c + H_{E:I}^c$. The current study chooses to visualize these separately, as it is interesting to see the differences between the synaptic connection types before convolution. This is equally

true for the I population and the I:E and I:I kernels. It is finally worth noting that the synaptic activations only account for the 'internal' synapses, denoting direct connections between neurons in the primary network. This implies that the kernel method extracellular signal includes neither the high-frequent somatic AP firing activity nor the n_{idx} external stimulation synapses, both of which are prominent in the primary network 'Reference'/ground-truth extracellular potential signal. These are all important factors to consider for the kernel method evaluation later on in the results section.

To summarize, the extracellular potential responses $H_p^c = \phi^c(100 \text{ ms} \leq t_i \leq 300 \text{ ms})$ from the synchronous AP firing of each synaptic type [E:E, E:I, I:E, I:I] are combined with the primary network firing rates ν_p using convolution, such that the extracellular potential approximation of the kernel method are then given by:

$$\phi^c_{\text{KM}} = \nu_{\text{E}} * (H^c_{\text{E:E}} + H^c_{\text{E:I}}) + \nu_{\text{I}} * (H^c_{\text{I:E}} + H^c_{\text{I:I}}) \,, \tag{3.37}$$

for all channels c. Finally, after the kernel method extracellular potential estimation ϕ^c_{KM} is calculated, the LFP approximation is obtained by applying the low-pass filter ≤ 300 Hz presented in section 3.3.3 to ϕ^c_{KM}.

3.5 Limitations of the Linear Models

The linear model limitations is a focal point of the study, where the performances of the linear LFP approximation methods are evaluated in various network conditions. This section is designed to prepare the reader for the new network conditions which are induced, as well as the new condition characteristics and how they can be quantified. This ties closely to the thesis goal of validating the linear spike-LFP assumptions made in Hagen et al. [3]. The main concern of the kernel method originates in nonlinear LFP contributions, and synchronous network states are of particular interest.

3.5.1 Network Synchronicity

If the network is stimulated in a certain fashion, a synchronous phenomena can appear in the spike δ-trains of the neurons. In a perfectly synchronous network state, each and every neuron fires an AP at the same time, repeating synchronously. Figure 3.4 illustrated this phenomena, where there is far less stochasticity in the synchronous network firing patterns (right) than in the asynchronous irregular firing patterns (left). This is also reminiscent of the epileptic phenomena described in section 3.1. In this system where the synchronicity of the network is large, the linear method LFP approximations are expected to have a drop in performance relative to the ground-truth 'Reference' signal. This is in part due to the fashion in which the post-synaptic membrane potential is estimated $V \rightarrow \bar{V}$. If two connected neurons fire an AP at the same exact time, then the post-synaptic membrane potential is likely to be much higher than the average $\bar{V}$ due to the depolarization of the membrane back-propagating into the dendrites. This is expected to impact the performance of the kernel method as an LFP approximation technique, and a comparison of the kernel method LFP approximation and the groun-truth LFP signal under various degrees of network synchronicity is conducted. A new metric S_{PCC} is introduced in order to measure the degree of synchronisity in a network, placing a quantitative measure of synchronicity to include in the results.

Spike Train Similarity

The pearson correlation coefficient (PCC) introduced in equation 3.25 was established as a way to evaluate the similarity between two signals. This metric will continue to be involved in the calculation of network synchronicity, as it can be used to quantify the similarity between neuron spike δ-trains. For full network synchronicity, the spike δ-train similarity of each neuron with each other neuron is evaluated. The average correlation of all spike δ-train similarities then represents the network synchronicity measure. Note that the spike δ-train signals only equal non-zero values in very small $dt = 0.0625$ ms windows where the spikes are registered to occur, as described in section 3.2.4. The similarity between two such signals would then only register if spikes happen within the same small time dt. The spike δ-train signals are transformed into a more temporally smooth signal in an attempt to solve this, giving the PCC measure some more leniency in the synchronicity context. This is done by convoluting the delta signal with a Gaussian kernel of max value 1 and standard deviation σ, producing a temporally spaced spike δ-train signals for the synchronicity measure.

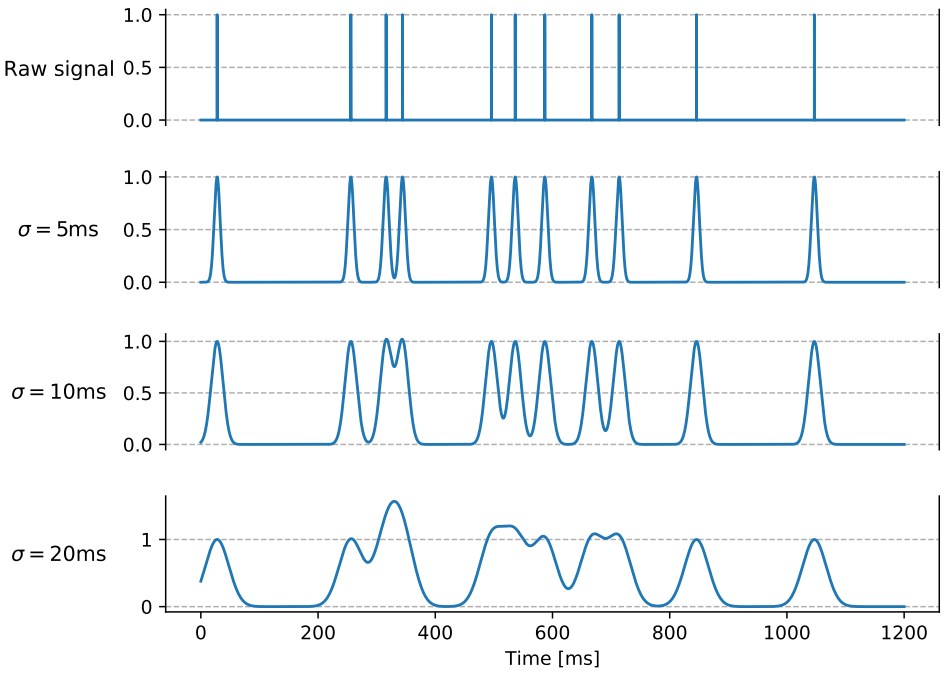

Figure 3.5: Impact of Gaussian kernel convolution on a δ-train signal. Various Gaussian kernel standard deviations σ are included for reference. Image generated using the `misc/delta_convolution_example.py` script[39].

An example convolution of a neuron spike δ-train with various Gaussian kernels is illustrated in figure 3.5. Multiple standard deviations are illustrated to show the impact it has on the convolution. The widths represent the temporal spread which each neuron spike is allowed when evaluating the similarity between two spike δ-trains. The larger the standard deviation, the longer the temporal spread of each spike, and the more likely for two spikes to overlap in the PCC evaluation. If the spread is chosen to be $\sigma = 20$ ms, then two spikes ≈ 20 ms apart would be deemed somewhat synchronous by the PCC measure. The aim is to keep it small enough to be considered temporally synchronous without being too generous. The standard deviation value of the kernel is set to be $\sigma = 5$ ms in the thesis, opting for a relatively strict standard for temporal similarity.

Synchronicity Measure

Once the spike δ-trains are convoluted with Gaussian kernels, the PCC values of the network can be calculated and averaged to obtain the synchronicity measure. This involves comparing the convoluted spike δ-train signal of each neuron with

every other neuron in the network, summarized by a square matrix $P \in \mathbb{R}^{N\times N}$:

$$P = \begin{bmatrix} 1 & P_{12} & P_{13} & \dots & P_{1N} \\ P_{21} & 1 & P_{23} & \dots & P_{2N} \\ P_{31} & P_{32} & 1 & \dots & P_{3N} \\ \vdots & \vdots & \vdots & \ddots & \vdots \\ P_{N1} & P_{N2} & P_{N3} & \dots & 1 \end{bmatrix}, \tag{3.38}$$

where element P_{ij} is the PCC metric of the Gaussian-convolved spike δ-trains of neurons i and j. Note that the characteristics of the PCC measure yield $P_{ii} = 1$ and $P_{ij} = P_{ji}$ for all (i, j)[56, 57]. To extract a network synchronicity value the mean value $\mathrm{S_{PCC}}$ is taken over all the upper-triangular elements of the matrix:

$$\mathrm{S_{PCC}} = \frac{2}{N(N-1)} \sum_{i=1}^{N} \sum_{j=i+1}^{N} P_{ij}, \tag{3.39}$$

where P_{ij} are the elements of the P matrix described in equation 3.38. This value of $\mathrm{S_{PCC}}$ is chosen to quantify the degree of network synchronicity in the thesis. It is worth noting that the PCC value is not defined when no spikes are fired, as the spike δ-train signal is constant[57]. The thesis addresses this by leaving the undefined values out of the synchronicity estimation entirely (value is not added and the normalization factor $\frac{2}{N(N-1)}$ is adjusted accordingly). It is additionally worth noting that the total number of network spikes $|\nu|$ is not included as a normalization factor to the synchronicity measure. Increasing the total number of spikes also increases the likelihood of alignment between the spike trains of neurons, leading to an increase in the synchronicity factor $\mathrm{S_{PCC}}$ even no network synchronicity is visible in the spike raster plot.

3.5.2 Synchronicity Induction Techniques

Once the network synchronicity measure is established, the methodology in which the synchronous network states are induced is described. Two techniques in particular are utilized in order to induce network synchronicity in the thesis, referred to as the stimulus increase and weight search methods.

Stimulus Increase

The stimulus increase approach to network synchronicity involves increasing the degree of external stimulus in the network, increasing the number of external synapses $\mathrm{n_{idx}}$ which connect to each neuron in the network, as presented in section 3.1.6. Four levels of network stimulus increase are presented using $\mathrm{n_{idx}} \in [64, 128, 192, 256]$, and the network characteristics and kernel method performance metrics of each of these networks are presented in the results. The results include the spike raster of each network state, an image of all LFP signals registered, and a summary of the kernel method performance for each channel in each of the network states. The fashion in which the synapses are distributed to each neuron and the synaptic characteristics of the external synapses are kept consistent with the description given in section 3.1.6.

Weight Search

The other methodology used to induce synchronicity is referred to as the weight search methodology. This method is a more brute-force approach to synchronicity induction in the network. This method involves performing a grid search over a multitude of recipe network simulations, varying the excitatory and inhibitory synaptic weights ($\bar{g}_{\mathrm{syn,E}}$, $\bar{g}_{\mathrm{syn,I}}$) slightly for each network. The spike raster graphs of the networks are inspected, and four levels of synchronicity are picked out for use in the kernel method evaluation. These are picked to represent a gradual increase from weak- to strong levels of synchronicity, and it is important to keep the network firing rates $\bar{\nu}_p$ in mind when picking out the four networks. This was previously mentioned to be a factor which can impact the spike synchronicity measure $\mathrm{S}_{\mathrm{PCC}}$, and if the network firing rate changes drastically, then the potential differences seen in the kernel approximation might be a result of the firing rate change, rather than the synchronous nature of the network. The population firing rates $\bar{\nu}_p$ should therefore be kept as consistent as possible across the four weight search networks.

3.6 Biophysically Detailed Neuron Network

The following section describes how the baseline network is altered to include more biophysically detailed morphologies, and how the linear methods are evaluated in these new circumstances. The biophysically detailed network baseline is first established. This involves calibrating the network to have AI activity and firing rates below $\approx$ 10 Hz and applying the kernel method to establish the baseline method performance. A stimulus increase study similar to the one described in section 3.5.2 is then conducted on the biophysically accurate network, where the hybrid and kernel methods are applied to networks with various degrees of external drive $n_{idx} \in [64, 128, 192, 256]$ and the LFP approximation accuracies are evaluated relative to the ground-truth.

3.6.1 Hay Cell and Network Initialization

A neuron model from Hay et al. [65] which models a neocortical layer 5b pyramidal cell is implemented for the excitatory neuron population in the biophysically detailed network. This neuron morphology/model is referred to as the Hay cell from now on. There are a number of motivations behind implementing this neuron as the excitatory neuron model in the biophysically accurate network, and the geometry of the cell is a central one. The cell morphology is very detailed in that it has a large amount of compartments with varying dendritic widths, with long branching apical and basal dendrites. The structure of the Hay cell is depicted later on in the results section. An additional motivation of implementing the Hay cell is the complexity which arises from the various active, nonlinear ion channels distributed throughout the cell. The ion channels of the Hay cell include two Na^+ channels (Nat, Nap), three K^+ channels (Kp, Kt, Kv3.1), two Ca^{2+} channels (Ca_HVA, Ca_LVA), among others. The full list of ion channels included in the Hay cell are described in Hay et al. [65]. These nonlinear ion channel details are not accounted for in the BaS cells, and the complexity increase provides a challenge to the linear LFP approximation methods. The a new inhibitory population morphology is also implemented, in which the ball-and-stick model from table 3.3 with a shortened 'stick' section is used.

The network of Hay cells are observed to require $\approx$ 1000 ms to stabilize. The study therefore assigns a 1200 ms initialization time to the biophysically detailed network, adding an additional 2000 ms for linear method evaluation afterwards. The total simulation time parameter previously described in table 3.1 is reconfigured to $T_{sim} = 3200$ ms for this reason, keeping the other network parameters consistent with what was previously presented. Increased initialization and simulation times alter previously stated expressions slightly:

$$\bar{\nu}_p = \frac{|\nu_p|_{\geq 1200 \text{ ms}}}{N_p \cdot (T_{\text{sim}} - 1200 \text{ ms})}. \tag{3.40}$$

$$\bar{V} = \frac{1}{N} \sum_{j=1}^{N} \frac{1}{N_{t \geq 1200 \text{ ms}}} \sum_{t=1200 \text{ ms}}^{3200 \text{ ms}} V_{\text{soma},j}(t), \tag{3.41}$$

$$\phi^c(t_i) = \phi^c(t_i) - \frac{1}{N_{t \geq 1200 \text{ ms}}} \sum_{t=1200 \text{ ms}}^{3200 \text{ ms}} \phi^c(t). \tag{3.42}$$

These three equations are variants of equations 3.32, 3.34 and 3.42, respectively, altered to account for the additional 1000 ms of initialization time which is required for the biophysically detailed network. These serve the same purposes as before, where equation 3.40 is the population-specific firing rate expression, equation 3.41 is the post-synaptic membrane potential estimate, and equation 3.42 is the DC-removal signal post-processing step performed for all (c, t_i) as described in section 3.3.3.

3.6.2 New Configuration Parameters

A number of new network configuration parameters are introduced to accompany the change in neuron models. Mostly the network still follows the network configuration presented in section 3.1, though the parameters which are altered are listed in the following section. Firstly, the inhibitory neuron morphology is still the ball-and-stick neuron configuration presented in table 3.3, and the following new parameters define the shortened 'stick' of the inhibitory cell. The new dendritic morphology is listed in table 3.6.

	Variable	Description	Value
Dendrite		3D Spatial Information	
	(x_0, y_0, z_0)	Dendrite Startpoint	(0, 0, 15 µm)
	(x_1, y_1, z_1)	Dendrite Endpoint	(0, 0, 115 µm)
	(d_0, d_1)	Boundary Diameters	(3 µm, 3 µm)

Table 3.6: The altered dendritic morphology for the inhibitory neuron population in the biophysically detailed network. The dendritic length now extends upwards 100 µm instead of 1000 µm. The other parameters still follow table 3.3.

Cell Configurations and Positioning

The biophysically detailed network has a radius of $r_{\text{Nw}} = 100$ µm, and synaptic depth sampling of $z_{\text{soma}} \sim \mathcal{N}\big(0, (20\ \mu\text{m})^2\big)$, equivalent to what was presented in section 3.1.1. Note that a rotation of $\text{rot}_x = 4.729$ rad and $\text{rot}_y = -3.166$ rad is applied to the Hay cells at initialization. This is done to orient the apical dedrites of the Hay cell upwards along the z-axis, and illustrations of the morphologies are included in the initial biophysically detailed network results to inspect the cell placements and orientations.

Synaptic Positioning

The synaptic positioning configuration of the biophysically detailed network differs from the previous ball-and-stick (BaS) configuration presented in section 3.1.5. The synaptic depth-preferences of the biophysically detailed network are reconfigured and stated in table 3.7. Each synaptic type is listed individually, and a context is included for a better description of the synaptic connection. Section 2.1.3 stated that excitatory- and inhibitory synapses are often found

Synaptic Type	Context	Depth-preference PDF
E:E	Hay-to-Hay Excitatory	$\mathcal{N}\big(0, (100\ \mu\text{m})^2\big) + \mathcal{N}\big(500\ \mu\text{m}, (100\ \mu\text{m})^2\big)$
E:I	Hay-to-BaS Excitatory	$\mathcal{N}\big(100\ \mu\text{m}, (100\ \mu\text{m})^2\big)$
I:E	BaS-to-Hay Inhibitory	$\mathcal{N}\big(0, (100\ \mu\text{m})^2\big)$
I:I	BaS-to-BaS Inhibitory	$\mathcal{N}\big(0, (100\ \mu\text{m})^2\big)$

Table 3.7: Depth preferences of the biophysically detailed network. These depth preferences are combined with the area probability Pr^A_{jn} to find the normalized synaptic connection probability per post-synaptic cell compartment $\text{Pr}^{\text{syn},\,p}_{jn}$, as described in equation 3.12.

on apical- and basal dendrites, respectively. This was combined with the biophysically detailed excitatory and inhibitory morphologies to reconfigure the depth-preferences.

The E:E synaptic type now combines two equally weighed Gaussian distributions, and E:I connects to the end of the shortened apical dendrite introduced in table 3.6. The I:E and I:I synaptic types still have identical depth preferences, as the somatic compartments of the E and I populations are initialized around the same depth. Recall that the depth preferences from table 3.7 are combined with the area probabilities of each compartment Pr^A_{jn} to determine the synaptic connection probability $\text{Pr}^{\text{syn},p}_{jn}$, as was described in section 3.1.5. The results section includes the synaptic placements in the morphology illustrations to verify that the connections were configured correctly.

3.6.3 Morphology Stimulus Changes

Once the new network configuration is established, the external drive/stimulus needs to be recalibrated to reproduce the asynchronous irregular firing activity and population firing rates $\bar{\nu}_p$ which are not too large (preferably $\leq$ 10 Hz). The external drive of the BaS network is unlikely to produce similar AP firing activity in the biophysically detailed network. If the connectivity and stimulus levels were to remain unchanged, the Hay- and shortened BaS neurons would fire off APs far less- and more frequently than the baseline BaS neurons, respectively. This is due to the fact that the Hay cell and shortened BaS cell have far greater-, and lesser spatial extentions relative to the baseline BaS morphologies described in table 3.3. An equal amount of randomly distributed stimulating $\text{n}_{\text{idx}} = 64$ synapses on relatively larger and smaller cells would then cause the net stimulus to the soma to decrease and increase accordingly. This is closely tied to the area-probability Pr^A_{jn} which the n_{idx} synapses are distributed by (described in section 3.1.5), and the ICS potential decay factor λ presented in section 2.2.2.

Stimulus Normalization

To normalize the stimulus to the two new neuron models, an external stimulus n_{idx} scale factor is implemented and calibrated for each population $[\epsilon_{\text{E}}, \epsilon_{\text{I}}]$. These scale the typical n_{idx} factor such that $\text{n}_{\text{idx},\,p} = \epsilon_p\ \text{n}_{\text{idx}}$, yielding a new number of external stimulating synapses for each population. A combination $[\epsilon_{\text{E}} = 2, \epsilon_{\text{I}} = 0.5]$ would, for example, double the number of external stimulating synapses for the excitatory population and halve it for the inhibitory population. To

calibrate these, a large number of networks with various $[\epsilon_{\mathrm{E}}, \epsilon_{\mathrm{I}}]$ combinations are simulated, and the spike raster graphs and populational firing rates $\bar{\nu}_p$ are monitored. Firing rates which are similar to the recipe network presented in section 3.1 are considered a benchmark, though anything below 10 Hz should suffice.

Post-synaptic Potential Adaption

The post-synaptic membrane potential estimation $V \to \bar{V}$ is additionally adapted to fit the biophysically detailed network. The same procedure presented in section 3.4.2 is used, where the histogram displaying the mean somatic potentials across the network is used to determine the post-synaptic membrane potential estimate $\bar{V}$. However, due to the significant morphology differences between the E and I populations in the biophysically detailed network, the two populations are evaluated separately $V \to \bar{V}_p$. The synaptic weight conversion scheme $\bar{g} \to \bar{I}$ is then determined by the post-synaptic neuron population p, such that:

$$\bar{I}_{\mathrm{syn}} = \bar{g}_{\mathrm{syn}}(\bar{V}_p - E_{\mathrm{syn}}) \tag{3.43}$$

is the max synaptic current value $\bar{I}_{\mathrm{syn}}$ of the current-based synapse model from equation 2.27, and $\bar{V}_p$ is the post-synaptic membrane potential estimation for post-synaptic population p. The synaptic reversal potential E_{syn}, and synaptic rise- and decay-factors (τ_1, τ_2) are kept consistent with what was presented in table 3.3.

3.6.4 Methodology Limits and Evaluation

The aforementioned stimulus increase study from section 3.5.2 is conducted on the biophysically detailed network. This methodology regards increasing the external stimulus $\mathrm{n_{idx}}$ and investigating what impacts it has on the linear spike-LFP method performances.

Stimulus Increase

The value of $\mathrm{n_{idx}}$ is incremented in four steps, increasing from $\mathrm{n_{idx}} \in [64, 128, 192, 256]$ as previously presented in section 3.5.2. The calibrated normalization scales $[\epsilon_{\mathrm{E}}, \epsilon_{\mathrm{I}}]$ presented in section 3.6.3 are kept equal to their calibrated values throughout these increases, scaling the default $\mathrm{n_{idx}}$ population-specific external synapses $\mathrm{n_{idx},\, \mathit{p}} = \epsilon_p\ \mathrm{n_{idx}}$ for each $\mathrm{n_{idx}}$ increase.

Final Evaluation

A number of additional graphs are presented which were not included in the stimulus increase of the BaS recipe network presented in section 3.5.2. These compare:

1. 'Reference' signal, produced by the fully connected, active network.
2. Hybrid scheme signal, where synaptic activations are recreated using current-based synapses $\bar{g}_{\mathrm{syn}} \to \bar{I}_{\mathrm{syn}}$.

3. Kernel method signal, where the extracellular responses H_p^c of the synchronous firing of each current-based synaptic type are convoluted with the firing rates ν_p to obtain the LFP estimation according to equation 3.37.

Both the hybrid and kernel schemes are compared to the ground truth of the 'Reference' signal, and the differences between the two approximation methods reveal where the hybrid scheme could be preferable to the kernel method. The current study identifies regions in which the hybrid method outperforms the kernel method as:

$$\text{PCC}(\text{'Reference'}, \text{hybrid}) - \text{PCC}(\text{'Reference'}, \text{kernel}) > 0, \tag{3.44}$$

$$\text{MSE}(\text{'Reference'}, \text{kernel}) - \text{MSE}(\text{'Reference'}, \text{hybrid}) > 0. \tag{3.45}$$

Notice that the subtraction order is changed between the two metrics. This is due to the fact that the PCC and MSE metrics have large- and small- values indicate more accurate approximations, respectively. Regions in which these equalities are found to be true are then used to indicate where the hybrid method outperforms the kernel method, and where the kernel method should potentially not be applied.

3.7 Technical Details

A section on technical details is provided for reproducibility before the results are presented. The environments used for simulation are built upon multiple requirements and specific package versions which are documented here.

3.7.1 Code Availability

A repository containing code developed for the thesis is made publically available on GitHub (see `https://github.com/steinnhauser/linearLFP`), and includes two central folders - one containing the recipe BaS configuration `recipeBaS` and the other the Hay cell configuration `detailedHay`. An additional folder `misc` containing scripts used to plot example figures in the thesis is also included. The thesis utilizes a forked version of the LFPy package (see `https://github.com/LFPy/LFPy`), where customized utilities were added for the thesis objectives. The forked version can be found at (`https://github.com/steinnhauser/LFPy`) and 'git' (`git-scm.com`) can be used for tracking the code origin and history. Additional utilities were developed and implemented for multiple miscellaneous purposes including plotting and signal processing. These utilities are also publically available at (`https://github.com/steinnhauser/linearLFP_utils`).

3.7.2 Simulation Requirements

All code written for the thesis is written in the object-oriented programming language `Python` (`https://python.org`). The following section describes the python packages and libraries which were utilized in the thesis, along with the specific versions used. The simulation code used Python (v3.8.5), numpy (v1.20.1), Cython (v0.29.22), mpi4py (v3.0.3), NEURON (v7.8.2), and SciPy (v1.6.1). LFPy (v2.1.1) was forked and customized. Other packages include h5py (v3.1.0) and pandas (v1.2.2) for data storage and matplotlib (v3.3.4) for plotting. For details on how the signals were low-pass filtered, see the Elephant (v0.10.0) [66] and SciPy (v1.6.1) [67] documentation on the `butter` and `filtfilt` methods.

3.7.3 Computational Facilities

The ball-and-stick network simulations were conducted in parallel (4 threads) on 1.60 GHz Intel Core i5-8250U CPUs running on Ubuntu 20.04.2 LTS. The biophysically detailed network simulations presented in section 3.6 were conducted in parallel (512 threads) on the JUSUF cluster module in the Jülich supercomputing centre (`https://fz-juelich.de/`). The JUSUF hardware configuration consists of 2.25 GHz AMD EPYC 7742 CPUs running the CentOS 7 Linux distribution, and the full specifications of the JUSUF cluster can be found at (`https://apps.fz-juelich.de/jsc/hps/jusuf/cluster/configuration.html`).

Chapter 4

Results

The results from the recipe ball-and-stick (BaS) network from section 3.1 are first presented, followed by the respective hybrid- and kernel approximations. These are presented to establish the baseline network activity and baseline hybrid- and kernel method performances. Afterwards, the results from the stimulus increase and weight search methods from section 3.5.2 are presented. These should reveal if the kernel method performance is impacted by the network conditions discussed in section 3.5.2. Finally, the results of the biophysically detailed network are presented, following what was described in section 3.6. A baseline network and baseline linear method approximation performances are first established, identifying how the kernel method performs with the complex morphology of the Hay cell. The biophysically detailed network is then stimulated with increased external drive n_{idx} and the kernel method performance is evaluated under these conditions. The hybrid- and kernel methods are then compared to investigate if the two linear method performances differ in the biophysically detailed network.

4.1 Recipe-, Hybrid-, and Kernel Implementations

The results of the baseline BaS network configuration from section 3.1 and the linear method implementations described in section 3.4 are presented. The performances of the hybrid- and kernel approximations are compared in relation to the 'Reference' recipe BaS network extracellular potential signal.

4.1.1 Recipe Network

Figure 4.1 illustrates the distribution of 25% of the 1280 neuron population for clutter reduction. The morphologies are depicted by inserting a dot in the soma compartment and connecting the first and last dendritic compartments with a line. Note that the dot and line diameters are not accurate to the morphologies, though the neuron placements and dendritic branch lengths are.

Figure 4.2 illustrates the spike raster plot of the recipe network. Each dot represents the AP firing of a neuron, where the x-axis is the time and the y-axis

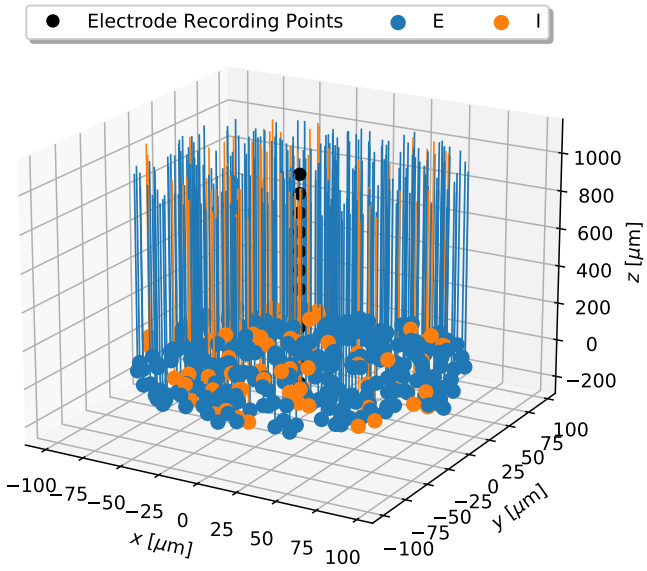

Figure 4.1: Distribution of 25% of the total population of the recipe network. Neurons from both the excitatory and the inhibitory populations are illustrated, with the central recording electrodes visible in the middle.

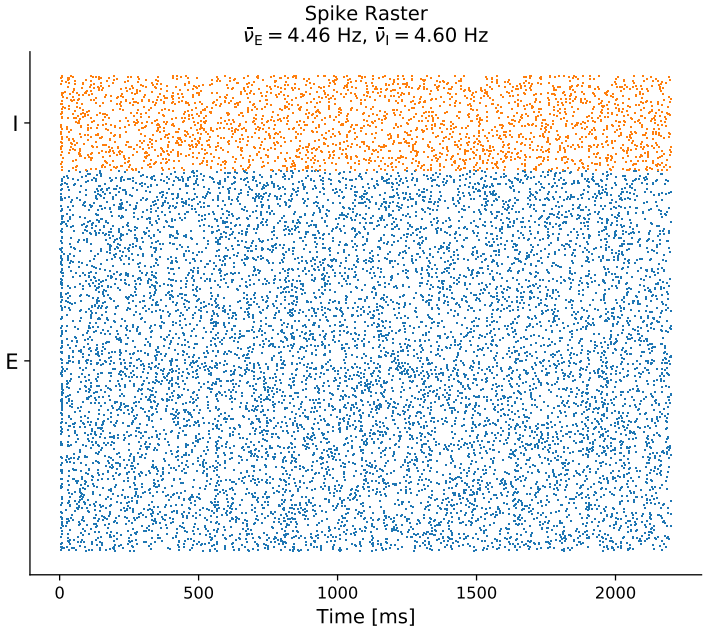

Figure 4.2: Spike raster of by the recipe network simulation. The estimated population-specific firing rates $\bar{\nu}_p$ are calculated according to equation 3.32.

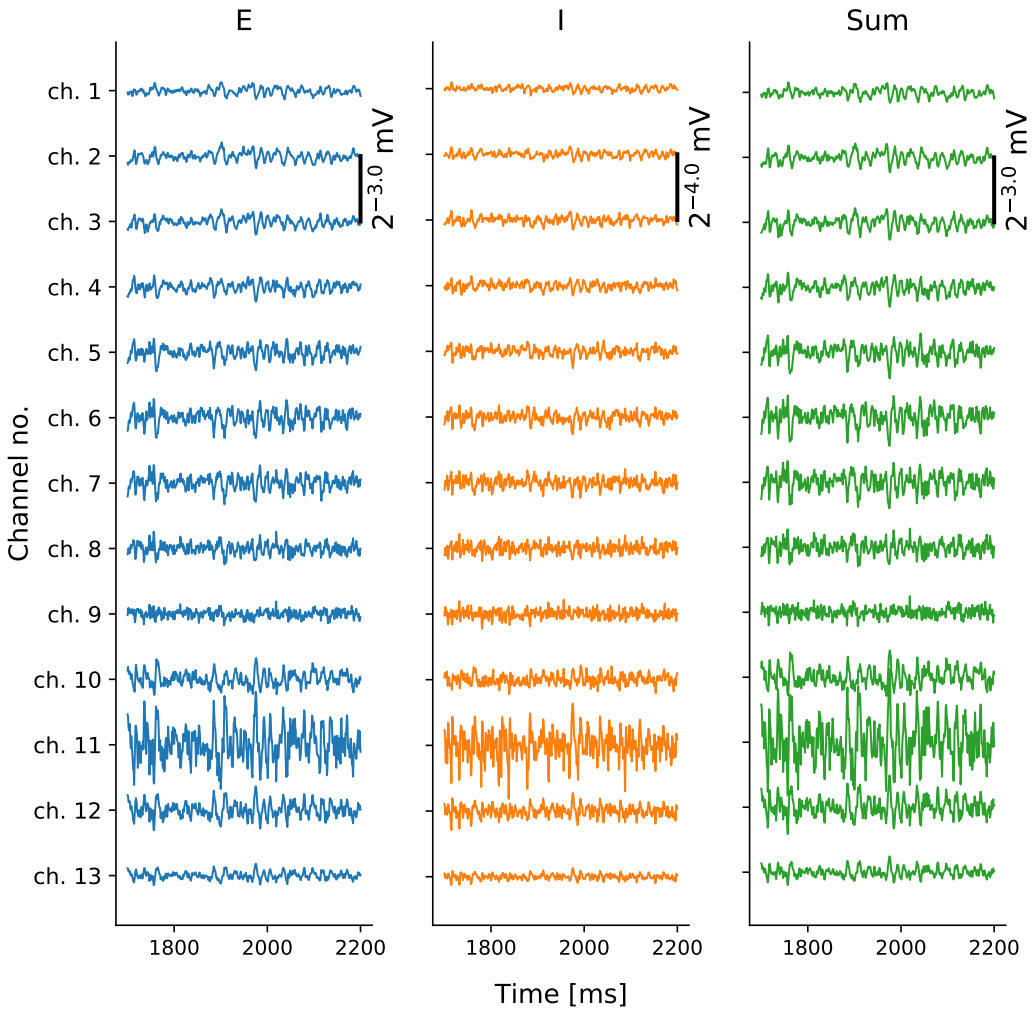

Figure 4.3: Raw extracellular potential signals of all electrode channels 1-13 for the recipe network. The signals from each population and the network sum are illustrated separately.

is the neuron ID. The y-axis distinguishes between the two populations instead of listing all neuron IDs. The entire 2200 ms of simulation is included, and the first 200 ms are considered as the startup transient time. The firing rate for each population is illustrated above the spike raster plot, calculated using equation 3.32.

This network condition is stochastic and noisey, with few significant structures in network firing times. Such activity is good for the baseline recipe network, as asynchronous irregular (AI) firing patterns are observed in cortex[52]. Inhibitory neurons are also found to have higher firing rates in cortex when the network activity is relatively low[52]. The inhibitory population firing rate in figure 4.2 is slightly larger than the excitatory $\bar{\nu}_{\mathrm{I}} > \bar{\nu}_{\mathrm{E}}$, though not by a large margin.

Figure 4.3 illustrates the raw extracellular potential recordings of each recording electrode channel. The signal amplitudes of the I population are found to be 1/2 that of the other two, a combination of the population size difference and the conductance-based synapse model weight difference $\bar{g}_{\mathrm{I}} > \bar{g}_{\mathrm{E}}$ described in table 3.4. Recall the coordinates of each recording electrode channel described in table 3.2, indicating that the high frequency components of the extracellular potential signals around channel 11 are a result of somatic AP firing activity.

4.1.2 Conductance-based Hybrid Model

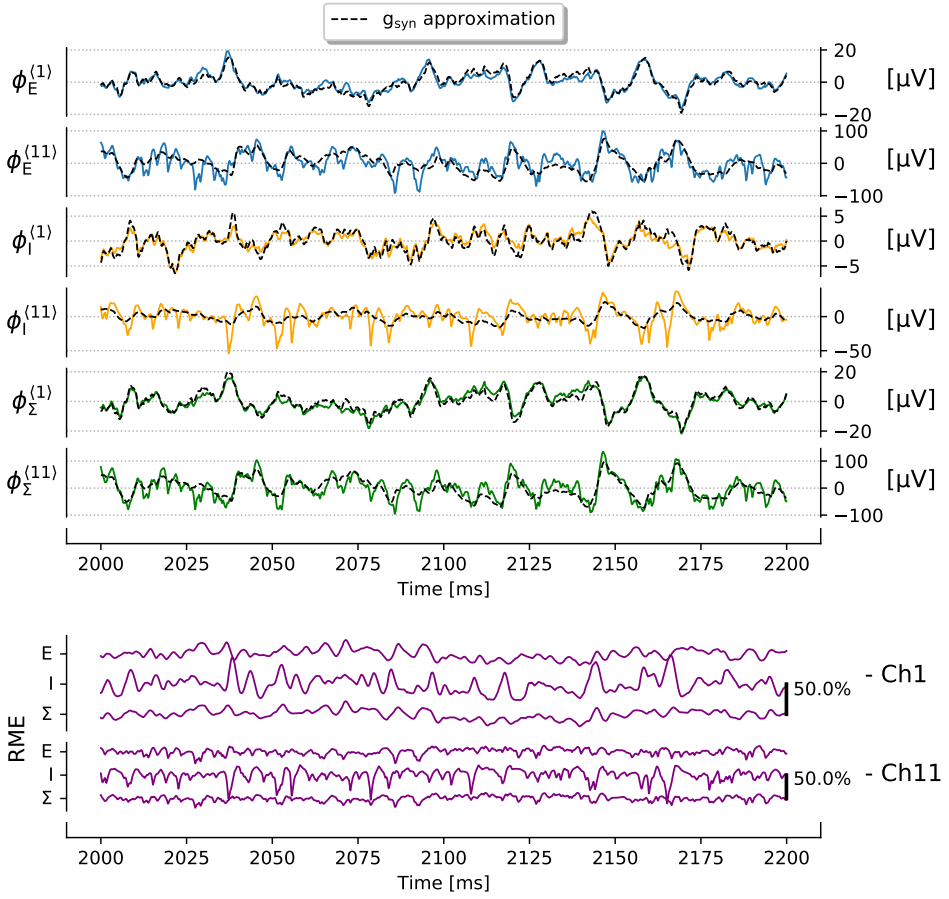

Figure 4.4: Raw extracellular potential recordings of the fully connected, active network (populations of E, I and their sum Σ depicted in blue, orange and green, respectively), and the conductance-based synapse hybrid model $\mathrm{g}_{\mathrm{syn}}$. Only channels 1 and 11 are illustrated, as channel 1 sees minimal somatic activity whereas channel 11 is very close to the soma. The RME of each signal combination is included below.

Figure 4.4 illustrates the full raw extracellular potential recordings of the fully connected, active conductance recipe network in relation to the conductance-based hybrid model approximation from in section 3.4.2, denoted as g_{syn}. Note that the conductance-based hybrid model is not a linear model, as it depends on both the post-synaptic membrane potential and time $I^{g}_{syn}(V,t)$, as expressed in equation 2.22. This model is later linearized by conversion to the current-based synapse model I^{i}_{syn}, as described around equation 2.28. The largest difference between the conductance-based hybrid approximation and the ground-truth signal is in channel 11, where somatic activity is most prominent. This is clearest in the raw extracellular potential signal of the inhibitory population $\phi_{I}^{\langle 11 \rangle}$, and can also be seen by the high frequent oscillations of signals $\phi_{E}^{\langle 11 \rangle}$ and $\phi_{\Sigma}^{\langle 11 \rangle}$

The RME signals below visualize the relative max error for each signal type, described in equation 3.22. The inhibitory population is found to have the largest relative error in channel 11. This is likely a result of the lesser signal amplitude, as the relatively small inhibitory population causes each AP firing to be more influential in the RME. This is also true for channel 1, and a current dipole-like pattern can be seen. The high frequent extracellular signals of the AP seen in channel 11 have equal and opposite spikes in the inhibitory population RME in channel 1. These are most visible for the inhibitory population, in particular at times $t_i \approx 2037$ ms, $t_i \approx 2145$ ms and $t_i \approx 2165$ ms.

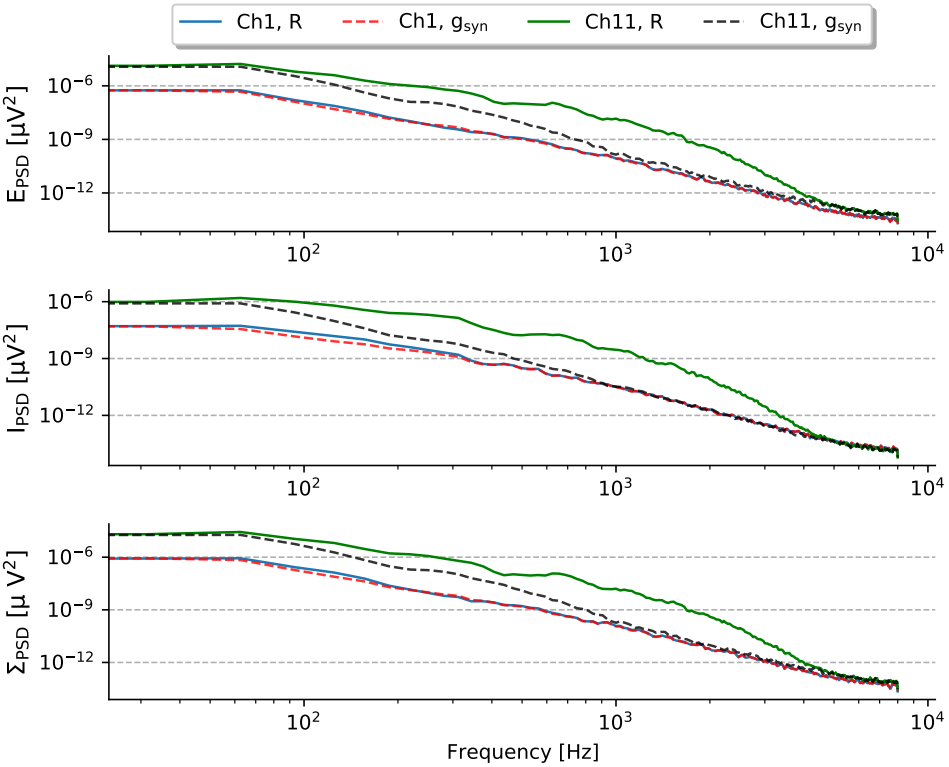

Figure 4.5: Power spectral densities (PSD) of the raw extracellular potential signals of channels 1 and 11. R signifies the 'Reference' signal.

Figure 4.5 presents the PSD calculations of the raw extracellular potential signals from figure 4.4. The ground-truth signals in which the network is fully connected and has active conductances are denoted as R, representing the 'Reference' signals. The PSD values of the dotted red- and blue lines are more or less equal, indicating that the 'Reference' signal is accurately approximated by the conductance-based hybrid model in regions far from the soma. This indicates that the extracellular potential signal far from the soma is largely a result of synaptic activity.

The black dotted- and green lines have significant differences, where high frequent somatic activity from the 'Reference' signal in channel 11 is prominent throughout the frequency spectrum. Recall that the conductance-based hybrid method has inactive conductances in the soma, such that this difference is expected. Note that the black dotted- and green lines are also separated by a fairly large margin at ≤ 300 Hz . This is the critical frequency used to obtain the LFP signal, and figure 4.5 reveals that the LFP signal still has trace contributions from somatic AP firing below this frequency. The somatic activity artifacts of the 'Reference' signal below 300 Hz are a consistent inaccuracy of the LFP approximation models presented later on.

4.1.3 Current-based Hybrid Model

Transitioning into the current-based synapse hybrid model, recall the process of synaptic model conversion $\bar{g} \rightarrow \bar{I}$ described in equation 2.28 and section 3.4.2. The somatic potential distributions are evaluated for the membrane estimation $V \rightarrow \bar{V}$, then the conversions $\bar{g} \rightarrow \bar{I}$ from equations 3.35 and 3.36 are used to produce the current-based hybrid model synaptic weights.

Figure 4.6 illustrates the distributions of the per-neuron mean soma potentials, as described in section 3.4.2. The mean of the somatic potential means, as presented in equation 3.34, yields the network somatic compartment potential estimation to be $\bar{V} \approx -64$ mV. Recall that the distributions presented in figure 4.6 are obtained from the active, fully connected recipe network. Note that the population-specific mean values are very similar, such that a population specific value $\bar{V}_p$ is not required.

To better view how potentials distribute inside the neurons, figure 4.7 illustrates the membrane potential distributions of a single randomly chosen neuron in the active, fully connected network. For each recording electrode channel, the neuron compartment which was closest to that channel was chosen, and the distribution of the compartment potential is illustrated as a boxplot. Note that channels 12 and 13 are not included, as the somatic compartment was the closest for them and is already depicted by channel 11. The AP firings of the neuron can be seen in the somatic compartment closest to channel 11, and the AP can be seen conducting into neighboring compartments by the red $> 95\%$ fliers. The mean value depicted by the orange lines is of most interest, differing by ≈ 5 mV between the compartments closest to channels 1 and 11. This indicates that the $V \rightarrow \bar{V}$ estimation, using the somatic compartment mean value as the general post-synaptic membrane potential, is reasonable for the recipe network.

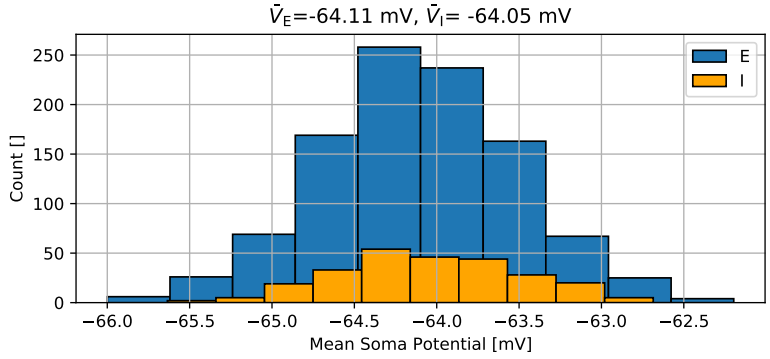

Figure 4.6: Distributions of the mean soma compartment potential values in the recipe network. The mean of the somatic membrane potential means is set to $\bar{V} \approx -64$ mV in the recipe BaS network.

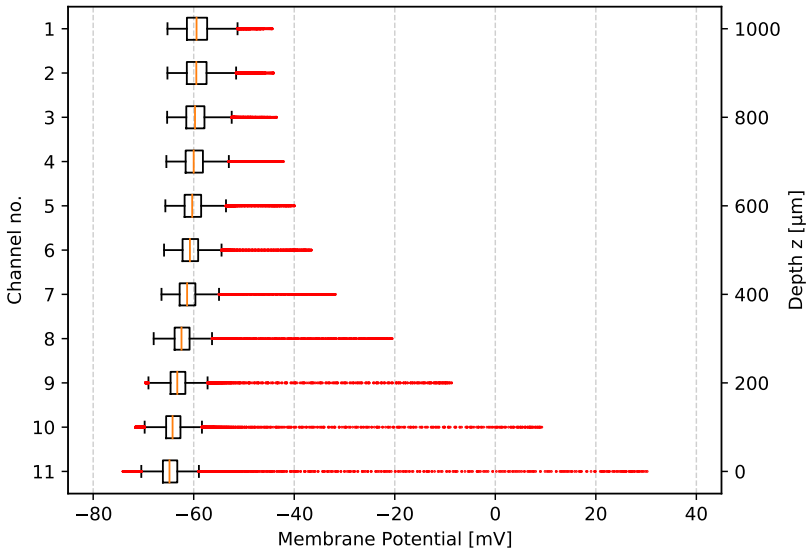

Figure 4.7: Membrane potential distributions across multiple compartments of a single neuron. Compartments which are the closest to the indicated electrode channel depths are chosen. The outliers of the distribution ($< 5\%$ and $> 95\%$) are illustrated by the red dots, and the mean potential value of the compartment is depicted by the orange line inside the box.

To compare the three signals presented, figure 4.8 illustrates the extracellular potentials of all three signals for channels 1 and 11. Note that the current-based hybrid model is linear, and is very similar to the non-linear conductance-based hybrid model throughout. These both are still found to differ from the high frequent somatic activity of the 'Reference' signal in channel 11. Although the conductance-based hybrid model signal is slightly more similar to the 'Reference' signal than the current-based hybrid model signal, figure 4.8 affirms that the $V \to \bar{V}$ synapse conversion for the current-based hybrid model is successful.

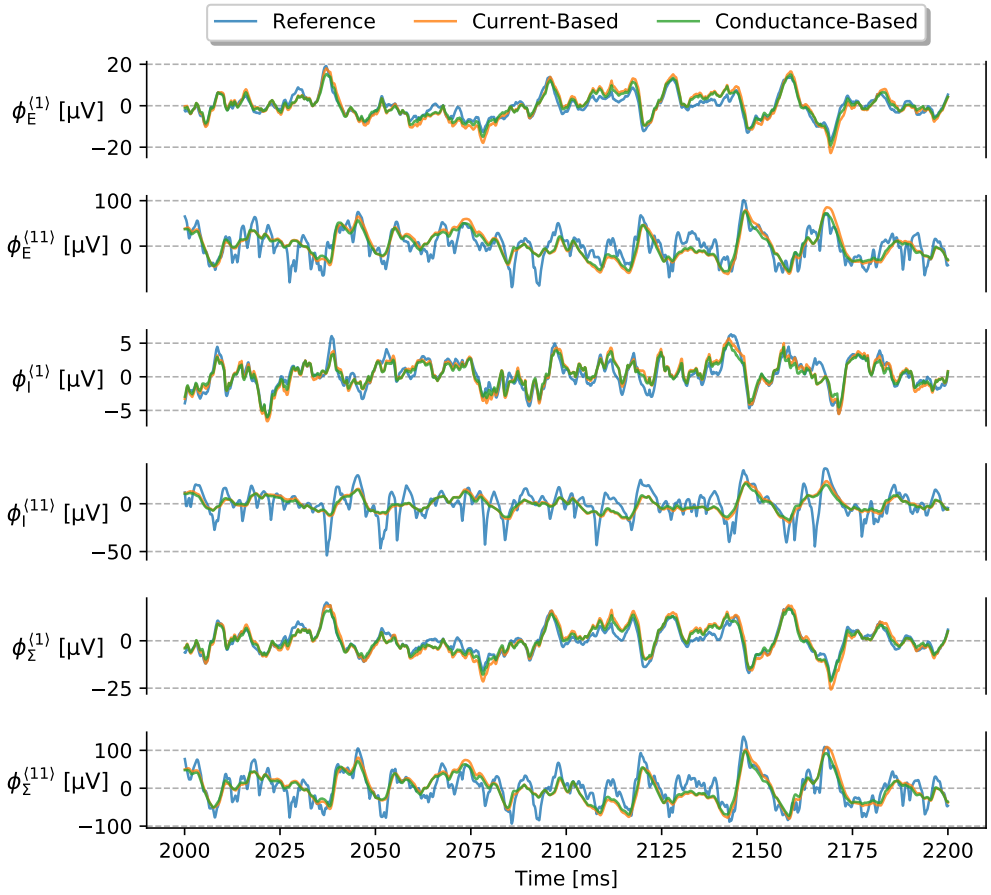

Figure 4.8: 'Reference' signal compared to the two hybrid method predictions. $\bar{V} = -64$ mV is used to convert $\bar{g} \to \bar{I}$ in equations 3.35 and 3.36 for the current-based hybrid method signal.

The fact that the linear current-based hybrid model performed well indicates that the recorded extracellular potential signals are linearly dependent of the spikes of the recipe network, and is a promising find in relation to the kernel method.

4.1.4 Kernel Method

The current-based hybrid model approximation indicates that a linear spike-LFP model correlates well with the 'Reference' signal, and the kernel methodology results are presented in the following section to build further upon this. Note that the 'Reference' and linear method approximation signals are lowpass filtered ≤ 300 Hz to obtain the LFP approximation from now on. The LFP signal from the full population, previously referred to as Σ in figures 4.4 and 4.8, is also exclusively illustrated from now on.

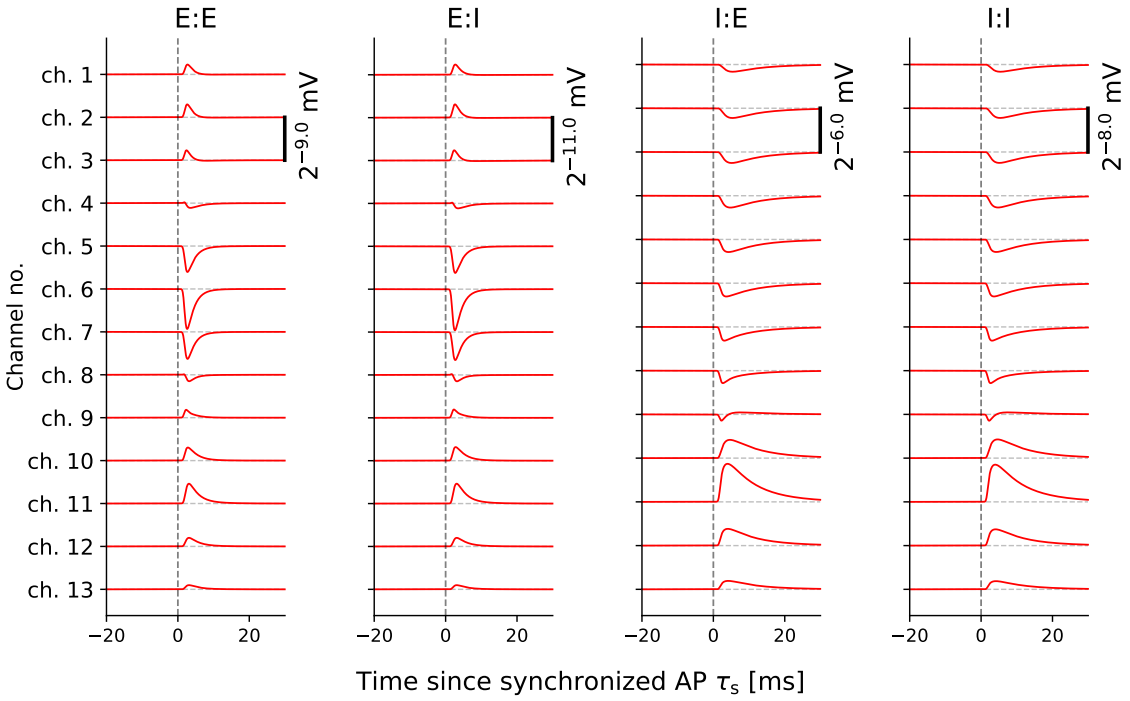

Figure 4.9: Raw extracellular potential responses from each channel for each synaptic type. A segment $[\tau_s - 20\text{ms}, \tau_s + 30\text{ms}]$ of the kernels is illustrated, though the total kernel signals extend 100ms in each direction from the synchronized AP time τ_s.

The kernels H_p^c obtained from the synchronous firing of the synapse types are illustrated in figure 4.9. As a reminder of section 3.4.3, these were obtained by setting up the synapses from the 'Reference' network, and firing them in a synchronous fashion, recording the extracellular potential response. This is done using a current-based synapse model, converted using a post-synaptic membrane potential estimation of $\bar{V} = -64$ mV. The resulting exctacellular response is subsequently divided by the number of neurons in the pre-synaptic population, yielding the net extracellular potential response of AP firing per neuron in that population H_p^c.

As mentioned before, the effective single kernel of population E is the sum of the synapse types E:E and E:I displayed in the figure, $H_{\text{E}}^c = H_{\text{E:E}}^c + H_{\text{E:I}}^c$. The details of the various synaptic connection types are however interesting to see for themselves. The kernels illustrated in figure 4.9 are not post-synaptic neuron population dependent, meaning that E:E and E:I are practically identical in shape. The amplitude difference between the two is caused by the fact that the excitatory population is four times larger than the inhibitory population. This is also true for the I:E and I:I kernels.

The kernels reflect the fact that the excitatory synapses yield positive stimulus into the dendrites and the inhibitory synapses yield negative stimulus into the somatic region, following the depth-preferences presented in equations 3.9 and 3.10. This is visible by the negative extracellular potential response around

channel 6 for the E:E and E:I synapse types, and the positive extracellular potential response around channel 11 for the I:E and I:I synapse types, respectively. The extracellular contributions of opposite sign in channels surrounding these are products of Kirchoff's law and the neuron acting as a dipole, as discussed in section 2.3.3.

A note on extracellular potential contribution per population is in order, as figure 4.9 reveals the amplitudes of the I:E and I:I kernels to be significantly larger than those of the E:E and E:I synapse types. This is a result of the stronger inhibitory synaptic weights listed in table 3.4, and does not necessarily imply that the inhibitory kernels contribute more to the full LFP signal produced by equation 3.37. Given that the E population is four times larger than the I population, a similar population firing rate $\bar{\nu}_{\mathrm{E}} \approx \bar{\nu}_{\mathrm{I}}$ implies that the amplitude of the populational spike trains are related by $\nu_{\mathrm{E}} \approx 4\nu_{\mathrm{I}}$ [1]. An even LFP contribution between the two populations is then obtained if the inhibitory kernel amplitude is four times larger than that of the excitatory $4H^c_{\mathrm{E}} \approx H^c_{\mathrm{I}}$ to account for the spike train amplitude difference. Figure 4.9 reveals this amplitude difference to be approximately $8H^c_{\mathrm{E}} \approx H^c_{\mathrm{I}}$, indicating that the inhibitory population likely contributes two times more to the LFP signal than the excitatory population, as the firing rates were found to be similar $\bar{\nu}_{\mathrm{E}} \approx \bar{\nu}_{\mathrm{I}}$ in figure 4.2. The subject of which population contributes most to the resuling LFP signal approximation is a relevant subject in the biophysically detailed morphology results.

Finally in figure 4.9, the inhibitory kernels are found to be wider than the excitatory kernels, in part due to the decay constants of the synapses presented in table 3.3. Section 3.2 briefly mentioned the impact wide kernels have in convolution, shown in figure 3.1 to have a low-pass filtering effect on the output signals. The low-pass filtering effect of wide kernels is due to the low-frequency content of the kernel, and is not specific to the convolution operation. A low-frequent filter results in a low-frequent output if a Finite Impulse Response (FIR)[68] filter formalism was used instead. An additional factor is referred to as 'processing gain' in signal processing, where the larger the gain, the more the contribution to the convolution outcome. The gain for each kernel is related area under the curves, and the inhibitory synapses are found to have larger gain. The impacts of the kernel widths and amplitudes should be kept in mind, as it is also a central point of discussion later on.

As a comparison of the kernel method in relation to the current-based hybrid method, figure 4.10 illustrates the LFP signals as well as the PCC and MSE evaluations of the signals. Recall from section 3.3.1 that the PCC measure evaluates the variances/shapes of two signals, while the MSE measure evaluates the mean squared amplitude difference of the two.

Note that the two evaluation metrics are benefited by longer signal lengths, the PCC metric in particular. An evaluation time of 2000 ms is sufficient for the current study, but a simulation time increase would yield a more rigorous PCC evaluation of the methods. This is due to the metric then converging to a so-called consistent estimator[69, 70]. The LFP signals and evaluation metric

[1] Recall that the populational firing rate $\bar{\nu}_p$ is normalized to the number of neurons in the population, as per equation 3.32

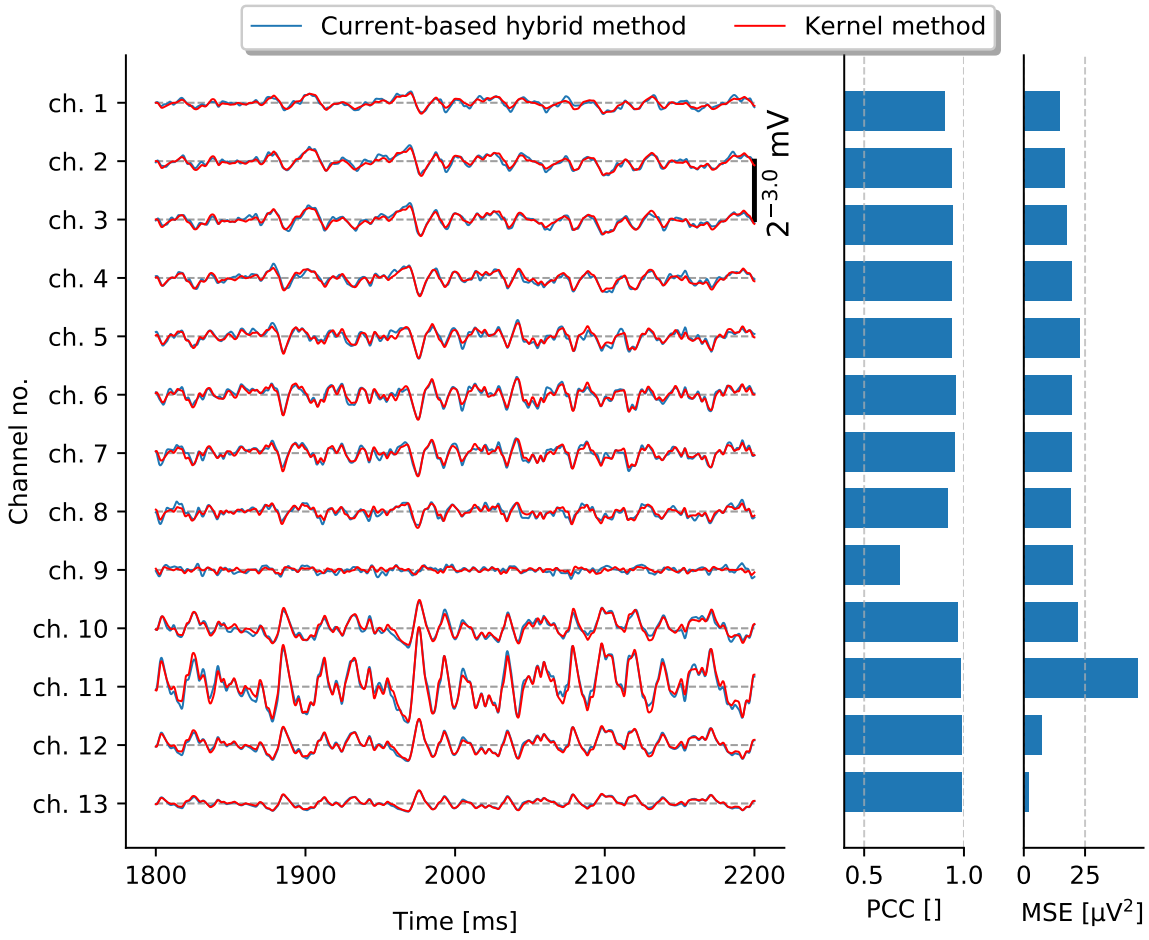

Figure 4.10: Comparison between the current-based hybrid model and kernel method LFP approximations. The PCC and MSE metrics from equations 3.25 and 3.23 are included for shape- and amplitude evaluations respectively. Recall that the first 200 ms are not included in the evaluation metrics.

values of figure 4.10 all point to a successful kernel method performance. Keep in mind that the 'Reference' LFP signal is not included in figure 4.10, though the current-based hybrid model was previously found to successfully recreate the raw extracellular potential of the 'Reference' signal in figure 4.8.

Channel 9 is found to have the lowest PCC metric performance in figure 4.10. Figure 4.9 reveals that a change in polarity for both the excitatory and inhibitory kernels occurs in the region around channel 9, resulting in a small extracellular potential response in the kernels $H_p^{\langle 9 \rangle}$. The inaccuracies of channel 9 can therefore be attributed to the local cancellations of channel 9 seen in the kernels, and the kernel recreation performance drop in polarity transition regions was also found to be the case in Hagen et al. [3].

Finally, the largest MSE metric value is found in channel 11, the rest of the MSE metrics being below 25 μV^2. The MSE metric being maximal in the

channel with the largest amplitude is to be expected, and an error of $\approx 50\ \mu V^2$ is still regarded as a successful kernel method recreation. The best channel in terms of the evaluation metrics in figure 4.10 is channel 13, where the PCC is ≈ 1, and the MSE is at a minimum. The linear method performances are however expected to drop in relation to the 'Reference' LFP in regions where somatic activity is prominent.

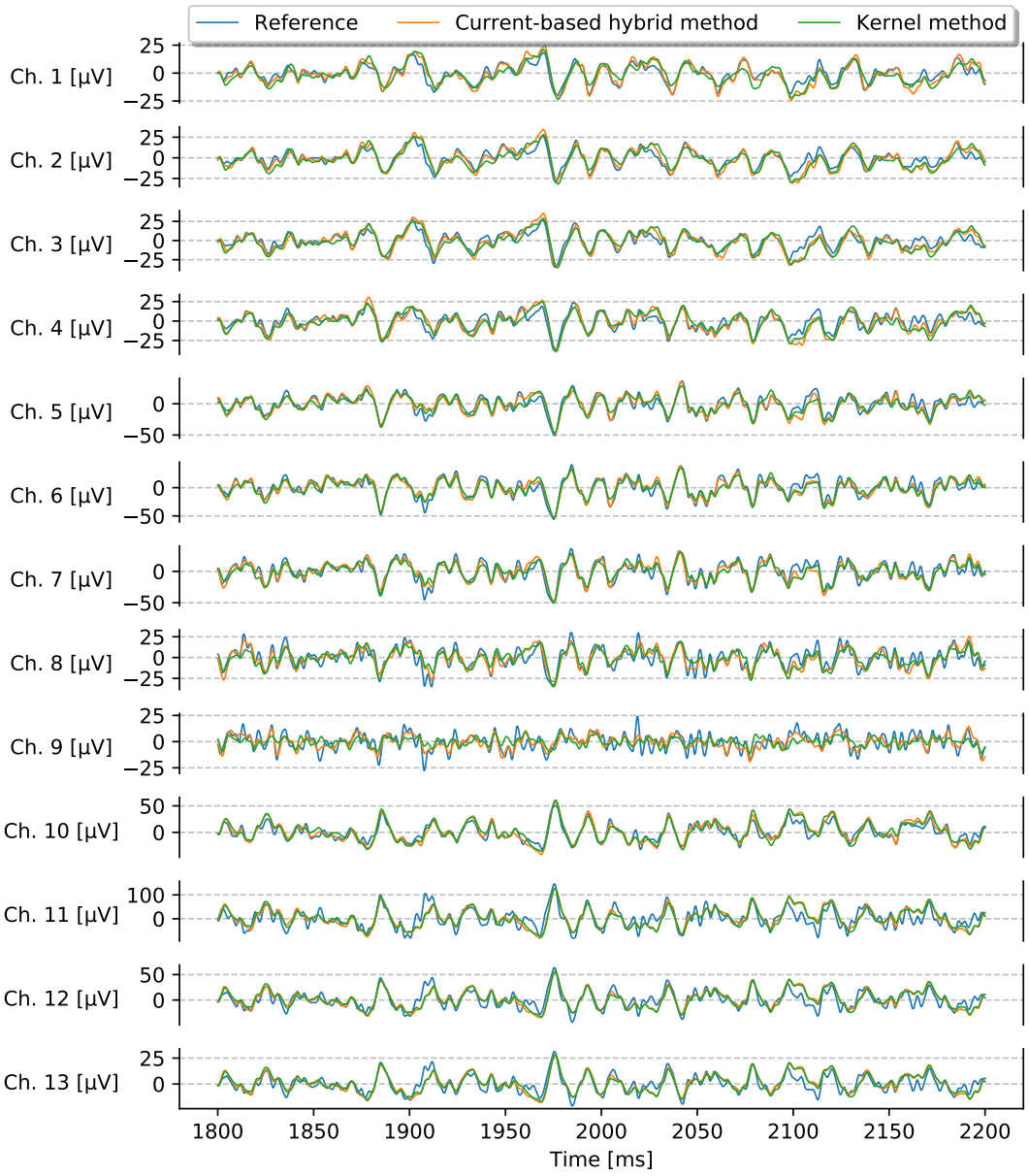

Figure 4.11: Full image of the 'Reference'-, current-based hybrid-, and kernel LFP signals for the recipe BaS network.

Figure 4.11 illustrates the 'Reference' LFP signal in relation to the current-based hybrid- and kernel method LFP approximations. Both linear approximation methods recreate the 'Reference' successfully, though the high frequency content of the 'Reference' signal provides challenges to both approximations. The current-based hybrid model performs slightly better than the kernel method in figure 4.11, though the difference is marginal. The baseline BaS network 'Reference' LFP signal is found to be very linearly dependent of the spiking activity.

4.2 Methodology Limits

The methodology limit results are presented, where the kernel method performance is evaluated under various network conditions, as described in section 3.5. Note that the evaluation metrics use the last 2000 ms of the signals.

4.2.1 Stimulus Increase

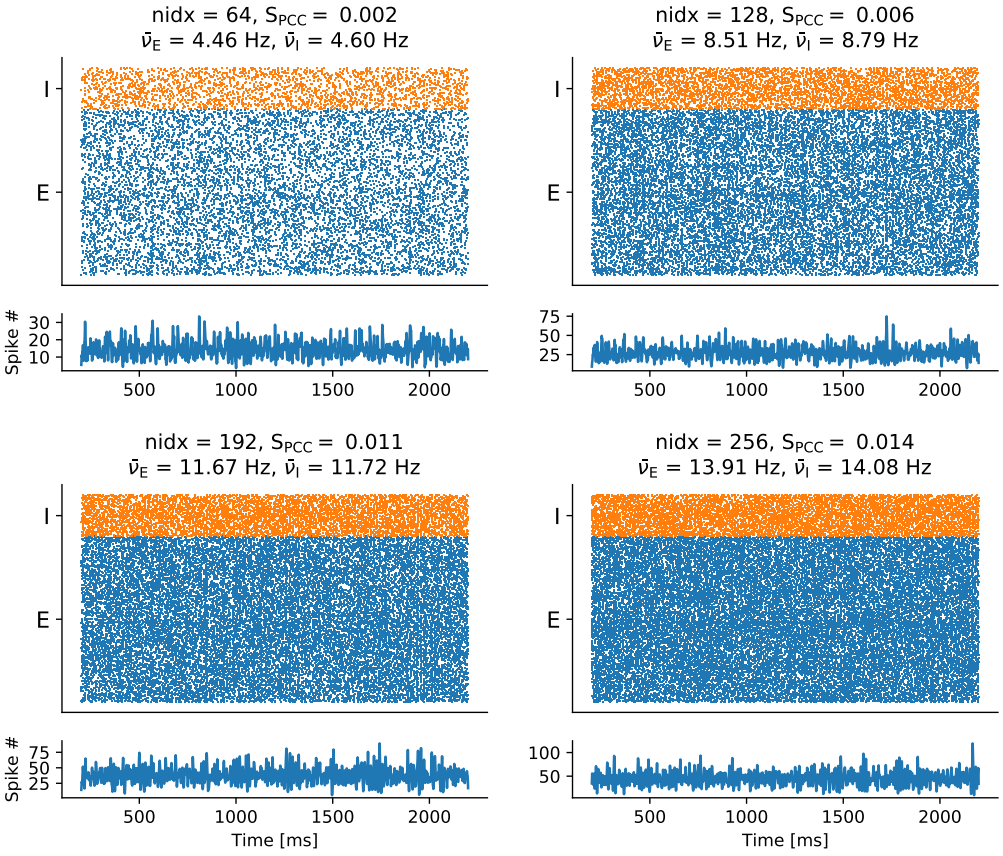

Figure 4.12: Spike raster plots for each stimulus increase network. The stimulus per neuron n_{idx}, network firing rate per population $\bar{\nu}_p$ from equation 3.32, and network synchronicity metric S_{PCC} from equation 3.39 are included. Below each spike raster is a smoothed total number of network spikes per time.

Figure 4.12 illustrates the spike rasters and firing rate summaries of the four networks of the stimulus increase study. These spike rasters provide a context of the four network states in which the kernel method is applied. The increase in stimulus per neuron n_{idx} produces a large increase in network activity across the four cases, increasing from a network firing rate of ≈ 4.5 Hz to around 14 Hz. The synchronicity measure is seen to increase for increased n_{idx}, though synchronous firing structures (i.e. clear vertical line patterns) are not seen in the spike rasters. Section 3.5.1 presented the synchronicity measure S_{PCC} by noting that the measure is not normalized according to the total number of network spikes $|\nu|$. The networks synchronicity measures S_{PCC} of figure 4.12 are therefore considered unreliable. The total number of network spikes for each network differ too much.

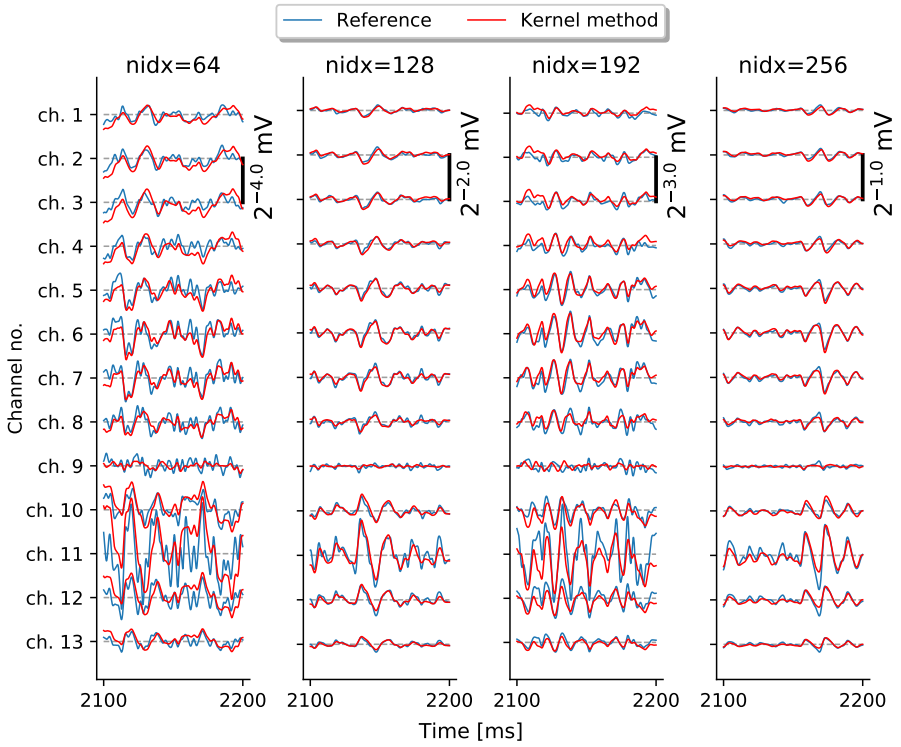

Figure 4.13: 'Reference' and kernel method LFP signals for each n_{ids} value of the stimulus incease study.

Figure 4.13 illustrates the LFP signals of the 'Reference' and the kernel approximation for each of the outside stimulus values n_{idx}. Only the last 100ms of the signals is included for a more detailed look of how well the signals match up. The kernel approximations perform well for all four networks, though the high frequencies of the 'Reference' signal in the $n_{idx} = 64$ column seem to provide large inaccuracies. It is likely that the inaccuracies between the two signals are more visible due to the scale/amplitude, as the other columns are scaled to eight times larger at most, and the same level of detail is not visible.

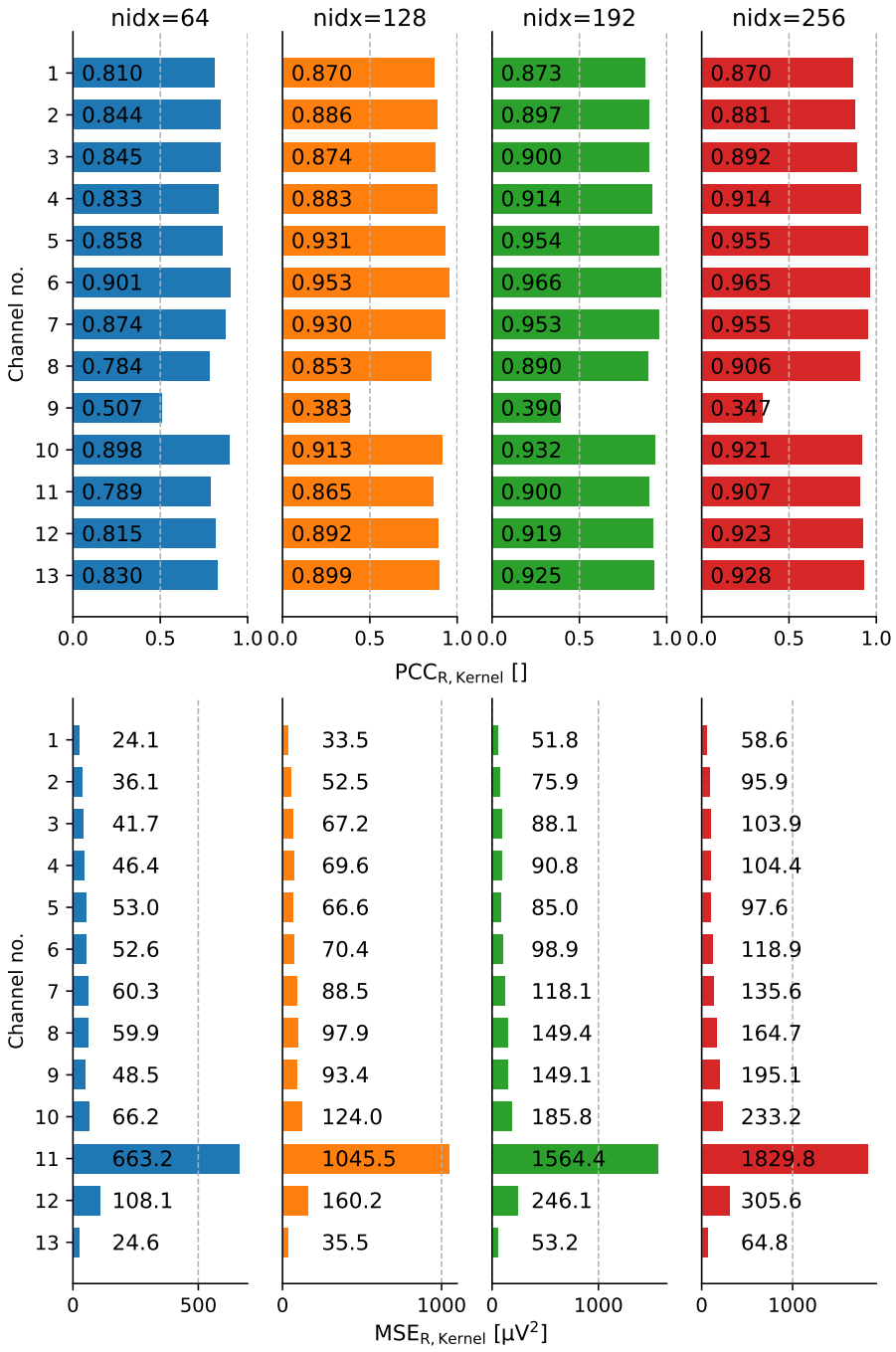

Figure 4.14: Top row: The PCC evaluation metric results of the 'Reference' and kernel signals of each channel. Bottom row: The MSE evaluation metric results of the 'Reference' and kernel signals of each channel. The four stimulus increase cases are sorted into the four columns.

To evaluate the 'Reference' and kernel signals, figure 4.14 lists both PCC and MSE evaluation metrics for all channels, and for each n_{idx} network. The kernel signals are found to perform very well in approximating the 'Reference' signals for all n_{idx} network states. Disregarding channel 9, each of the three columns $n_{idx} \in [128, 192, 256]$ have PCC values which are well above 0.850. The low PCC values of $n_{idx} = 64$ are to be expected, as figure 4.13 revealed this network state to have significantly lower LFP signal amplitudes, indicating that small fluctuations can have relatively large impacts on the PCC. Finally, the MSE is smallest in $n_{idx} = 64$ and consistently increases for a larger amount of network stimulus n_{idx}. This is also a product of the network amplitude differences, where the largest LFP signal amplitude was found in column $n_{idx} = 256$. The stimulus increase provided no negative impact to the kernel method performance.

4.2.2 Weight Search

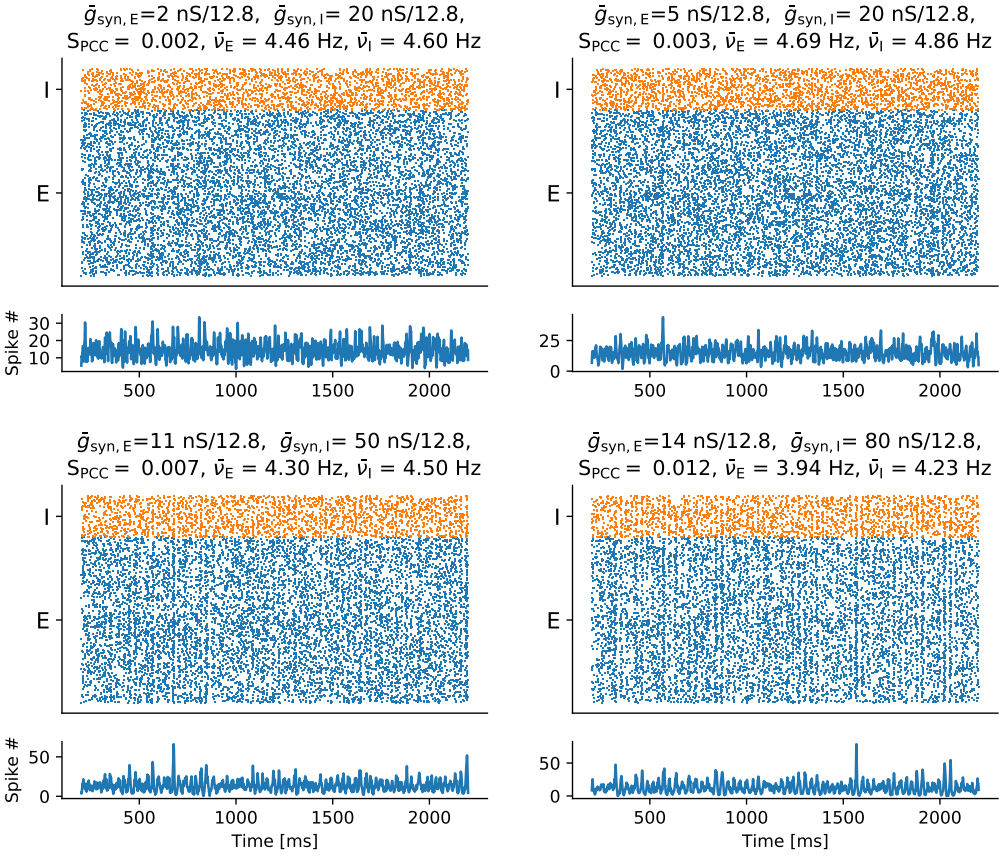

Figure 4.15: Spike raster plots of the weight search networks. The conductance-based synapse weights used are listed above each spike raster. Synchronicity S_{PCC} and firing rates ν_p are included, and a smoothed total network spikes per time is included below each spike raster.

The weight search study follows the same procedure as the simulus increase study, and figure 4.15 illustrates the four spike raster plots of the weight search study. Recall the fashion in which the weights are initialized and converted. The weights listed in figure 4.15 are used as mean values μ for sampling $\mathcal{N}(\mu, \sigma^2)$, as listed in table 3.4 and described in section 3.4.2. $\bar{V} = -64$ mV is still used for $\bar{g} \rightarrow \bar{I}$ conversion, still set according to figure 4.6. The spike rasters in figure 4.15 display the synchronous firing structures desired. Regarding the most synchronous network, the clear vertical line patterns are now visible, reflected by the total network spike number per time graph below. Note that the firing rates of the networks are kept consistent around ≈ 4.4 Hz, indicating that the synchronicity measure S_{PCC} is considered reliable. The S_{PCC} measure is seen to increase systematically from the first network to the last.

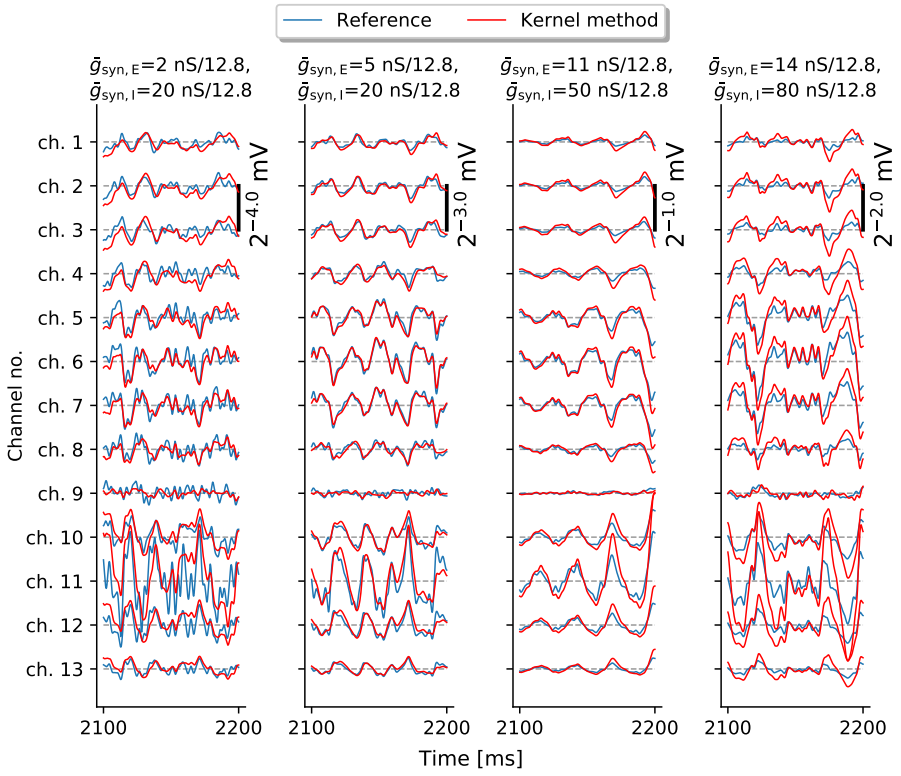

Figure 4.16: 'Reference' and kernel method LFP signals for the four weight search networks.

Figure 4.16 illustrates the LFP signals of the four weight search networks. The amplitudes are again found to increase between the four networks, similar to figure 4.13. The kernel method is still successful in recreating the 'Reference' signal in figure 4.16, though there are regions of inaccuracy seen. In particular, the amplitude of the kernel method in the final network (weights $\bar{g}_{\mathrm{syn,\,E}} = 14$ nS/12.8 and $\bar{g}_{\mathrm{syn,\,I}} = 80$ nS/12.8), is consistenly almost two times larger than the 'Reference' signal.

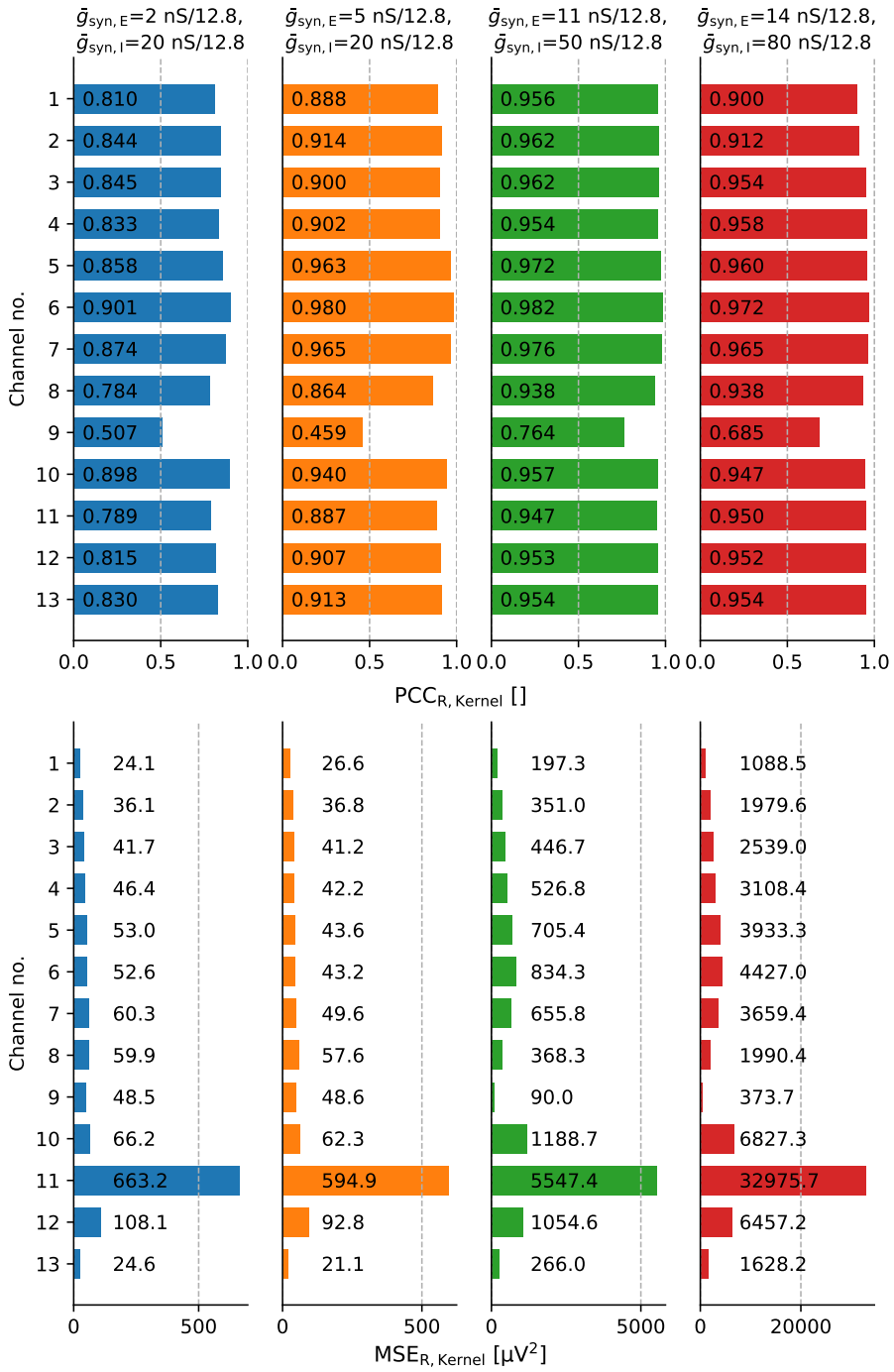

Figure 4.17: Top row: The PCC evaluation metric results of the 'Reference' and kernel signals of each channel. Bottom row: The MSE evaluation metric results of the 'Reference' and kernel signals of each channel. The four weight search cases are sorted into the four columns.

Figure 4.17 illustrates the PCC and MSE evaluation of the signals from figure 4.16. The second column is found to perform better than the first column in terms of both PCC and MSE, an interesting find considering that the network synapse strengths only differ by $\Delta\bar{g}_{\text{syn, E}} = 3$ nS/12.8. Columns three and four have outstanding PCC evaluation measures, indicating that the kernel method captured the signal variances very well. This is however at the cost of an increased MSE, which is found to be very large in column 4. The amplitude differences of column four indicate that the linear spike-to-LFP assumptions have a systematic signal magnitude error for synchronous network states. In particular, the $V \rightarrow \bar{V}$ and $\bar{g} \rightarrow \bar{I}$ conversions presented in section 3.4.2 seem to be less applicable in the highly synchronous network state. Despite this amplitude inaccuracy, the PCC indicates that the kernel method is very successful in recreating the shape/variance of the 'Reference' signal.

4.3 Biophysically Detailed Neuron Model

The results of the biophysically detailed neuron morphology described in section 3.6 are presented. Recall that this process involves implementing new neuron morphologies, configuring a baseline network similar to what was seen in section 4.1.1, followed by a methodology extent study following what was described in section 3.6.4. Firstly, the baseline network state is established, followed by the external stimulus increase study.

4.3.1 Network Baseline

The new morphologies of the network include the Hay cell for the excitatory population and a shortened BaS cell for the inhibitory population. The Hay cell morphology is illustrated in figure 4.18, accompanied by the total number of E:E and I:E synapses per depth. The histograms provide an idea of the E:E and I:E distributions on the new cell model. These reflect the distributions which are a result of the depth- and area preferences of synaptic connections, described in equation 3.12. The depth preferences of the E:E and I:E connections in the upgraded network were described in table 3.7.

The inhibitory neuron morphology is displayed in figure 4.19, where the ball-and-stick cell described in table 3.3 has a dendritic branch shortened to the specifications listed in table 3.6. The total number of E:I and I:I synapses per depth are also included, where the depth preferences listed in table 3.7 are visible.

The baseline network configuration spike raster of the biophysically detailed network is illustrated in figure 4.20. The initialization artifacts are very significant in the neuron model upgrade network, where it takes some time to stabilize, as described in section 3.4.1. The network normalization parameters $[\epsilon_{\text{E}}, \epsilon_{\text{I}}]$ described in section 3.6.3 are included above the spike raster, and recall that these are multiplied by the default number of external stimulating synapses $\text{n}_{\text{idx}} = 64$. The stimulus to each population is then scaled to $\text{n}_{\text{idx, E}} = 4.625 \cdot 64 = 296$ and $\text{n}_{\text{idx, I}} = 0.375 \cdot 64 = 24$ to fit the new morphologies.

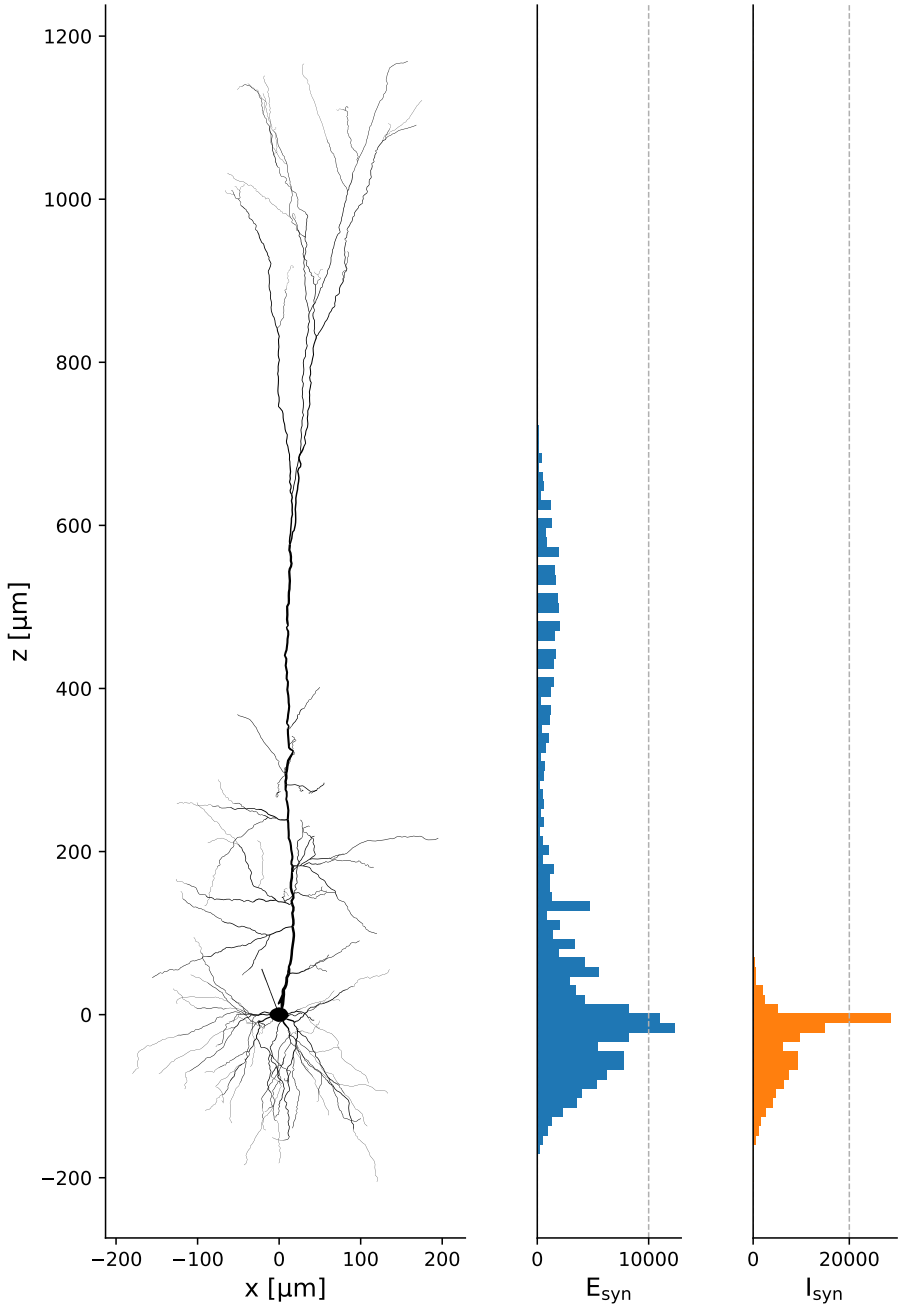

Figure 4.18: Morphology of the Hay cell, set as the excitatory population in the biophysically detailed network. The total number of E:E and I:E synapses in the network are also illustrated in a histogram of synaptic depths z using a 12 µm bin width.

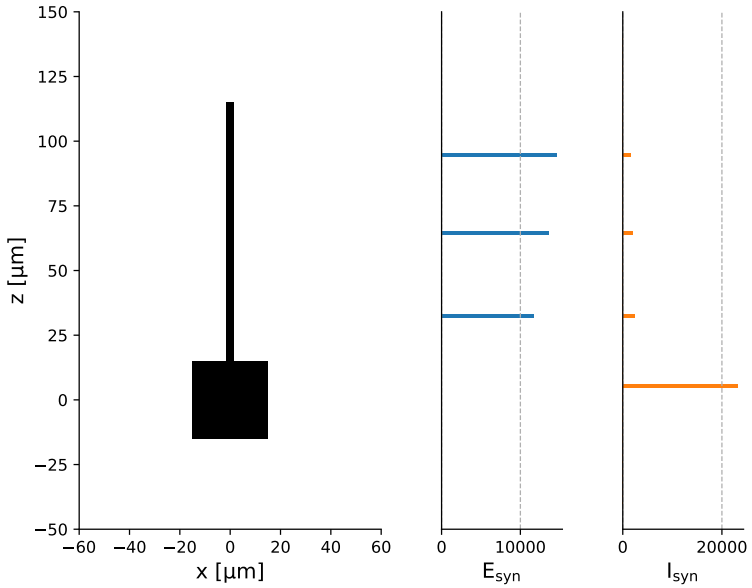

Figure 4.19: Shortened BaS cell morphology, used as the inhibitory population in the biophysically detailed network. A histogram of synaptic depths z with a 12 µm bin width of all E:I and I:I synapses is included.

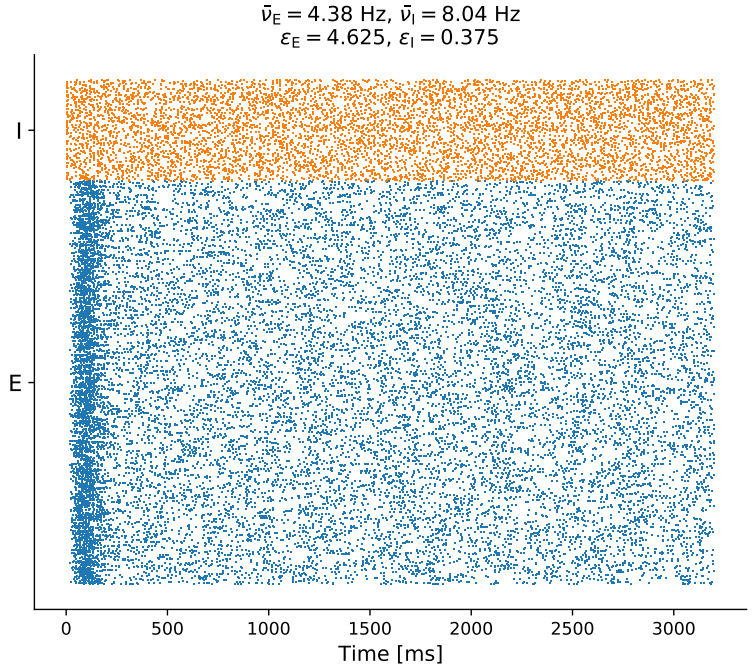

Figure 4.20: Spike raster plot of the biophysically detailed network baseline. Normalization factors $[\epsilon_E, \epsilon_I]$ and firing rates are included.

Few structures are found in the spike raster after $t_i = 200$ ms, and the spikes are quite stochastic. The firing rate of the inhibitory network is additionally larger than that of the excitatory network $\bar{\nu}_{\mathrm{I}} > \bar{\nu}_{\mathrm{E}}$. Both the asynchronous irregular firing patterns and increased inhibitory network firing rate were mentioned to be good baseline representatives of cortical activity in section 4.1.1[52].

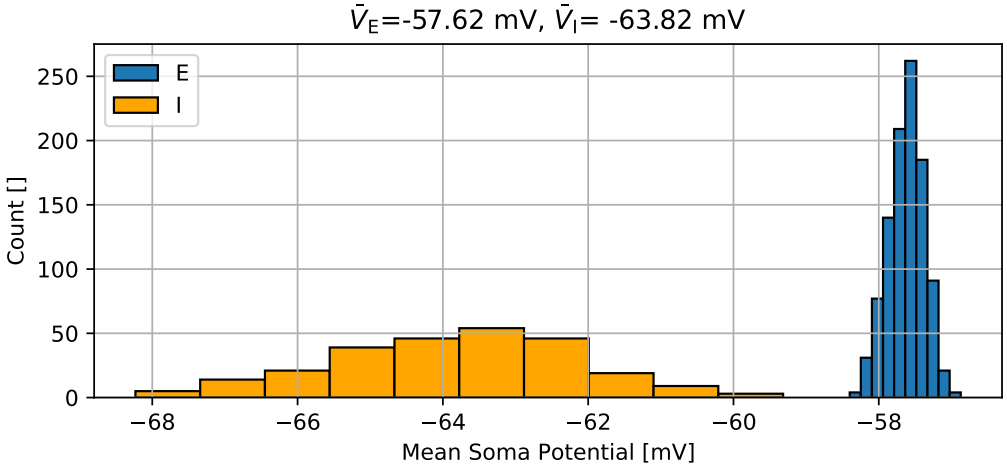

Figure 4.21: Mean soma potential distribution of each neuron in the network, split by population. The mean of the somatic potential mean values are used to determine the appropriate $\bar{V}_p$ value, as described by equation 3.43.

Figure 4.21 illustrates the mean somatic potential distributions, used to determine the population specific conversion factors $V \to \bar{V}_p$ for equation 3.43. Note that the mean somatic potential value of each neuron was obtained using the last 2000 ms of simulation time, leaving 1200 ms for initialization. The two post-synaptic estimations are set to $\bar{V}_{\mathrm{E}} = -57.62$ mV, and $\bar{V}_{\mathrm{I}} = -63.82$ mV in the upcoming current-based synapse conversions. The populations now differ clearly in mean somatic potential, contrary to the previous BaS network distributions in figure 4.6. The inhibitory population distribution is found to have a larger standard deviation than that of the excitatory population, indicating that the activity per neuron in the inhibitory population is more uneven than that of the excitatory population. This indicates that the estimation might work better for some neurons rather than others in the inhibitory population.

Moving onto the kernel method approximation, figure 4.22 illustrates the kernels of each synaptic type in the biophysically accurate network. The morphologies of the neurons are visible here, as the inhibitory BaS neuron dendrite extends up to z =115 µm, which is close to channel 10 as seen in table 3.2. The E:I and I:I kernels have very small extracellular responses in channels 1-8 for this reason. Note once again that the kernels used span $\tau_s \pm 100$ ms instead of the time frame of $[\tau_s - 20 \text{ ms}, \tau_s + 30 \text{ ms}]$ illustrated in figure 4.22. The injection sites of the E:E and I:E synapses are once again visible in the kernels. The negative extracellular potential repsponse in channels 6 and 11 of the E:E kernels indicate a positive synaptic stimulus in those regions. Similarly, the I:E

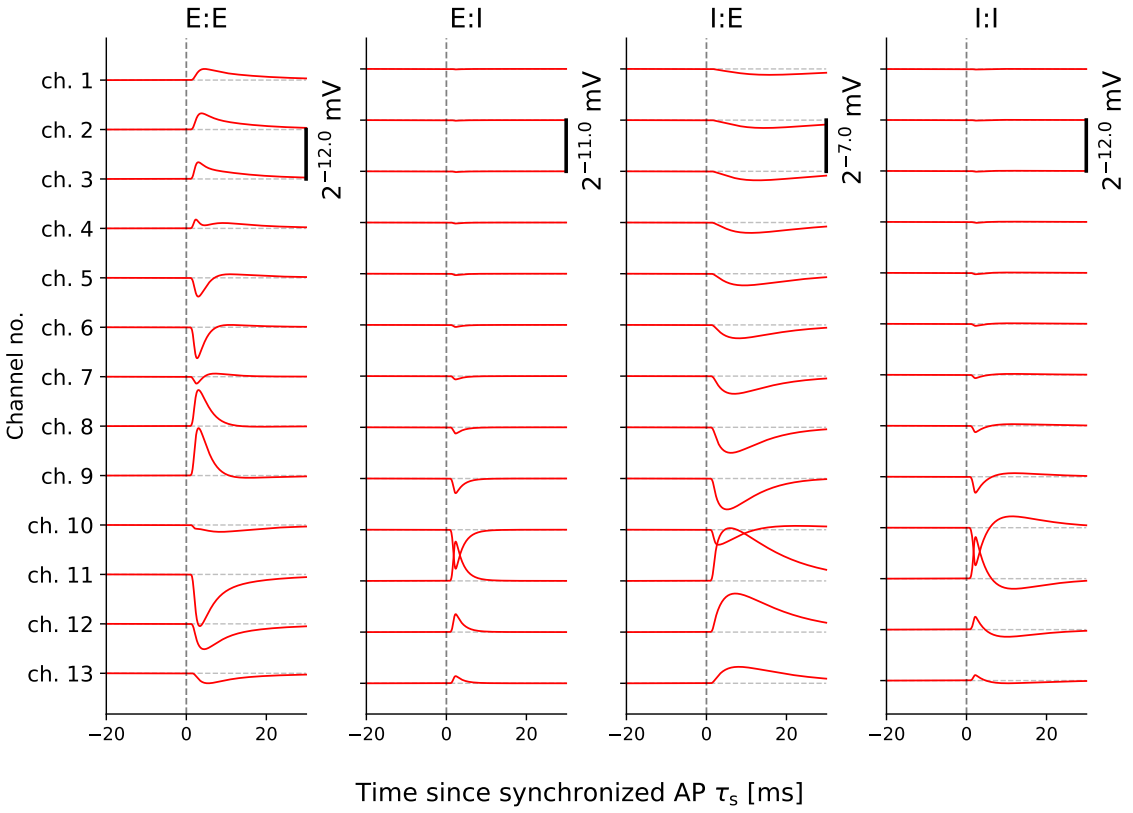

Figure 4.22: Biophysically detailed network kernels

kernel has a positive extracellular potential response in channel 11, indicating that these synapses provide a negative stimulus to the soma. These agree well with the depth preferences stated in table 3.7. The other channels have responses of opposite sign in regions which neighbor the synaptic connections - a result of current conservation as described in section 2.3.3. Note that the E:E kernel type has two depth preferences of 0 µm and 500 µm, as stated in table 3.7 and seen in figure 4.22. This results in a total of three polarity transition zones around channels 4, 7 and 10. These local cancellations in polarity transition regions were previously seen to jeopardize the performance of the kernel method in channel 9 in figure 4.10, and should be noted for the upcoming kernel results.

It important to discuss the width and amplitude of the I:E kernel. These two subjects were presented in detail in the section 4.1.4, where the inhibitory I:E and I:I kernels of figure 4.9 were wide and had relatively high amplitudes. The signal amplitudes and gain is significantly larger for the I:E kernels than for any of the others, where many of the I:E kernels do not decay to zero before the end of the illustrated $[\tau_s - 20 \text{ ms}, \tau_s + 30 \text{ ms}]$ time window. These widths were attributed to the long inhibitory synaptic decay constant $\tau_2 = 9$ ms in figure 4.9, though there is an additional factor which is referred to as intrinsic dendritic filtering. The term is described by Lindén et al. [71], which builds

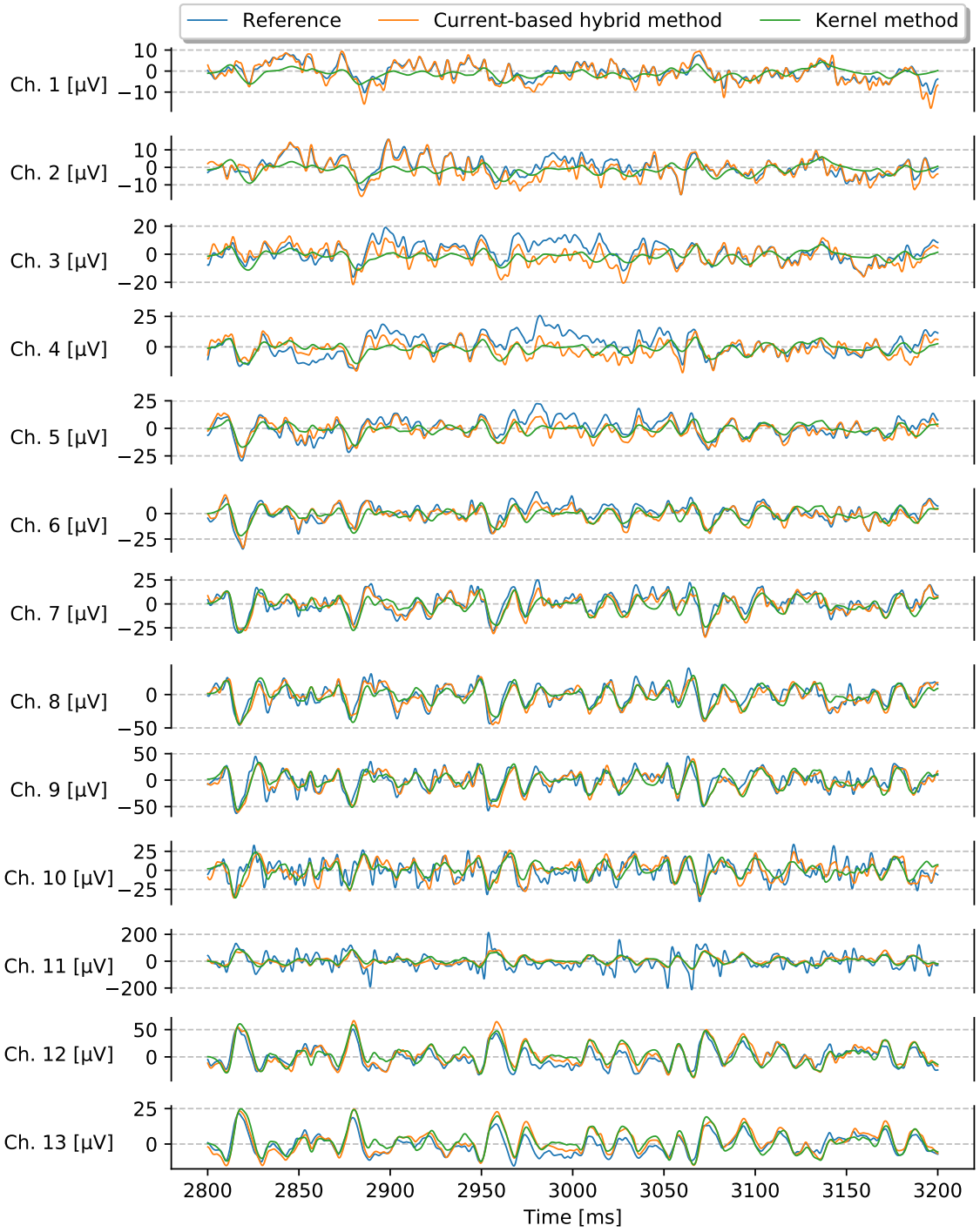

Figure 4.23: 'Reference' LFP signal in relation to the current-based hybrid- and kernel method LFP approximation signals.

upon work by Pettersen et al. [72]. The latter finds that a low-pass filtering effect is found in the extracellular potential response of APs, with a larger low-pass effect with increasing distance from the soma[72]. Lindén et al. [71] stated as a main finding that there is an unavoidable low-pass filtering effect of the extracellular potential frequency signature due to dendrites acting as electrical cables. Lindén et al. [71] goes on to state that this applies to frequencies as low as 10 Hz (well within the LFP domain), and that this filtering impact also occurs for synaptic input. The LFP power spectra which were recorded closer to the active synapses were typically found to be less low-pass filtered than those recorder further away [71]. The results from the two papers are similar; passing axial currents through a large amount of compartments produces an increased low-pass filtering effect of the recorded extracellular response. Figure 4.22 confirms this, as channels 1-3 of the I:E kernels are farthest from the synaptic input in the soma, and are found to have the lowest frequency content. The principles which lead to the low-frequency content of the kernels are important to identify, as low-frequent kernels are unable to produce relatively high-frequent LFP signals. This was described in section 3.2.3 and by figure 3.1, where a noisey input signal was smoothed by a relatively wide triangular kernel.

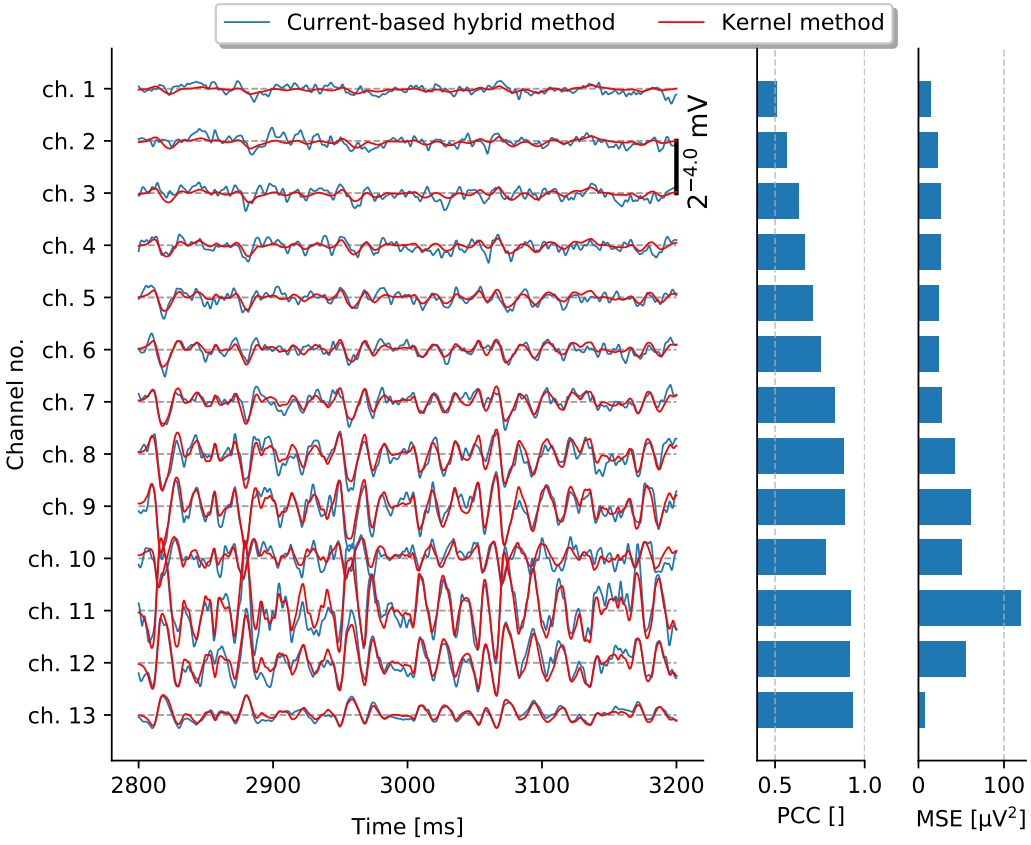

Figure 4.24: Current-based hybrid model relative to the kernel method in the biophysically detailed network. PCC and MSE metrics are included.

The 'Reference' LFP signal is illustrated with the current-based hybrid model and the kernel method LFP signals in figure 4.23. Channels 1-5 affirm the current-based hybrid method to be a successful recreation of the 'Reference' signal, though the kernel method signal frequency content is too low. The three signals agree very well in the other channels, though the 'Reference' signal amplitude is far too large in the somatic region of channel 11. The hybrid method does perform slightly better than the kernel method in the channels surrounding channel 11, though this performance increase is marginal. The performance of the kernel method in relation to the current-based hybrid method is illustrated in figure 4.24. This figure contrasts with figure 4.10, where the only poor PCC evaluation was found in channel 9. Here, channels 1-5 reveal the poor kernel method performance in terms of PCC metric, where the red kernel LFP signal is far too low-frequent. The current-based hybrid and kernel methods are however seen to be similar in channels 5-13, where the kernel method variability is larger.

4.3.2 Stimulus Increase

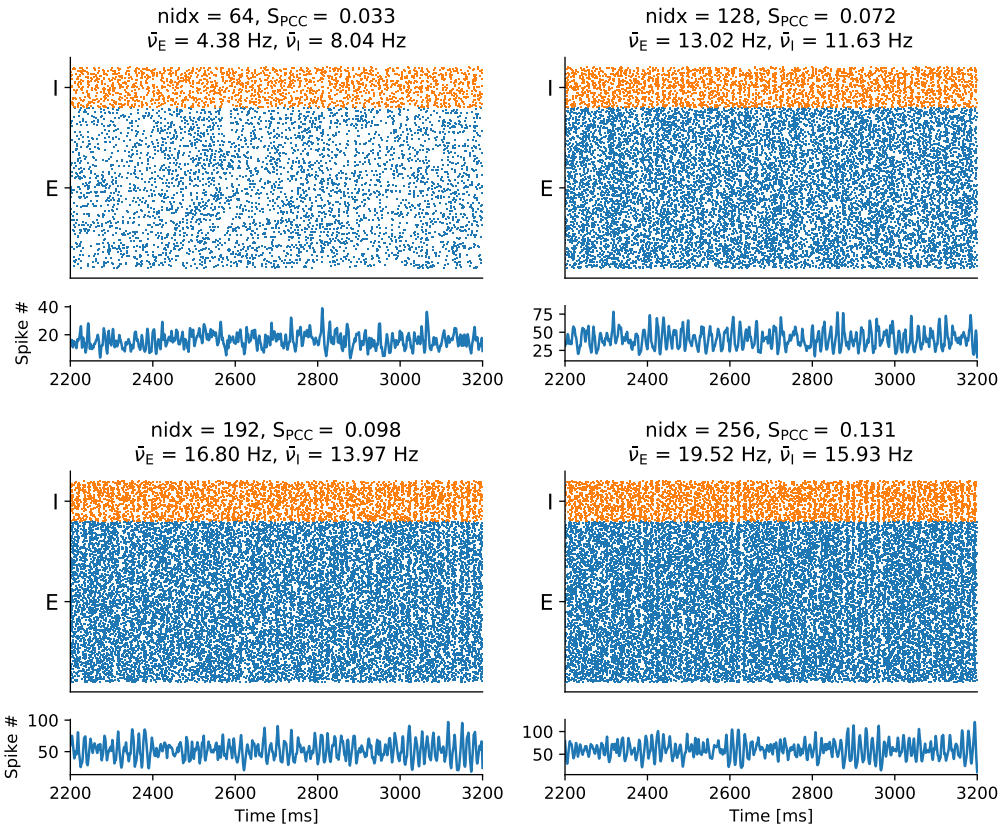

Figure 4.25: Spike raster graphs of the four levels of external stimulus in the biophysically detailed neuron network, including the smoothed total number of spikes per time. The default n_{idx} value is displayed on top of each spike raster.

Moving on to the stimulus increase study of the upgraded network, keep in mind that the default value of $n_{idx} = 64$ is increased in the same fashion as in section 4.2.1, while the normalization factors $[\epsilon_E, \epsilon_I]$ presented in figure 4.20 are kept constant throughout. To remind, the population-specific number of external synapses n_{idx} is then $n_{idx,p} = \epsilon_p n_{idx}$. The kernel method is compared to the 'Reference' signal for each network stimulus state, and an additional comparison using the hybrid method finalizes the study.

The spike rasters and their quantitative metrics of the four networks are all illustrated in figure 4.25. The total number of spikes per time are included below in the same fashion as previously, assisting in identifying network spike structures. The spiking activities of both populations $\bar{\nu}_p$ increase significantly for increased external stimulus n_{idx}, as previously. Recall that the synchronicity measure S_{PCC} is not considered reliable under such conditions. Synchronous structures are very clear in final 1000 ms of all four the T_{sim} =3200 ms simulations, and the final three external stimulus levels $n_{idx} \in [128, 192, 256]$ demonstrate the clearest synchronicity patterns.

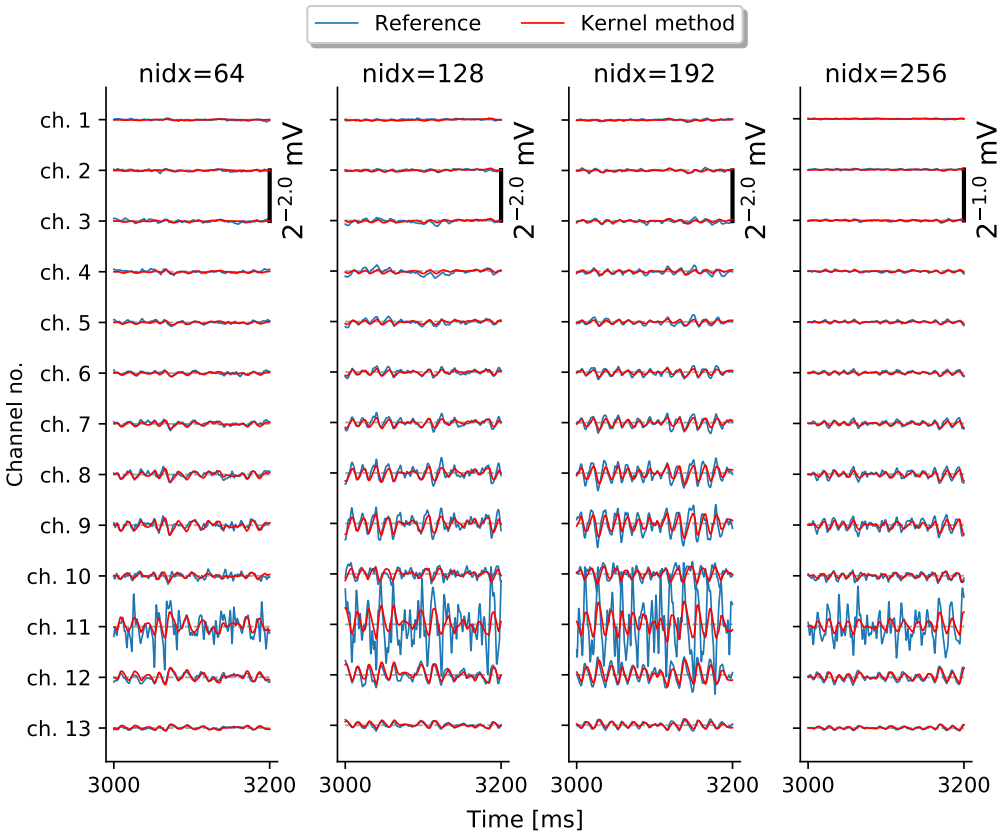

Figure 4.26: 'Reference' and Kernel method LFP signals for each channel of the four states of stimulus increase. The default n_{idx} value is indicated at the top of each column.

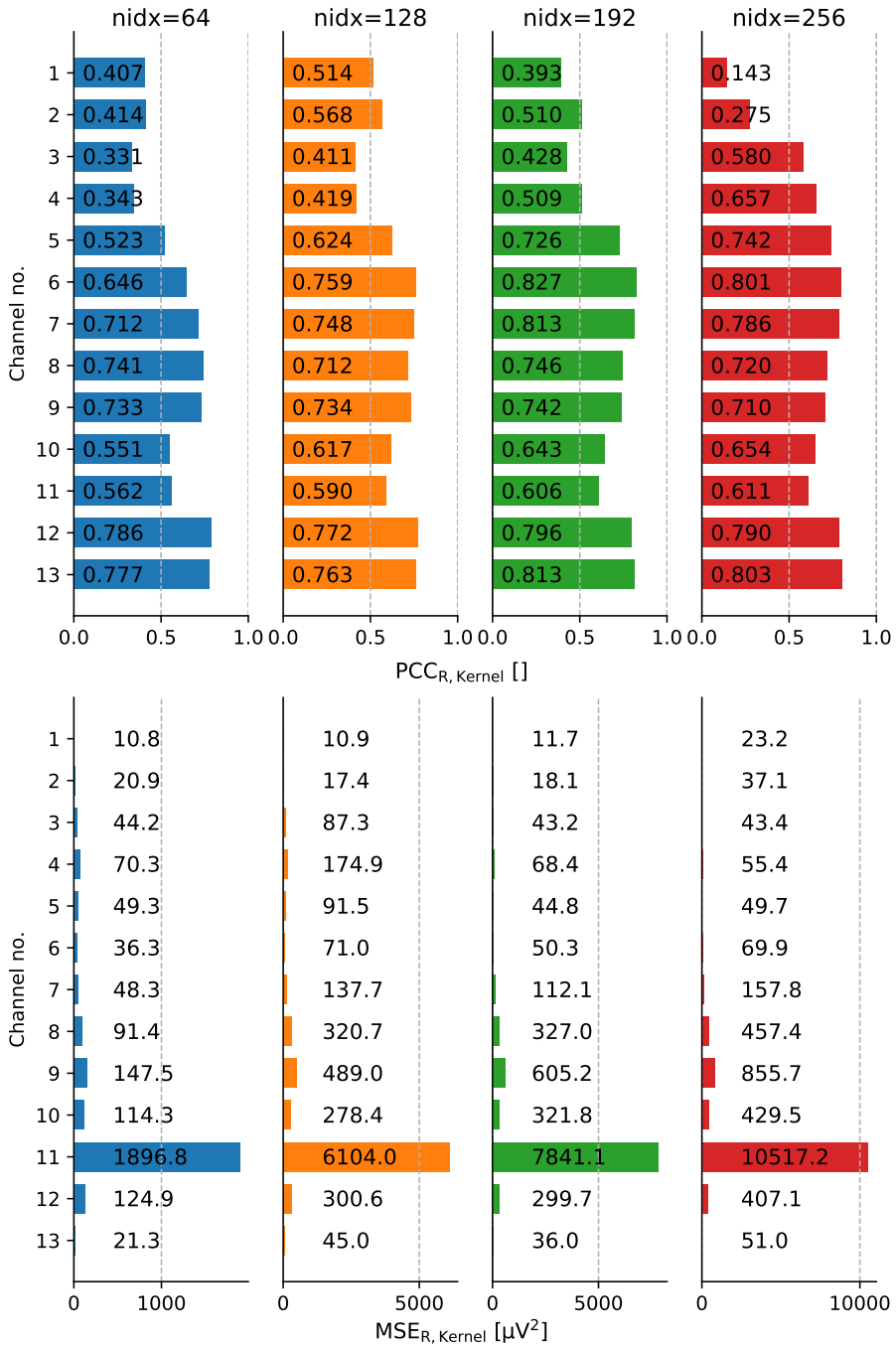

Figure 4.27: Top row: The PCC evaluation metric results of the 'Reference' and kernel signals of each channel. Bottom row: The MSE evaluation metric results of the 'Reference' and kernel signals of each channel. The default n_{idx} value is indicated at the top of each column.

The 'Reference' and kernel LFP signals of each network state are illustrated by figure 4.26. As compared to figures 4.13 and 4.16, the LFP amplitudes across the four networks figure 4.26 are quite consistent. The previous BaS methodology extent study found the amplitudes to vary up to 8 times stronger and figure 4.26 shows that the amplitude of network $n_{idx} = 256$ is only around two times stronger than network $n_{idx} = 64$.

Figure 4.27 illustrates the evaluation metrics of the signals seen in figure 4.26. Recall that the kernels H_p^c illustrated in figure 4.22 are produced by the simultaneous firing of the synaptic connections from within the network, as described in section 3.2. This means that all the network configurations $n_{idx} \in [64, 128, 192, 256]$ use the same kernels illustrated in figure 4.22. The inaccuracies seen in the topmost channel metrics of all columns in figure 4.27 are therefore attributed to the same low-frequency content of the kernel model discussed in figures 4.22 and 4.24.

4.3.3 Hybrid and Kernel Comparison

The current-based hybrid method is finally applied to the four networks and compared to the kernel method. Figure 4.28 illustrates the LFP signals in detail for all channels and networks. Note that the channels are illustrated on relative scales for a better view of the details in the topmost channels. The signals affirm the successful linear model performances in recreating the 'Reference' signal, indicating that a linear spike-LFP approximation can still account for a large amount of the ground-truth signal variability in the biophysically detailed network. Note the current-based hybrid model accuracy relative to the 'Reference' signal in the topmost channels of column $n_{idx} = 64$. The kernel method predition in this region is far too low-frequent, and this seems to be a consistent problem in channels 1-6 of column $n_{idx} = 64$. In columns $n_{idx} = [128, 192, 256]$, the current-based hybrid method seems to have consistent amplitude inaccuracies in channels 1-3. An amplitude inaccuracy of the hybrid model points to an inaccurate post-synaptic membrane potential estimation $V \rightarrow \bar{V}$. Note that new calibration factors $\bar{V}_p$ are not extracted for each new network state, and that the values found in 4.21 are still used in all four networks presented. Recalibration of the $\bar{V}_p$ factors at the start of each network is a possible solution to this. To finalize, the kernel method is compared to the current-based hybrid method by evaluation metric differences in figure 4.29. Recall that the signs between the two metric subractions is different for the PCC and MSE metrics, such that a positive value indicates a better current-based hybrid model performance for both the PCC and MSE metrics. For all columns, the largest PCC value difference is in the topmost channels, and the largest MSE differences are in the channels closest to the soma. The former is prodominantly a result of the kernel widths discussed around figure 4.22, where the low-frequency content of the kernels in the topmost channels results in a LFP approximation which does not capture large amounts of the 'Reference' LFP signal variability. The largest overall difference between the two methods is found in network $n_{idx} = 64$, where the hybrid model outperforms the kernel method consistently across all channels. The largest localized difference is found in channels 1 and 2 in network $n_{idx} = 256$, where the current-based hybrid method outperforms the kernel method with a substantial difference of $\Delta\text{PCC} \approx 0.6$, though the methods have similar performances in channels 3 and below.

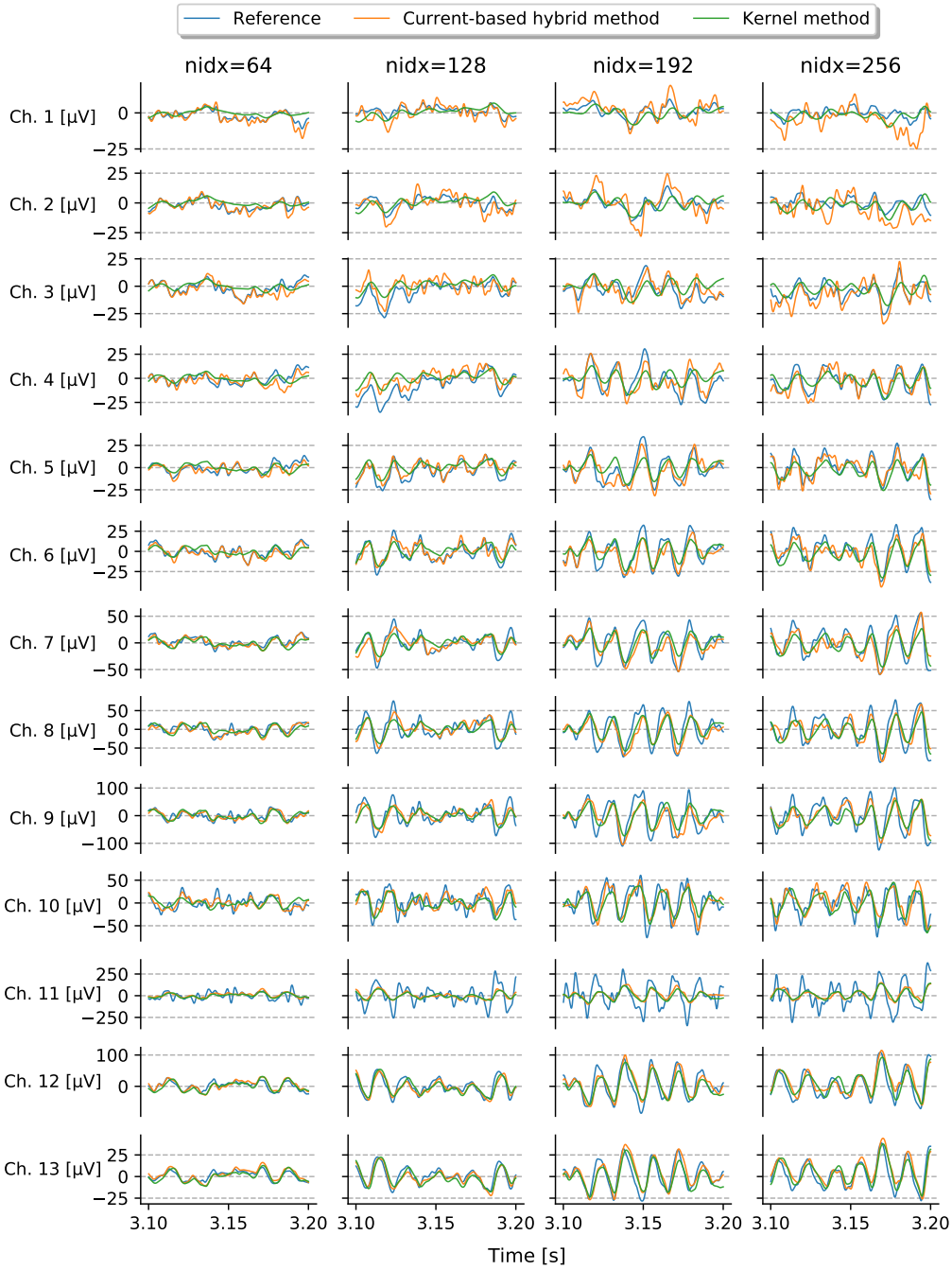

Figure 4.28: 'Reference', current-based hybrid model, and kernel method LFP signals from the four biophysically detailed networks, where the default n_{idx} value is indicated at the top of each column.

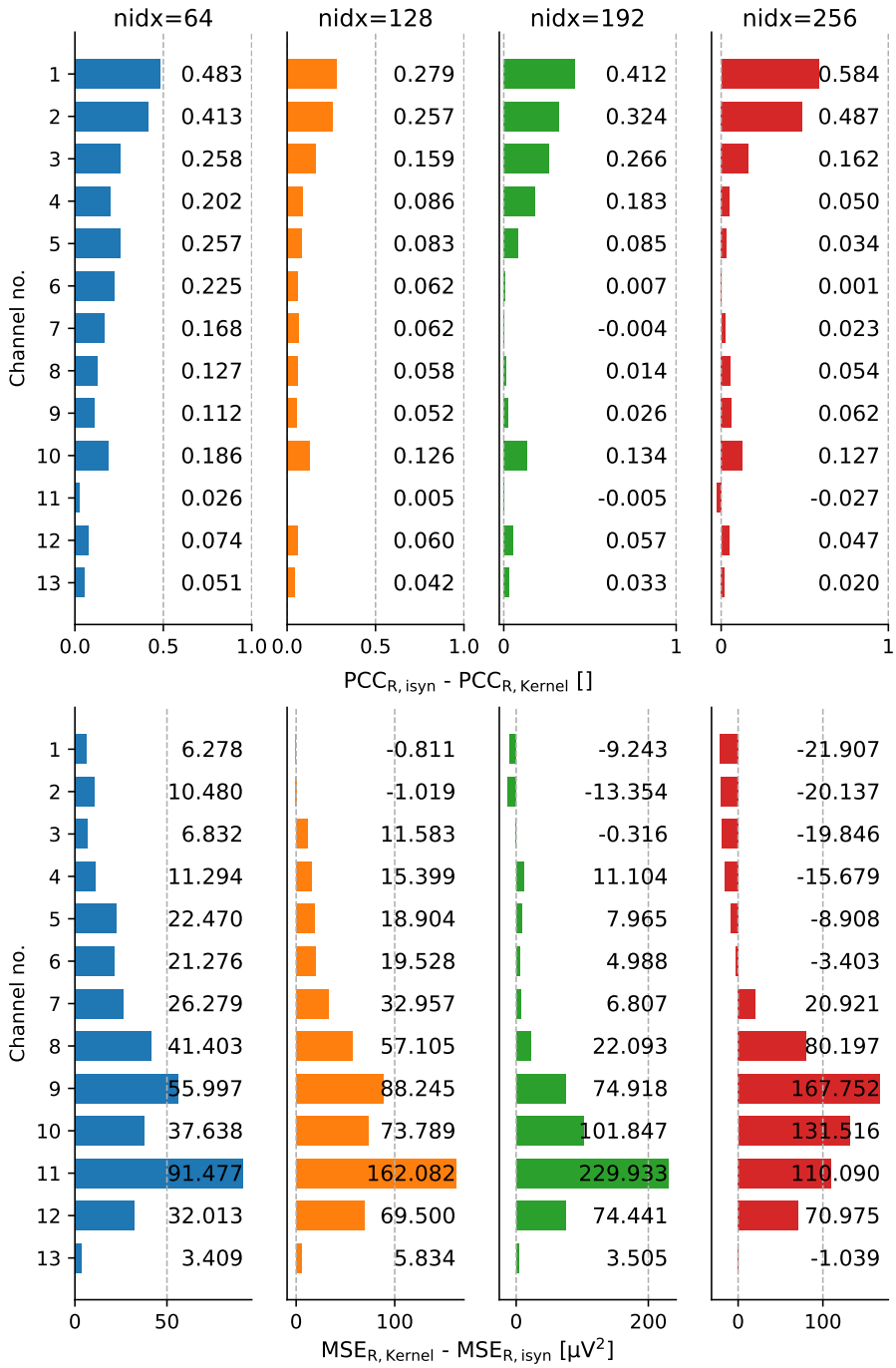

Figure 4.29: Top row: The PCC evaluation metric differences between the current-based hybrid- and kernel methods. The PCC values of both methods are calculated in relation to the 'Reference' signal and subtracted. Top row: The MSE evaluation metric differences between the current-based hybrid- and kernel methods. Both are calculated relative to the 'Reference' and subtracted. The network state is indicated by the default n_{idx} value at the top of each column.

Chapter 5

Discussion and Conclusion

5.1 Recipe-, Hybrid-, and Kernel Implementations

The study aimed to test and assess the hybrid- and kernel methods, and the results presented reinforce the work by Hagen et al. [3]. The approximations of the ground-truth local field potential (LFP) signal produced by the linear spike-LFP methods are overall found to be successful. The extracellular signals of the conductance- and current-based hybrid schemes were both found to be very accurate approximations of the ground-truth signal in the multicompartmental ball-and-stick (BaS) network. Both methods were found to have inaccuracies around the soma, and this is to be expected of the methods. The ground-truth signal includes a number of nonlinear factors, and the most prominant one comes from the high-frequent action potential (AP) contributions to the LFP around the soma. The hybrid method was generally found to perform slightly better than the kernel method, though the computational efficiency and speed of the kernel method is outstanding. On a mid-range personal computer, the hybrid method generally took above 2 hours, whereas the kernel method could be completed in less than 3 minutes when given the preliminary network information. This makes the kernel method a great option for LFP signal prediction in the BaS network.

5.2 Limitations of the Linear Models

The thesis investigated how the performances of the linear methods were impacted by synchronous network states. Two approaches were used to investigate the limitations of the linear models: one in which the external drive/stimulus of the network was increased up to four times stronger than the baseline, and another in which synchronous activity was created by tuning the synaptic strengths of the network. The expectations of the study were that the linear prediction performance would decrease with increased synchronicity, as compared to the baseline network. This study revealed that the two methods of inciting synchronicity provided no significant challenge to the kernel method, and that the pearson correlation coefficient (PCC) between the ground-truth signal and the

kernel prediction were in fact found to improve with increased external drive/stimulus and synchronicity. This improvement is mostly attributed to the signal amplitude increase, as the mean squared error (MSE) between the ground-truth and kernel predictions increased consistently for both increased external drive/stimulus and synchronicity. The largest MSE between the ground-truth and kernel method prediction by far was in the most synchronous network, where the amplitude of the kernel method prediction was up to two times larger than the ground-truth signal in all channels. An alternative to the kernel method should be considered for LFP prediction in synchronous networks if signal amplitude accuracy is of large importance.

5.3 Biophysically Detailed Network

A network was constructed using a biophysically detailed layer 5b pyramidal cell from Hay et al. [65] to study how the linear methods perform using complex cell models. The performance of the linear method predictions was expected to drop when recreating the ground-truth LFP signal of the complex cell model network, as the Hay cell consists of multiple additional nonlinear LFP contributions which were not included in the BaS configuration. The biophysically detailed network LFP signals proved to be the most difficult for the linear spike-LFP methods to recreate. The current-based hybrid method was found to outperform the kernel method overall, though both methods had large performance drops relative to that found with the BaS network configuration. These performance drops are attributed to the complex characteristics of the Hay cell.

The impact of intrinsic dendritic filtering on the kernels was found to produce very low-frequency extracellular potential responses far from the synaptic input sites, concurring with Lindén et al. [71]. This resulted in low-frequency LFP signal approximations in the same channels, significantly reducing the kernel method LFP prediction variability and accuracy. Note that this did not impact the hybrid method to the same degree despite the synaptic placements being identical, meaning that intrinsic dendritic filtering impacted the hybrid model as well. The difference is likely attributed to the fact that the kernel method reduces the contributions from specific synapses by averaging over the presynaptic cell populations. The hybrid methods ability to activate specific synapses was therefore beneficial in recreating the ground-truth LFP signal variability in channels far from the soma.

In addition to intrinsic dendritic filtering, the many additional ion channels of the Hay cell proved to be a challenge to the linear spike-LFP methods. The number of degrees of freedom in the Hay cell gave rise to complexities and non-linear factors which were not present in the BaS network, and the hybrid- and kernel schemes struggled to recreate these in their entirety. Despite the additional nonlinear LFP contributions from the Hay cell, the two linear spike-LFP methods were overall successful in approximating the LFP signal in terms of both PCC and MSE measures, indicating that linearizing the system in this fashion is suitable for larger scale networks.

5.4 Further Improvements

A number of potential shortcomings of the thesis are discussed in the following section, together with potential further improvements to the methods used. Centrally, the evaluation metrics presented could be calculated more rigorously. The PCC metric in particular would benefit from longer simulation times, converging to a consistent estimator with increasing signal length. Simulating multiple runs with varying RNG seeds and averaging evaluation metrics across runs would also yield more reliable performance evaluations. The trial size of the evaluation metrics was 1 in the thesis, and increasing the trial size would produce more statistically significant results. The synaptic model conversion method used was also quite rudimentary, and the mean network value of the mean somatic potential is likely not an ideal estimate for the general post-synaptic membrane potential. This method produced very reliable LFP approximations in the BaS network, though it likely contributed to errors in the biophysically detailed network. The post-synaptic potential estimate was also only determined by the baseline network in the limitation studies, and the mean of the mean somatic potential could be recalibrated for each of the three additional networks in the increased external drive- and synchronicity studies. Alternative methods for approximating the post-synaptic potential can also be considered, and it could additionally be interesting to search for synaptic weight combinations which result in highly synchronous activity in the biophysically detailed network, as only the increased external drive methodology was applied in this instance. A final discussion of the assumptions made in configuring the models of the thesis follows. Firstly, the membrane conductivity was set to be constant throughout the simulations. In reality, the total conductance of the membrane changes with the number of synaptic inputs. Cavallari et al. [31] sets the total membrane conductance to equal the sum of passive leak conductance and additional conductance which accounts for synaptic input. To account for this in future work, since the total conductance would be a time-dependent function, the average of the total conductance over time could be used to linearize the system. Secondly, when modeling active, voltage-dependent conductances using inactive/passive ion channels, an equivalent quasi-linearized version of the voltage-dependent conductances can be added to the membrane voltage dynamics, assuming a typical membrane potential. Ness et al. [73] showed that the LFP signals from active, voltage-dependent ion channels which use the Hodgkin-Huxley formalism can be accurately approximated by the addition of a linearized quasi-active conductance term in the voltage dynamics expression. The model then accounts for active Na^+ and K^+ contributions in the soma while still maintaining a linear spike-LFP relation. The current study removed the g_{Na} and g_{K} conductances from the somatic membrane dynamics without adding an equivalent quasi-active conductance, and an addition of a linearized quasi-active conductance term in the membrane dynamics is another further improvement for future work. Thirdly and finally, the so-called hyperpolarization-activated inward current I_{h} was not accounted for in the BaS neuron models. This current is activated by a hyperpolarized membrane, capable of producing rebound spiking in neurons [74] and resonance in the LFP power spectral density (PSD)[73]. It would also be prudent to investigate the impact which the hyperpolarization current has on the linear methods.

5.5 Conclusion

The linearized spike-LFP methods were found to successfully recreate the reference LFP signal in the BaS network. This indicates that the LFP signals are linearly dependent on the spikes of the BaS network, and is a promising find in relation to the method applications. The limitations of the linear methods were also investigated, and neither the increased external drive nor the synchronous network were found to impact the kernel method negatively. The increase in network stimulus was even found to result in more accurate PCC metrics, albeit at the cost of MSE inaccuracies. A similar result was found in networks in which synchronicity was induced. The PCC values of all channels were found to be consistently more accurate with increased synchronicity, though the most synchronous network had relatively large MSE errors in all channels.

The implementation and trials performed on the Hay cell revealed complex Hay cell dynamics to be the most damaging to the linear spike-LFP method performances. The impacts of intrinsic dendritic filtering, multiple new ion channels, and hyperpolarization-activated current I_{h} introduced new non-linear factors which the hybrid- and kernel methods were unable to account for. Ultimately, regions in which the hybrid model was preferable to be kernel method were identified in channels 1 and 2, the channels farthest from the soma. These regions were mainly attributed to regions of significant intrinsic dendritic filtering within the Hay cell.

These results could prove to be very promising when implemented for large scale simulations. The linear methods provide an advantage which allows for further upscaling of these systems, and these methods are not necessarily limited to LFP prediction. Although the LFP signal was the primary focus of the thesis, the linearization techniques presented are potentially applicable to other electrophysiological recordings of the brain which have clinical and research applications. Further exploring the application of these linear methods to MRI, MEG, EEG, and other brain activity recordings could provide a computational breakthrough to the simulations required today.

Bibliography

[1] Yazan N. Billeh, Binghuang Cai, Sergey L. Gratiy, Kael Dai, Ramakrishnan Iyer, Nathan W. Gouwens, Reza Abbasi-Asl, Xiaoxuan Jia, Joshua H. Siegle, Shawn R. Olsen, Christof Koch, Stefan Mihalas and Anton Arkhipov. 'Systematic Integration of Structural and Functional Data into Multi-scale Models of Mouse Primary Visual Cortex'. In: *Neuron* 106.3 (May 2020), 388–403.e18. DOI: 10.1016/j.neuron.2020.01.040. URL: https://doi.org/10.1016/j.neuron.2020.01.040.

[2] Wilfrid Rall. 'Theory of Physiological Properties of Dendrites'. In: *Annals of the New York Academy of Sciences* 96.4 (Dec. 2006), pp. 1071–1092. DOI: 10.1111/j.1749-6632.1962.tb54120.x. URL: https://doi.org/10.1111/j.1749-6632.1962.tb54120.x.

[3] Espen Hagen, David Dahmen, Maria L. Stavrinou, Henrik Lindén, Tom Tetzlaff, Sacha J. van Albada, Sonja Grün, Markus Diesmann and Gaute T. Einevoll. 'Hybrid Scheme for Modeling Local Field Potentials from Point-Neuron Networks'. In: *Cerebral Cortex* 26.12 (Oct. 2016), pp. 4461–4496. DOI: 10.1093/cercor/bhw237. URL: https://doi.org/10.1093/cercor/bhw237.

[4] Minoree Kohwi and Chris Q. Doe. 'Temporal fate specification and neural progenitor competence during development'. In: *Nature Reviews Neuroscience* 14.12 (Nov. 2013), pp. 823–838. DOI: 10.1038/nrn3618. URL: https://doi.org/10.1038/nrn3618.

[5] Gaute T. Einevoll, Christoph Kayser, Nikos K. Logothetis and Stefano Panzeri. 'Modelling and analysis of local field potentials for studying the function of cortical circuits'. In: *Nature Reviews Neuroscience* 14.11 (Oct. 2013), pp. 770–785. DOI: 10.1038/nrn3599. URL: https://doi.org/10.1038/nrn3599.

[6] T. N. Doan and D. L. Kunze. 'Contribution of the hyperpolarization-activated current to the resting membrane potential of rat nodose sensory neurons'. In: *The Journal of Physiology* 514.1 (Jan. 1999), pp. 125–138. DOI: 10.1111/j.1469-7793.1999.125af.x. URL: https://doi.org/10.1111/j.1469-7793.1999.125af.x.

[7] 'Medical gallery of Blausen Medical 2014'. In: *WikiJournal of Medicine* 1.2 (2014). DOI: 10.15347/wjm/2014.010. URL: https://doi.org/10.15347/wjm/2014.010.

[8] OpenStax College. *Anatomy & Physiology*. Retrieved 18. May 2021. URL: https://courses.lumenlearning.com/ap1/chapter/the-action-potential/.

[9] David Sterratt, Bruce Graham, Andrew Gillies and David Willshaw. *Principles of Computational Modelling in Neuroscience*. Cambridge University Press, 2011. DOI: 10.1017/CBO9780511975899.

[10] *"Channelpedia", Web-based freely-accessible information management network and electrophysiology data repository for comprehensive ion channel research*. Retrieved 18. May 2021. URL: https://channelpedia.epfl.ch/.

[11] *"Ion Channel Geneaology", A comprehensive and quantitative assay of ion channel models currently available in the neuroscientific modeling community, all browsable in interactive visualizations*. Retrieved 18. May 2021. URL: https://icg.neurotheory.ox.ac.uk/.

[12] William F Podlaski, Alexander Seeholzer, Lukas N Groschner, Gero Miesenböck, Rajnish Ranjan and Tim P Vogels. 'Mapping the function of neuronal ion channels in model and experiment'. In: *eLife* 6 (Mar. 2017). DOI: 10.7554/elife.22152. URL: https://doi.org/10.7554/elife.22152.

[13] R.P. Deshpande. *Capacitors*. McGraw-Hill Education, 2014. ISBN: 9780071848572. URL: https://books.google.is/books?id=rFGoBAAAQBAJ.

[14] Aarushi Khanna. *Action Potential*. Retrieved 18. May 2021. URL: https://teachmephysiology.com/nervous-system/synapses/action-potential/.

[15] Stuart Irvine. *Conduction of the Action Potential*. Retrieved 18. May 2021. URL: https://dundeemedstudentnotes.wordpress.com/2012/04/07/conduction-of-the-action-potential/.

[16] Designua. *Neural communication. Transmission of the nerve signal between two neurons with axon and synapse. Close-up of a chemical synapse. vector diagram for education, medical, science use*. Retrieved 18. May 2021. URL: https://www.shutterstock.com/image-vector/neural-communication-transmission-nerve-signal-between-1456461275.

[17] Pasquale De Michele. 'Analysis, tuning and implementation of neuronal models simulating Hippocampus dynamics'. PhD thesis. Mar. 2015. DOI: 10.6092/UNINA/FEDOA/10322.

[18] Dave Beeman. *Modeling Dendrites and Synapses*. Retrieved 18. May 2021. URL: http://ecee.colorado.edu/~ecen4831/cnsweb/cns2a.html.

[19] A. L. Hodgkin and A. F. Huxley. 'A quantitative description of membrane current and its application to conduction and excitation in nerve'. In: *The Journal of Physiology* 117.4 (Aug. 1952), pp. 500–544. DOI: 10.1113/jphysiol.1952.sp004764. URL: https://doi.org/10.1113/jphysiol.1952.sp004764.

[20] Nobel Media AB 2021. *The Nobel Prize in Physiology or Medicine 1963*. Retrieved 18. May 2021. URL: https://www.nobelprize.org/prizes/medicine/1963/summary/.

[21] C. Morris and H. Lecar. 'Voltage oscillations in the barnacle giant muscle fiber'. In: *Biophysical Journal* 35.1 (July 1981), pp. 193–213. DOI: 10.1016/s0006-3495(81)84782-0. URL: https://doi.org/10.1016/s0006-3495(81)84782-0.

[22] Richard FitzHugh. 'Impulses and Physiological States in Theoretical Models of Nerve Membrane'. In: *Biophysical Journal* 1.6 (July 1961), pp. 445–466. DOI: 10.1016/s0006-3495(61)86902-6. URL: https://doi.org/10.1016/s0006-3495(61)86902-6.

[23] A. L. Hodgkin, A. F. Huxley and B. Katz. 'Measurement of current-voltage relations in the membrane of the giant axon of Loligo'. In: *The Journal of Physiology* 116.4 (Apr. 1952), pp. 424–448. DOI: 10.1113/jphysiol.1952.sp004716. URL: https://doi.org/10.1113/jphysiol.1952.sp004716.

[24] Peter E Latham, BJ Richmond, PG Nelson and S Nirenberg. 'Intrinsic dynamics in neuronal networks. I. Theory'. In: *Journal of neurophysiology* 83.2 (2000), pp. 808–827.

[25] Wulfram Gerstner and Werner M Kistler. *Spiking neuron models: Single neurons, populations, plasticity*. Cambridge university press, 2002.

[26] Wulfram Gerstner, Werner M Kistler, Richard Naud and Liam Paninski. *Neuronal dynamics: From single neurons to networks and models of cognition*. Cambridge University Press, 2014.

[27] Richard B. Stein, E. Roderich Gossen and Kelvin E. Jones. 'Neuronal variability: noise or part of the signal?' In: *Nature Reviews Neuroscience* 6.5 (May 2005), pp. 389–397. DOI: 10.1038/nrn1668. URL: https://doi.org/10.1038/nrn1668.

[28] Richard B. Stein. 'A Theoretical Analysis of Neuronal Variability'. In: *Biophysical Journal* 5.2 (Mar. 1965), pp. 173–194. DOI: 10.1016/s0006-3495(65)86709-1. URL: https://doi.org/10.1016/s0006-3495(65)86709-1.

[29] R.D. Yates. *Probability and Stochastic Processes: A Friendly Introduction for Electrical and Computer Engineers, 3rd Edition: Third Edition*. Probability and Stochastic Processes: A Friendly Introduction for Electrical and Computer Engineers. John Wiley & Sons, 2014. ISBN: 9781118804384. URL: https://books.google.ie/books?id=zn5bAgAAQBAJ.

[30] Frank A. Haight. *Handbook of the Poisson distribution by Frank A. Haight*. English. Wiley New York, 1967, xi, 168 p.

[31] Stefano Cavallari, Stefano Panzeri and Alberto Mazzoni. 'Comparison of the dynamics of neural interactions between current-based and conductance-based integrate-and-fire recurrent networks'. In: *Frontiers in Neural Circuits* 8 (Mar. 2014). DOI: 10.3389/fncir.2014.00012. URL: https://doi.org/10.3389/fncir.2014.00012.

[32] Simon S Keller and Neil Roberts. 'Measurement of brain volume using MRI: software, techniques, choices and prerequisites'. In: *J Anthropol Sci* 87 (2009), pp. 127–151.

[33] Vangelis Sakkalis. 'Review of advanced techniques for the estimation of brain connectivity measured with EEG/MEG'. In: *Computers in biology and medicine* 41.12 (2011), pp. 1110–1117.

[34] Leslie Gordon Kiloh, Alan J McComas and John Walkinshaw Osselton. *Clinical electroencephalography*. Butterworth-Heinemann, 2013.

[35] Tobias Pistohl, Tonio Ball, Andreas Schulze-Bonhage, Ad Aertsen and Carsten Mehring. 'Prediction of arm movement trajectories from ECoG-recordings in humans'. In: *Journal of neuroscience methods* 167.1 (2008), pp. 105–114.

[36] R. Brette and A. Destexhe. *Handbook of Neural Activity Measurement*. Cambridge University Press, 2012. ISBN: 9780521516228. URL: https://books.google.no/books?id=YLyGmfVuBsIC.

[37] Seward B. Rutkove. 'Introduction to Volume Conduction'. In: *The Clinical Neurophysiology Primer*. Humana Press, pp. 43–53. DOI: 10.1007/978-1-59745-271-7_4. URL: https://doi.org/10.1007/978-1-59745-271-7_4.

[38] Edwin Kashy Sharon Bertsch McGrayne et al. *Electricity*. Retrieved 18. May 2021. URL: https://www.britannica.com/science/electricity/Calculating-the-value-of-an-electric-field#ref71555.

[39] Steinn Magnusson. *Github Thesis repository*. Retrieved 18. May 2021. URL: https://github.com/steinnhauser/linearLFP.

[40] Wilfrid Rall and Gordon M Shepherd. 'Theoretical reconstruction of field potentials and dendrodendritic synaptic interactions in olfactory bulb.' In: *Journal of neurophysiology* 31.6 (1968), pp. 884–915.

[41] Gary R Holt and Christof Koch. 'Electrical interactions via the extracellular potential near cell bodies'. In: *Journal of computational neuroscience* 6.2 (1999), pp. 169–184.

[42] Espen Hagen, Solveig Næss, Torbjørn V. Ness and Gaute T. Einevoll. 'Multimodal Modeling of Neural Network Activity: Computing LFP, ECoG, EEG, and MEG Signals With LFPy 2.0'. In: *Frontiers in Neuroinformatics* 12 (Dec. 2018). DOI: 10.3389/fninf.2018.00092. URL: https://doi.org/10.3389/fninf.2018.00092.

[43] Steinn Magnusson. *Initial 'example network' code on Github*. Retrieved 18. May 2021. URL: https://github.com/LFPy/LFPy/blob/49f819/examples/example_network/example_network.py.

[44] M. L. Hines and N. T. Carnevale. 'Neuron: A Tool for Neuroscientists'. In: *The Neuroscientist* 7.2 (Apr. 2001), pp. 123–135. DOI: 10.1177/107385840100700207. URL: https://doi.org/10.1177/107385840100700207.

[45] Henrik Lindén, Espen Hagen, Szymon Leski, Eivind S Norheim, Klas H Pettersen and Gaute T Einevoll. 'LFPy: a tool for biophysical simulation of extracellular potentials generated by detailed model neurons'. In: *Frontiers in neuroinformatics* 7 (2014), p. 41.

[46] H Lindén, E Hagen, S Łęski, ES Norheim, KH Pettersen et al. 'LFPy: A tool for simulation of extracellular potentials'. In: *Frontiers in Neuroinformatics* 5 (2011).

[47] Solveig Næss, Torbjørn V Ness, Geir Halnes, Anders M Dale and Gaute T Einevoll. 'Biophysical Modeling of Single-Neuron Contributions to EEG and ECoG Signals'. In: *1st Human Brain Project Student Conference*, p. 105.

[48] Math Vault. *List of Probability and Statistics Symbols*. Retrieved 18. May 2021. URL: https://mathvault.ca/hub/higher-math/math-symbols/probability-statistics-symbols/.

[49] Andrew Gillies and David Sterratt. *A NEURON Programming Tutorial - Part A*. Retrieved 18. May 2021. URL: http://web.mit.edu/neuron_v7.4/nrntuthtml/tutorial/tutA.html.

[50] Tobias C. Potjans and Markus Diesmann. 'The Cell-Type Specific Cortical Microcircuit: Relating Structure and Activity in a Full-Scale Spiking Network Model'. In: *Cerebral Cortex* 24.3 (Dec. 2012), pp. 785–806. ISSN: 1047-3211. DOI: 10.1093/cercor/bhs358. eprint: https://academic.oup.com/cercor/article-pdf/24/3/785/14099777/bhs358.pdf. URL: https://doi.org/10.1093/cercor/bhs358.

[51] Sacha Jennifer van Albada, Moritz Helias and Markus Diesmann. 'Scalability of Asynchronous Networks Is Limited by One-to-One Mapping between Effective Connectivity and Correlations'. In: *PLOS Computational Biology* 11.9 (Sept. 2015). Ed. by Peter E. Latham, e1004490. DOI: 10.1371/journal.pcbi.1004490. URL: https://doi.org/10.1371/journal.pcbi.1004490.

[52] Nicolas Brunel. 'Dynamics of sparsely connected networks of excitatory and inhibitory spiking neurons'. In: *Journal of computational neuroscience* 8.3 (2000), pp. 183–208.

[53] M Megías, Zs Emri, T.F Freund and A.I Gulyás. 'Total number and distribution of inhibitory and excitatory synapses on hippocampal CA1 pyramidal cells'. In: *Neuroscience* 102.3 (Feb. 2001), pp. 527–540. DOI: 10.1016/s0306-4522(00)00496-6. URL: https://doi.org/10.1016/s0306-4522(00)00496-6.

[54] Steven W. Smith. *The scientist and engineer's guide to digital signal processing*. 1st ed. San Diego, Calif: California Technical Pub, 1997. ISBN: 9780966017632.

[55] Steven B. Damelin and Willard Miller. *The mathematics of signal processing*. Cambridge texts in applied mathematics 48. OCLC: ocn751752415. Cambridge ; New York: Cambridge University Press, 2012. ISBN: 9781107013223 9781107601048.

[56] opentextbc.ca. *"Introductory Business Statistics: The Correlation Coefficient r"*. Retrieved 18. May 2021. URL: https://opentextbc.ca/introbusinessstatopenstax/chapter/the-correlation-coefficient-r/.

[57] Eric W. Weisstein. *"Statistical Correlation." From MathWorld–A Wolfram Web Resource*. Retrieved 18. May 2021. URL: https://mathworld.wolfram.com/StatisticalCorrelation.html.

[58] Eric W. Weisstein. *"Covariance." From MathWorld–A Wolfram Web Resource*. Retrieved 18. May 2021. URL: https://mathworld.wolfram.com/Covariance.html.

[59] Gerald Kaiser and Lonnie H. Hudgins. 'A Friendly Guide to Wavelets'. In: *Physics Today* 48.7 (July 1995), pp. 57–58. DOI: 10.1063/1.2808105. URL: https://doi.org/10.1063/1.2808105.

[60] M. Rahman. *Applications of Fourier Transforms to Generalized Functions*. WIT Press, 2011. ISBN: 9781845645649. URL: https://books.google.no/books?id=k%5C_rdcKaUdr4C.

[61] F. Rieke. *Spikes: Exploring the Neural Code*. Bradford book. MIT Press, 1999. ISBN: 9780262681087. URL: https://books.google.ie/books?id=pcs6qJIawScC.

[62] Vibration Research University. *Calculating PSD from a Time History File*. Retrieved 18. May 2021. URL: https://vru.vibrationresearch.com/lesson/calculating-psd-time-history/.

[63] Peter Welch. 'The use of fast Fourier transform for the estimation of power spectra: a method based on time averaging over short, modified periodograms'. In: *IEEE Transactions on audio and electroacoustics* 15.2 (1967), pp. 70–73.

[64] Stephen Butterworth et al. 'On the theory of filter amplifiers'. In: *Wireless Engineer* 7.6 (1930), pp. 536–541.

[65] Etay Hay, Sean Hill, Felix Schürmann, Henry Markram and Idan Segev. 'Models of Neocortical Layer 5b Pyramidal Cells Capturing a Wide Range of Dendritic and Perisomatic Active Properties'. In: *PLoS Computational Biology* 7.7 (July 2011). Ed. by Lyle J. Graham, e1002107. DOI: 10.1371/journal.pcbi.1002107. URL: https://doi.org/10.1371/journal.pcbi.1002107.

[66] M. Denker, A. Yegenoglu and S. Grün. 'Collaborative HPC-enabled workflows on the HBP Collaboratory using the Elephant framework'. In: *Neuroinformatics 2018*. 2018, P19. DOI: 10.12751/incf.ni2018.0019. URL: https://abstracts.g-node.org/conference/NI2018/abstracts#/uuid/023bec4e-0c35-4563-81ce-2c6fac282abd.

[67] Pauli Virtanen, Ralf Gommers, Travis E. Oliphant, Matt Haberland, Tyler Reddy, David Cournapeau, Evgeni Burovski, Pearu Peterson, Warren Weckesser, Jonathan Bright, Stéfan J. van der Walt, Matthew Brett, Joshua Wilson, K. Jarrod Millman, Nikolay Mayorov, Andrew R. J. Nelson, Eric Jones, Robert Kern, Eric Larson, C J Carey, İlhan Polat, Yu Feng, Eric W. Moore, Jake VanderPlas, Denis Laxalde, Josef Perktold, Robert Cimrman, Ian Henriksen, E. A. Quintero, Charles R. Harris, Anne M. Archibald, Antônio H. Ribeiro, Fabian Pedregosa, Paul van Mulbregt and SciPy 1.0 Contributors. 'SciPy 1.0: Fundamental Algorithms for Scientific Computing in Python'. In: *Nature Methods* 17 (2020), pp. 261–272. DOI: 10.1038/s41592-019-0686-2.

[68] A.V. Oppenheim and A.S. Willsky. *Signals and Systems: Pearson New International Edition*. Always learning. Pearson Education Limited, 2013. ISBN: 9781292025902. URL: https://books.google.is/books?id=ut9oAQAACAAJ.

[69] Michiel Hazewinkel. *Encyclopaedia of mathematics*. Springer-Verlag, 2002. ISBN: 9781402006098. URL: http://eom.springer.de/default.htm.

[70] Encyclopedia of Mathematics. *Consistent estimator*. Retrieved 18. May 2021. URL: http://encyclopediaofmath.org/index.php?title=Consistent_estimator&oldid=46481.

[71] Henrik Lindén, Klas H. Pettersen and Gaute T. Einevoll. 'Intrinsic dendritic filtering gives low-pass power spectra of local field potentials'. In: *Journal of Computational Neuroscience* 29.3 (May 2010), pp. 423–444. DOI: 10.1007/s10827-010-0245-4. URL: https://doi.org/10.1007/s10827-010-0245-4.

[72] Klas H. Pettersen and Gaute T. Einevoll. 'Amplitude Variability and Extracellular Low-Pass Filtering of Neuronal Spikes'. In: *Biophysical Journal* 94.3 (Feb. 2008), pp. 784–802. DOI: 10.1529/biophysj.107.111179. URL: https://doi.org/10.1529/biophysj.107.111179.

[73] Torbjørn V Ness, Michiel WH Remme and Gaute T Einevoll. 'Active subthreshold dendritic conductances shape the local field potential'. In: *The Journal of physiology* 594.13 (2016), pp. 3809–3825.

[74] Zhiguo Zhao, Li Li and Huaguang Gu. 'Dynamical Mechanism of Hyperpolarization-Activated Non-specific Cation Current Induced Resonance and Spike-Timing Precision in a Neuronal Model'. In: *Frontiers in Cellular Neuroscience* 12 (Mar. 2018). DOI: 10.3389/fncel.2018.00062. URL: https://doi.org/10.3389/fncel.2018.00062.